6. Appendixes – attached publication

Publication declaration

In all publications included in this thesis, I, Tomáš Urbánek, was responsible for the synthetic procedures and the physico-chemical characterization of the prepared materials. This included techniques such as SEC, UV-Vis spectrophotometry, DLS, and NMR, with advanced NMR measurements conducted with the assistance of Rafał Konefał. The SEM and TEM analyses were performed by Miroslav Šlouf. A4F was carried out by Dmytro Rak and Marián Sedlák at the Institute of Experimental Physics in Košice. Cyclic voltammetry and EIS were conducted by Iryna Ivanko, while Jan Svoboda performed XPS. The biological characterization of the samples was undertaken by collaborating biologists, including Jiří Trousil, Kristýna Gunár, Olga Šebestová Janoušková, Jana Matějková, You-Shan Dai, Jia-You Fang, and Miša Škorič, at various institutions such as the Institute of Macromolecular Chemistry AS CR, the Department of Medical Microbiology at the Second Faculty of Medicine, Charles University, the Pharmaceutics Laboratory at the Graduate Institute of Natural Products, Chang Gung University, and the Department of Pathological Morphology and Parasitology at the Faculty of Veterinary Medicine, University of Veterinary Sciences Brno.

Appendix 1

Urbánek, T.; Jägger, E.; Jägger, A.; Hrubý, M. Selectively Biodegradable Polyesters: Nature-Inspired Construction Materials for Future Biomedical Applications. *Polymers* **2019**, 11 (6), 1061. IF = 4.9

Selectively Biodegradable Polyesters: Nature-Inspired Construction Materials for Future Biomedical Applications

Tomáš Urbánek, Eliézer Jäger, Alessandro Jäger and Martin Hrubý *

Institute of Macromolecular Chemistry, Czech Academy of Sciences, Heyrovského náměstí 2, 162 00 Prague 6, Czechia; urbanekto@gmail.com (T.U.); jager@imc.cas.cz (E.J.); ajager@imc.cas.cz (A.J.)
* Correspondence: mhruby@centrum.cz

Abstract: In the last half-century, the development of biodegradable polyesters for biomedical applications has advanced significantly. Biodegradable polyester materials containing external stimuli-sensitive linkages are favored in the development of therapeutic devices for pharmacological applications such as delivery vehicles for controlled/sustained drug release. These selectively biodegradable polyesters degrade after particular external stimulus (e.g., pH or redox potential change or the presence of certain enzymes). This review outlines the current development of biodegradable synthetic polyesters materials able to undergo hydrolytic or enzymatic degradation for various biomedical applications, including tissue engineering, temporary implants, wound healing and drug delivery.

Keywords: polyester; polycondensation; ring-opening; stimuli-sensitive; drug delivery; biodegradability; medical application

1. Introduction

The days of Carothers's skepticism about the quality of polyesters (PES) are long gone and deeper knowledge brings insight into many areas of interest every day. Due to the extensive research, the polymeric structure and the final material properties can be deliberately fine-tuned by different approaches of polymer chemistry for the purposes of specific applications [1].

The polymer chemistry has a wide toolbox available for tuning and fine-tuning the structure and properties of final material. The nature of monomers, the regulation of the molar mass and the dispersity are the very basic concept of the control over properties. Nowadays, there are several polymerization techniques, which enable us to control molar mass and narrow dispersity very precisely. The introduction of branching points into the polymer structure is another simple way of modulation of the final properties [2]. There are many other approaches of modulating the final properties of polymer materials—introduction of functional groups, combination of two or more polymers or with other materials, etc. The keystone of successful fine-tuning is the understanding of the relationship between the structure and functional properties of polymer materials.

In addition, there are particular polymers—the so-called smart polymers—which benefit from the fact that they can undergo structural changes after being exposed to an external stimulus (pH change, temperature change, presence of particular molecules, etc.) leading to significant change in physico-chemical or solution properties within a relatively narrow window of the external environment change. Obviously, there are such smart polyesters, which respond to external stimuli, too.

1.1. Synthesis and Mechanisms

Albertsson and Varma [3] reported that polycondensation, ring opening polymerization (ROP) and enzymatic polymerization are the three major routes for the synthesis of aliphatic polyesters. A very interesting but minor polymerization technique that also leads to polyesters is the free radical ROP of 2-methylidene-1,3-dioxepane. This process offers us a wide range of copolymers combining ester bond with repeating units derived from vinylic monomers in the backbone, which would not be possible to prepare by any other process [4,5]. The synthetic routes leading to aliphatic polyesters are schematically shown in Figure 1.
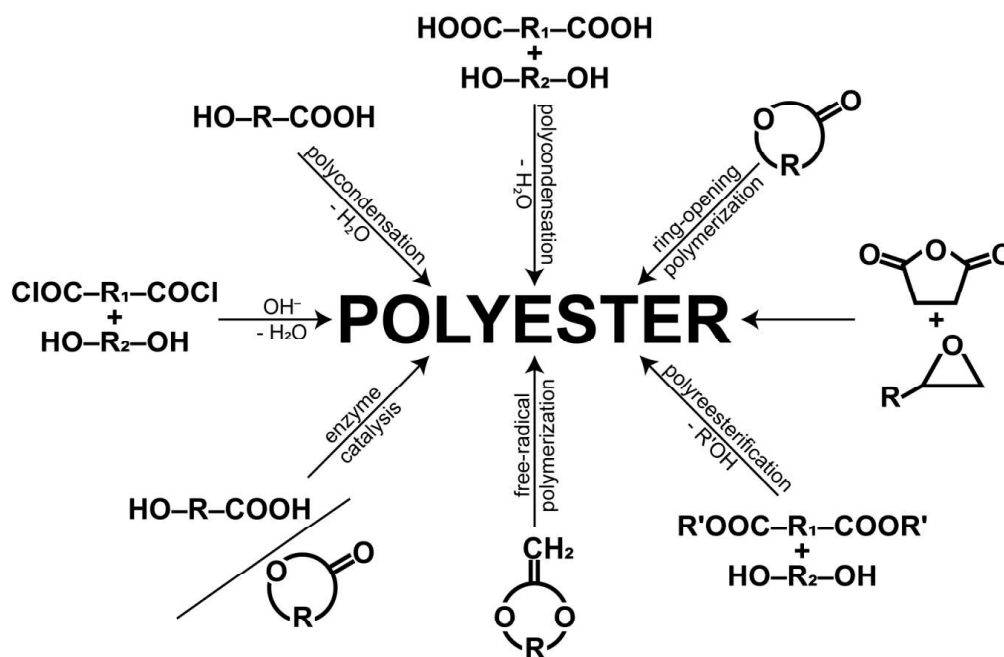
Figure 1. An overview of the synthetic routes used for the synthesis of polyesters.

Polycondensation is characterized by a stepwise polymerization reaction involving difunctional monomers of the AB type, i.e., hydroxy carboxylic acids, or from a combination of AA and BB difunctional monomers resulting in the formation of a small byproduct, e.g., water [6,7]. Basically, examples of polycondensation reactions, which proceed using difunctional monomers are the esterification of diacids with diols, diacid chlorides with diols or the ester interchange reaction of diols with diesters (Figure 2) [3,8–10].
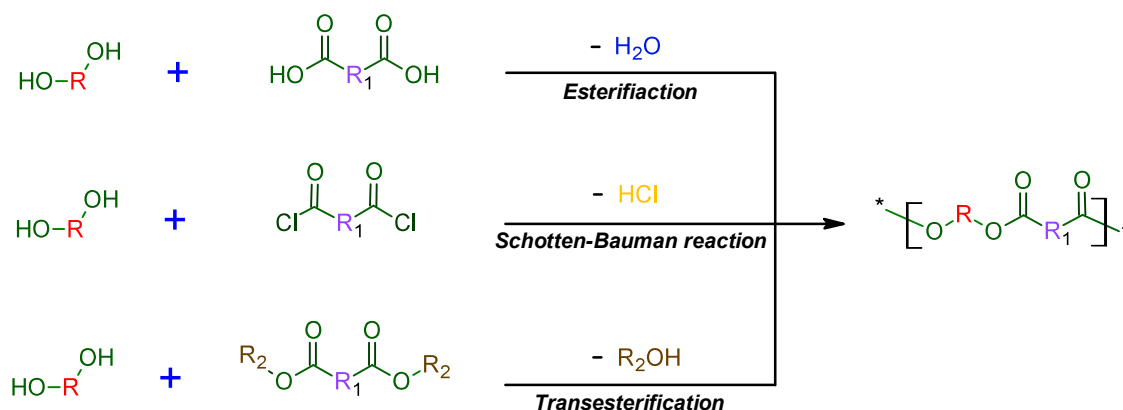
Figure 2. Examples of stepwise polycondensation reactions for the preparation of polyesters [10].

The pioneering studies of Carothers in the 1930s [11,12] on kinetics of polycondensation provided the first insights on the fundamentals analysis of step polymerization kinetics. It was defined by his equation that high molecular weight polymers ($\overline{X}_n > 50$) could be achieved only at a very high degree of conversions ($p > 98\%$–99%).

$$\overline{X}_n = \frac{1}{1-p} \tag{1}$$

Therefore, the formation of the ester group during the polymerization process is characterized by an equilibrium reaction (Figure 3) and in order to prepare high molecular weight polymers, two major prerequisites must be fulfilled [13,14]. Firstly, the equilibrium constant of polycondensation (K_P) must be sufficiently high and secondly, according to Equation (2) in case of heteropolycondensation (e.g., dialcohols and dicarboxylic acids) the stoichiometry (1:1) must be strictly obeyed.

Figure 3. The equilibrium constant of polycondensation reaction of carboxylic acids with alcohols [10].

The number average degree of polymerization ($\overline{X}_n$) in this case is associated to K_P through the derivation of Equation (2) and K_P values around 10 were generally found for a condensation reaction of aliphatic alcohols with carboxylic acids [7].

$$K_p = \frac{[-C(O)O-][H_2O]}{[-C(O)OH][HO-]} \tag{2}$$

Thus, according to Equation (3) values of $\overline{X}_n$ around 4 for $K_P \approx 10$ drives the polymerization reaction to the equilibrium.

$$\overline{X}_n = K_p^{0.5} + 1 \tag{3}$$

In general K_P must be increased to values higher as 2400 during the reaction since polyesters with $\overline{X}_n > 50$ is required to fulfill the basic physical properties of the polymer. In this case removal of the by-product (e.g., water) [15] from the reaction, the use of a catalyst [16–18] and high temperature settings (180–250 °C) [19,20] are some of the usual strategies applied in order to drive the reaction equilibrium toward high K_P values resulting in higher conversion rates. However, one of the main drawbacks in the polycondensation reaction is given by Equation (4). According to it the increase in the conversion (p) leads also to the increase in the polymer dispersity ($\overline{X}_w/\overline{X}_n$). Thus, at high conversions ($p > 98\%$–99%) the polymer $\overline{X}_w/\overline{X}_n$ has the tendency to approach 2 as a value [11,21].

$$\left. \begin{array}{l} \overline{X}_n = \frac{1}{1-p} \\ \overline{X}_w = \frac{1+p}{1-p} \end{array} \right\} \frac{\overline{X}_n}{\overline{X}_w} = 1+p \tag{4}$$

Nowadays, is with no doubt that ROP polymerization (e.g., of cyclic glycolide, lactides and lactones, Figure 4) is one of the most employed polymerization routes in order to circumvent the drawbacks from the polycondensation. The ROP polymerization processes several advantages compared to traditional condensation polymerization, e.g., high conversion without the necessity of removal of reaction byproducts, shorter reaction times, mild synthetic conditions and the use of a stoichiometric balance of monomers. Moreover, the ROP polymerization sometimes proceeds in a "living" manner, without side reactions, which allows good control of the polymer characteristics (narrow molecular weight distribution and predictable final molecular weight of polymer) [6,10,22]. All these remarkable advantages make ROP the method of choice for the preparation of high-molecular weight aliphatic homo- and copolyesters.
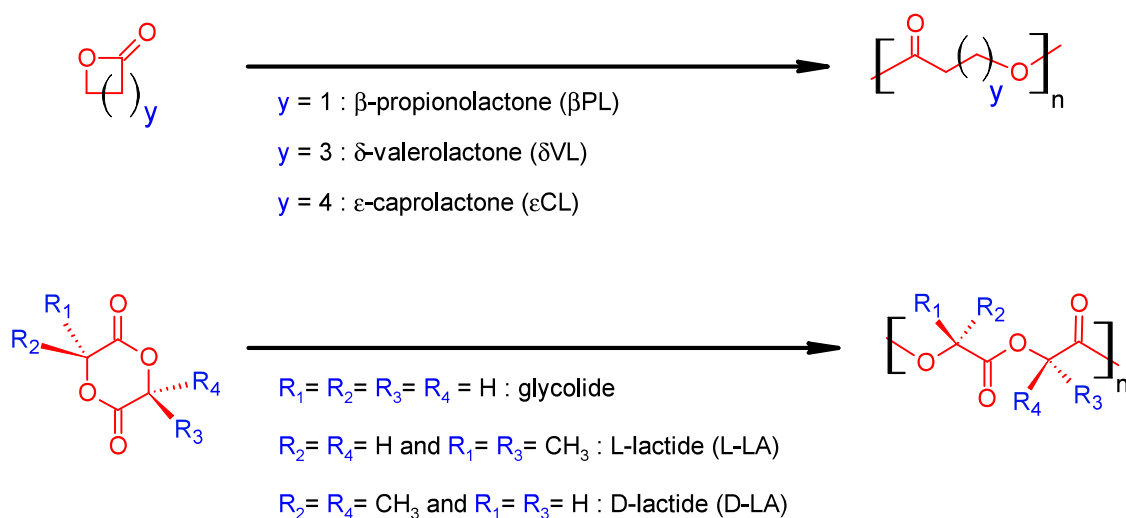
Figure 4. Monomers of choice for ring opening polymerization (ROP) polymerization [10].

ROP is a very flexible synthetic route and allows the use of several mechanistic approaches such as cationic, anionic, as well as coordinative catalyst or initiators have been reported [23,24]. In general, ionic (free ions and non-bulky ion pairs) are much more reactive and in the case of polyester inter and intra-molecular transesterification occurs lowering the molecular weight and broadening the molecular weight distribution of the polymer [10,25]. Otherwise, organometallic compounds of metals (Al, Sn, Ti or Mg) are more energetically favorable in comparison to their anionic counterparts and able to provide full control to the polymerization. Taking into account the several mechanisms involved in the ROP the two major proceeds using organometallics that are acting as initiators or as catalysts. In the cases where it is used as an initiator the polymerization proceeds through an "insertion-coordination" mechanism (Figure 5a) and when it is used as catalyst (Figure 5b) the polymerization is initiated by any nucleophile present in the polymerization medium.
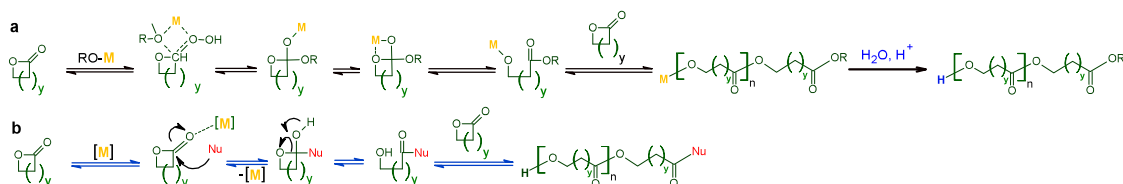
Figure 5. Mechanism of ROP of lactones using organometallics [M] as (**a**) an initiator in the "coordination-insertion" mechanism and (**b**) as a catalyst in the presence of nucleophiles (Nu) [10].

The third route to obtain polyester under mild conditions is using enzymatic polymerization. This method avoids the use of toxic reagents and allows the recycling of the catalyst. Moreover, regional and stereo selectivity of enzymes allows the direct synthesis of functional polyesters avoiding the use of protected monomers and block copolymers. However, the production of polymers with relatively low molecular weight is still a major drawback in the application of enzymatic polymerization on the synthesis of polyesters.

Nowadays, aliphatic polyesters constitute one of the most important classes of synthetic biodegradable and biocompatible polymer intended for biomedical applications [10,26,27]. Most of them are commercially available in several types, some examples of FDA-approved aliphatic polyesters are polycaprolactone (PCL) [28,29], poly(glycolic acid) (PGA), poly(ʟ-lactic acid) (PLA) [30,31] and poly(lactic-co-glycolic acid) (PLGA) [32]. They have been extensively studied for their biocompatibility [33–36], biodegradability [37,38] and bioresorbability [39]. It is very well established that they are highly biocompatible materials [40], easily hydrolysable into human body [41–43] and therefore they can be used for biomedical applications in the production of drug carrier devices for

controlled release [44–47]. Between the FDA-approved synthetic biodegradable and biocompatible polymers, poly(alkylene succinate) based polyesters has also proven to be an interesting alternative on the production of biomaterials for a myriad of applications [15,48–53]. Since they are free of cytotoxic degradation products, e.g., succinic acid, which is an intermediate in the TCA cycle (tricarboxylic acid cycle, citric acid cycle), makes poly(alkylene succinates) potential candidates as biomaterials on the development of drug delivery structures [54–57]. Moreover, the copolymerization of alkylene succinates with fatty acids (naturally occurring body compounds) [58,59], such as dilinoleic acid, allow the preparation of more hydrophobic biodegradable polymers. These more hydrophobic polymers are suitable for fine-tune hydrophobic drugs encapsulation via polymer–drug interactions when, for example, these polymers are used as drug nanocarriers [8,9,53,60,61].

### 1.2. Drug Release from Polyesters in General

The potential to protect the active drug component from degradation together with sustaining their release, as well as the capability to modulate the active drug diffusion and polymer degradation resulting in inert body-friendly degradation byproducts, make polyesters successful candidates for drug delivery systems in biomedical applications. The encapsulation of drugs into polyester-based nanosystems, subsequent drug release and to some extent also polymer degradation are generally dependent on the polymer/matrix interaction with the dissolved (compound at the amorphous state) or dispersed (compound at crystalline state) drug [8,62,63]. This is directly related to the solubility (for the crystalline host molecules) and/or miscibility (for the amorphous load) of the drug with the polymer matrix and vice-versa. The polymer crystallinity can also play an important role for the encapsulation, drug release and degradation. Some studies reported that the drug loading decreased with the increase of polymer crystallinity and the glass transition temperature (T_g) [14,63–65], other studies reported that the drug loading capacity for polyester nanoparticles can be significantly enhanced by hydrophobic effects between the polymer and the drug and in combination with hydrogen bonding, electrostatic interaction and dipole–dipole interactions modifying the drug release profile [66–68]. In addition, the degradation behavior of the polyester matrix is an important prerequisite for the potential drug release. There are two main mechanisms involved in the degradation of polyesters and they are dependent on the relative rates of water diffusion into the polymer matrix and on the polymer degradation rate [8,62]. In the case where the rate of polymer degradation is faster than the rate of water diffusion into the polymer matrix the mechanism is called surface degradation. On the contrary, when diffusion of water into the matrix is faster than polymer degradation and the whole matrix is affected by degradation and erosion, the process is called bulk degradation. In general, under biological conditions (in vitro and in vivo) the degradation of polyesters without specific responsive linkage (described in detail hereafter) proceeds by random hydrolytic cleavage of ester linkages.

2. Polyesters with Stimuli-Sensitive Linkages

2.1. pH-Labile Polyesters

The pH-labile polyesters have found a wide range of applications in drug release for diseases where certain pH shift from the physiological pH is observed. Typically, the polymer degradation may be selective in this way in cancer and inflamed tissues (in the case of inflammation, the presence of reactive oxygen species is also used for specific drug release or polymer degradation, see below) [62]. While in the healthy tissues the pH value is around 7.4, in the cancer and inflamed tissue the pH value is significantly lower—around 6.5 [69]. It has also been shown that some cell compartments such as lysosomes or endosomes exhibit lower the pH to between 5 and 6 [70,71]. Many pH-labile systems have been developed so far and there is always a pH-sensitive functional group present in the structure. The most common bonds with such properties are the hydrazone bond [72–77], amine/imine groups [78,79], acetals/ketals [80,81], ortho esters [82,83], *cis*-aconityl group [84,85], etc. The selected pH-sensitive linkages are shown in Figure 6.
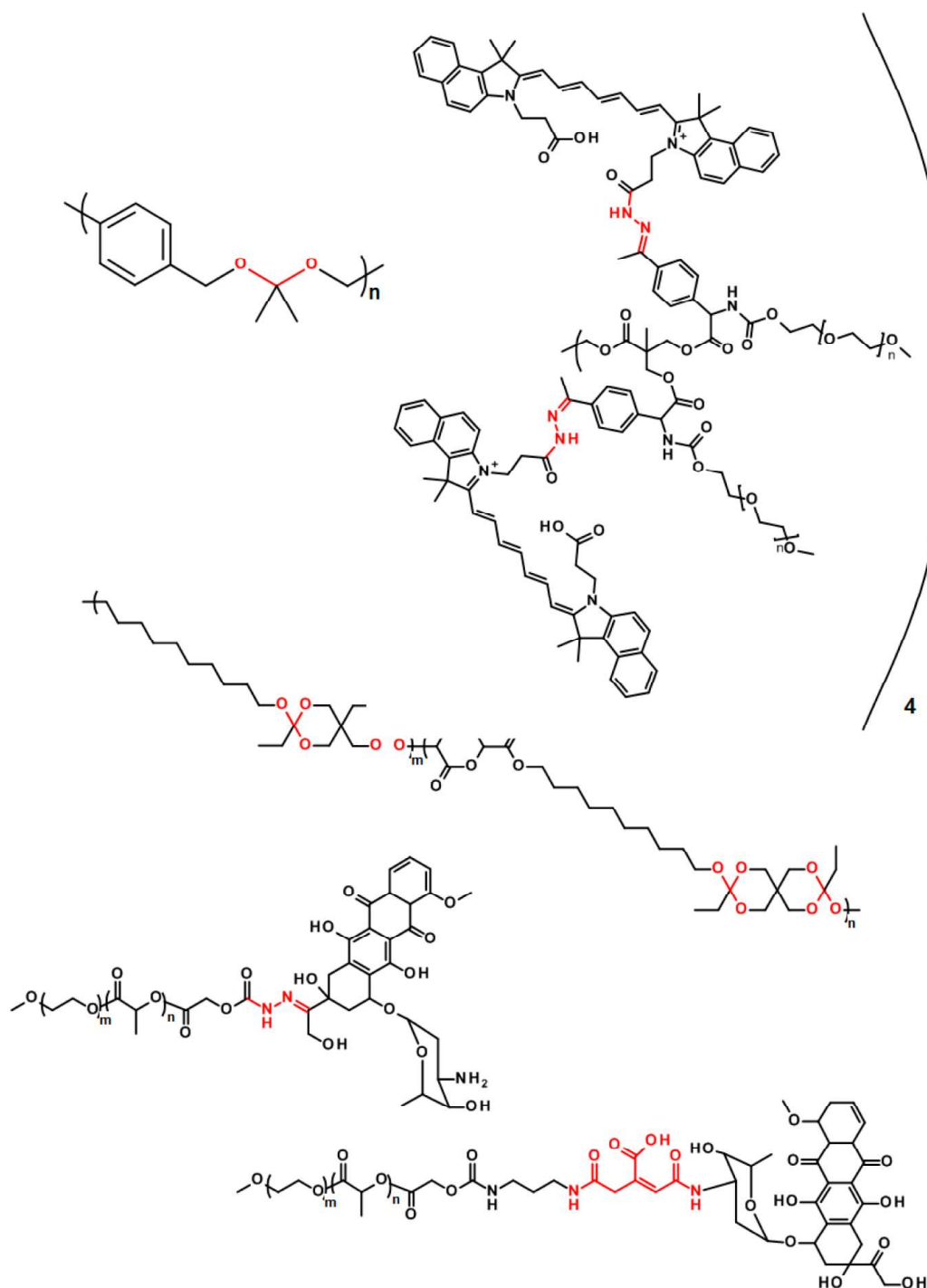
Figure 6. Polymer structures with pH-sensitive linkages.

The well-known pH-sensitive linkage hydrazide/hydrazone has become one of the most popular pH-sensitive linkages in drug delivery systems. The pH-sensitivity in compact biodegradable aliphatic polyester dendrimer has been observed by near-infrared (NIR) fluorescence [77]. The NIR fluorophore cypates have been attached to the PEGylated polyester dendrimer via a hydrazone bond. The hydrazone bond is stable in neutral pH so the dye sits on the dendrimer. The activation of the NIR fluorescence occurs when the dye is cleaved off the dendrimer in the acidic pH. In addition, the dendrimer scaffold can be enzymatically degraded by endogenous esterase.

The PES-like polyketal particles have been described for the controlled drug release systems. Due to their easy synthesis they hold promises for further development. The system based on poly(1,4-phenyleneacetone dimethylene ketal) has been designed as a pH-sensitive drug carrier. It has been shown that the degradation time of the polyketal backbone undergoes three times faster in acidic conditions (pH 5.5) compared to the physiological conditions (pH 7.4). In addition, the loading with the hydrophobic drug has been successfully done, so the loaded biodegradable drug vehicles have been proposed for therapeutic treatment involving phagocytosis by macrophages [86].

The pH-lability of orthoester bond has been described in the literature [87]. The current trend of designing very specific systems for individual applications has motivated the research group at the University of Minnesota to prepare double responsive copolymer where along the pH sensitivity due to the orthoester group, the amide group is incorporated to introduce the temperature-responsivity, too. The sol–gel transition temperature (Tt) is highly depending on the polymer structure so the Tt can be set up precisely and the pH-lability in the acidic environment is maintained [83].

The comparison of pH lability of hydrazone and *cis*-aconityl linkage has been done in the study where the doxorubicin was attached to the diblock copolymer composed of poly(L-lactic acid) and methoxy-poly(ethylene oxide) via these pH labile bonds and the degree of release has been evaluated [85]. Although both linkages have cleaved in the acidic environment, the *cis*-aconityl bond showed higher lability, which led to faster drug release. However when the drug was measured at pH 7, the *cis*-aconityl bond exhibited higher stability.

2.2. Reductively Labile Polyesters

There are two main approaches for the construction of reductively degradable drug delivery systems. They utilize (i) the reduction of the disulfide bond by glutathione specifically in cancer cells and (ii) the bacterial reduction of aromatic azo-dye, which allows for colon-selective degradation [88,89].

The azo group is well known for the photosensitive properties in organic chemistry. The Z-configuration can be easily switched to a more stable *E*-configuration by specific wavelength irradiation [90]. In the polymer chemistry, the reduction of azo group is taken in advantage and it is widely used for drug delivery systems. It highly depends on whether the azo linkage is part of the backbone or it occurs in the side group for the reduction. It has been observed that the azo linkage incorporated in polymeric backbone degrades slower [88,89,91]. The difference in the degradation mechanism has been noticed when aromatic (Figure 7) and aliphatic polymers were compared—the aliphatic azo compounds such as azobis(isobutyronitrile) undergo a rather nitrogen-releasing thermal or photoinduced decomposition than bioreduction. The azo bond is known for the ability to be reduced by intestinal microflora [92]. There are also polyester systems containing a reductively labile azo group. These polyesters containing the azo linkages can be used in colon-specific therapy [93–95]. Most precisely, the aromatic poly(ether-ester) has been synthetized by classical polycondensation of 4-[(4-hydroxyphenyl)azo]benzoic acid and its derivatives. These poly(ether-ester)s are well degraded by azoreductase—enzymes located in the intestinal bacteria and therefore they were suggested as the carrier for colon-specific drug release [93].
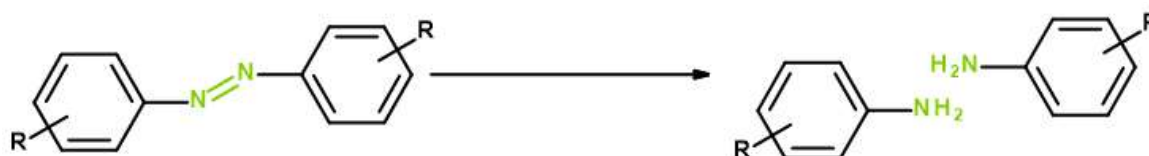

Figure 7. The reductive cleavage of azo-dye linkage.

A considerable number of systems have been invented for drug specific release at the cancer tissue with the use of the disulfide bond. The reason why the disulfide bond is often used is that the cancer environment shows a more reductive potential compared to healthy tissue due to lower oxygen partial pressure in such tissues. This shift in redox potential is connected with higher concentration of reduced

glutathione (GSH) [96]. In general, also the intracellular environments exhibit higher concentrations of GSH compared to the extracellular (1–10 mM vs. 1–10 μM) [97]. While GHS occurs in the reduced form in the intracellular compartments, in extracellular rather in the oxidized form [98]. Therefore this system based on GSH has been widely used not only in target drug release [99,100] but also in gene delivery [101–104].

There is more than one physiological function of GSH in organisms. Beside it being an antioxidant agent, which prevents the damage caused by reactive oxygen species, it also serves as the reducing agent, particularly for the disulfide bond [105]. The GSH donates its electrons to the proteins connected by a disulfide bond or to the protein, which has an intramolecular disulfide connection and oxidizes itself to glutathione disulfide. This phenomenon can be taken advantage of in drug design and many researchers have suggested polyester systems containing a disulfide bond as a drug carrier aiming at specific release or polymer degradation on cancer cells. The mechanism of the GSH oxidation in the presence of a polyester drug carrier containing disulfide linkage is shown in Figure 8.
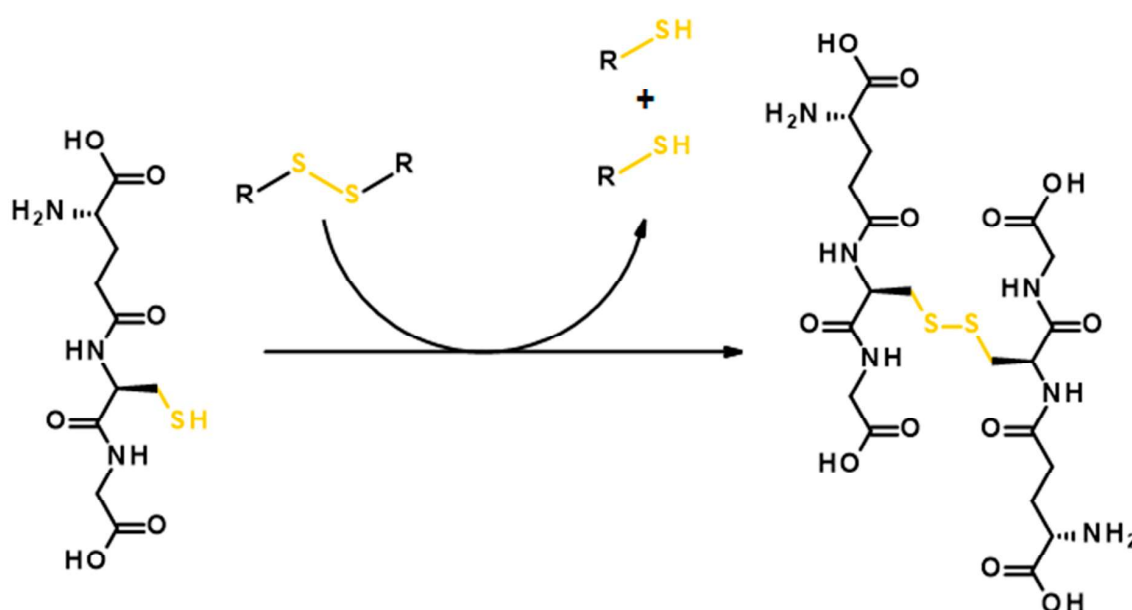
Figure 8. The scheme of reductive degradation of the disulfide bond with glutathione.

The strategy of Shen's research group was to prepare such micelles, which would be stable in the blood stream (would not disintegrate into unimers there) so the disintegration will occur in the cancer cells, specifically. They design stimuli sensitive crosslinkable micelles based on a hydrophobic polyester core with reversible disulfide crosslinking points and hydrophilic poly(ethylene oxide) shell. Their synthetized micelles loaded with paclitaxel showed high stability in circulation and due to the cytoplasmic glutathione, the paclitaxel release was targeted in cancer cells, preferably [106].

In the study of Prof. Farokhzad et al. [107], the system based on poly(ether ester) with introduced disulfide linkages was compared with a system where the disulfide linkages were missing. Even though the systems exhibit very similar properties such as the ability of nanoparticle formation and dye and drug encapsulation, the system containing disulfide linkages was much more sensitive to the introduced reducing agents and thus the dye release was much faster. Not surprisingly, the cell viability was reduced by the drug-loaded reduction-sensitive nanoparticles compared to reduction-insensitive nanoparticles with a comparable amount of drug [107].

2.3. Reactive Oxygen Species (ROS)-Labile Polyesters

The importance of ROS that it is involved in several pathological sates and cellular signalization have attracted great attention towards the development of chemical tools for specific delivery

to ROS-rich niches, and ROS-responsive micro-or nano-delivery systems. Delivery systems that are capable of targeting and releasing active molecules (chemotherapeutics, antigens, adjuvants, antioxidants, proteins, etc.) at sites of high ROS expression have the potential for high biological impact. The capability to generate a triggered polymer response (e.g., to deliver cargo or to induce polymer self-immolation/degradation) at ROS rich sites has received particular interest, e.g., for the preparation of delivery system targeting the tumor microenvironment and inflammation sites. Several ROS-responsive polyesters were designed based on oxidatively cleavable linkers such as thioethers, selenium-containing bonds, phenylboronic acid esters and aryl oxalates—schematically shown in Table 1. In this section, we will systematically describe ROS-responsive polyesters that have been mostly developed so far from those moieties and their nanoparticles (NPs) preparation and characterization with the proof-of principle tested in in vitro and in vivo models.

2.3.1. Poly(propylene sulfide)s

Poly(propylene sulfide)s have been one of the most investigated classes of ROS-responsive polyesters. Due to their very low dipole moment, in the presence of oxidative conditions, poly(propylene sulfide)s containing polymers undergo a phase transition from hydrophobic sulfide to a more hydrophilic sulfoxide or sulfone [108,109]. Oxidation, for example, by H_2O_2, would be a trigger that converts the polyester from hydrophobic to hydrophilic resulting in morphological transitions, swelling, solubilization or release of the entrapped molecules.

Table 1. Representative oxidation-responsive polyesters and their oxidation products.

ROS-Sensitive Materials	Chemical Structure and Oxidation	References
Poly(propylene sulfide)s		[109–119]
Selenium containing polyesters		[120–124]
Arylboronic ester containing polyesters		[125–127]
Polyoxalates		[128–135]

Poly(propylene sulfide)s can be produced by several techniques such as propagation reactions producing main-chain thioethers from thiols or from cyclic strained thioethers comprising step-growth polymerization mechanism or most recently by "living' radical polymerization such as the ROP of episulfides that provides amphiphilic block copolymers [108]. One example is the pioneer synthesis of symmetric amphiphilic triblock copolymer of ethylene glycol and propylene sulphide (named PEO-PPS-PEO) described by Hubbell's group in 2004 [110]. The triblock copolymer comprises the hydrophobic block of poly(propylene sulphide) (PPS), owing to its extreme hydrophobicity, its low glass-transition temperature and most importantly its oxidative conversion from a hydrophobe to a hydrophile, poly(propylene sulphoxide) and ultimately poly(propylene sulphone) undergoes self-assembly into polymer vesicles where the presence of H_2O_2 induces a morphological change of otherwise highly stable vesicles to worm-like micelles, then to spherical micelles and ultimately to non-associating unimolecular micelles. Poly(propylene sulfide) nanoparticles also can be directed synthesized by anionic ROP emulsion polymerization [111,112]. By this synthetic strategy Allen et al., synthesized poly(propylene sulfide) NPs with the addition of hydrophobic solvatochromic dyes

such as Reichardt's dye or fluorescent dyes such as Nile red dye during the polymerization process resulting in their stabilization in aqueous media by encapsulation. Subsequent addition of H_2O_2 or low levels of sodium hypochlorite (NaOCl), causes particle oxidation followed by particles swelling and release of cargo. Furthermore, it was demonstrated that this oxidative release could be facilitated through peroxidase enzyme oxidant generation. Chloroperoxidase (CPO) and human myeloperoxidase (hMPO) enzymes in the presence of 200 mM NaCl and 500 μM H_2O_2, generate hypochlorous acid (HOCl), which oxidizes the poly(propylene sulphide) NPs and causes the release of the encapsulated cargo. Taking advantage of this oxidation-mediated transition, various ROS-sensitive structures based on polysulfides such as micelles [113,114], microspheres [115], vesicles [110] and hydrogels [116] have been synthesized and their proof-of-principle tested as delivery agents for antioxidant [115], chemotherapeutic [117] and immunomodulatory [113,118] compounds.

2.3.2. Selenium-Containing Polyesters

Diselenide-containing polymers have been developed because they attractive rapid ROS response kinetics and their sensitivity to oxidation–reduction, which makes them promising candidates for a dual redox response. Similar to polysulfides in thioether-containing polymers (aforementioned), hydrophobic selenides are able to be oxidized to water soluble selenoxides and selenones [119]. In addition, selenium-containing polymers possess a higher sensitivity to oxidants because of the weaker bond energy of the C–Se bond compared with the C–S bond.

Usually selenides are prepared by step-growth polymerization synthesis resulting in polyester urethanes (polyurethanes) as block copolymers. One pioneer study was designed by Ma et al., where a diselenide containing polyurethane block was synthesized via polymerization of toluene diisocyanate in excess with diselenide-containing diols and posterior termination by PEG monomethyl ether. The new amphiphilic diselenide-containing triblock copolymer of ABA-type (named PEG-PUSeSe-PEG) could self-assemble in micelles cargo doxorubicin or rhodamine B with unique dual redox responsive behavior [120]. The loaded cargo was released either in the presence of H_2O_2 (0.01%) or glutathione (0.01 mg/mL) within a period of 5 h. In forthcoming work, these diselenide-containing triblock copolymers (PEG-PUSeSe-PEG) were also shown to be responsive to singlet oxygen [121]. Upon irradiation of PEG-PUSeSe-PEG micelles in the presence of porphyrin derivatives with a red light, the generated singlet oxygen oxidized the diselenide-containing block copolymers and cleaved the diselenide bonds resulting in the disassembly of the micelles and the release of the loaded Dox.

Selenide based polyesters were also prepared by ROP. Recently Yu at al., demonstrated the ROP of caprolactone for the preparation of selenide ROS-responsive poly(ε-caprolactone) (PCL)-type polyesters with pendant selenide motifs. The NPs prepared from this newly synthesized polyester containing pendant selenide groups respond much faster to H_2O_2 than NPs prepared by the same pathway (ROP of caprolactone), however containing thioether as pendant groups, most likely due to the superior sensitivity of the selenide pendant groups towards H_2O_2 [122]. In a straightforward approach, the synthesis of a variety of multi-responsive linear and cross-linked diselenide-containing polyesters was designed by Wang et al., from a novel one-pot two-step process consisting of a nucleophilic ring opening reaction of γ-butyroselenolactone with a wide range of alcohols, followed by a stepwise polymerization in situ ring opening/oxidation process [123]. By this pathway diselenide bonds can be easily introduced into several types of polyester architectures, avoiding thorough synthesis procedures and including dynamic diselenide intermediates.

2.3.3. Aryl Boronic Esters Containing Polyesters

Among the aforementioned oxidation responsive polymers, the preparation of polymeric systems sensitive to H_2O_2 through the cleavage of boronic ester compounds is a straightforward approach. Boronic ester compounds can be introduced to the motifs of polymeric NP's design and the cleavage leads to polymer backbone degradation followed by cargo release. With these strategies small hydrophobic chemotherapeutic agents can be released upon exposure to biologically relevant oxidative

conditions, e.g., from μM to mM concentrations of H_2O_2 [124–126]. Boronic ester based polyesters undergo oxidation with an insertion of oxygen to the linkage between boronic ester and the polyester chain or drug molecule of interest. In the presence of water this linkage undergoes hydrolysis resulting in the cleavage of the boronic ester linkage and subsequently polymer degradation or molecules release.

Several boronic ester polymer derivatives have been studied for ROS-responsivity among which aryl boronic esters with either ester or ether linkages show superior ROS-dependent degradation kinetics. This was demonstrated in one study designed by de Garcia Lux et al., where two new polymers were designed differing with respect to the linkage between the boronic ester group and the polymeric backbone: Either direct or via an ether linkage. The polymers were synthesized by polycondensation reaction using adipic acid as a co-monomer. NPs encapsulating a model of hydrophobic probe, Nile Red (NR), were formulated and the degradation kinetics of the polymer NPs was studied by monitoring the release of the model probe under varying concentrations of H_2O_2. The NPs formulated from the polymers of arylboronic esters with ether linkages have shown to be extremely sensitive to H_2O_2 at concentrations ~50 μM oppositely to the NPs formulated of arylboronic esters directly linked requiring about 1 mM H_2O_2 for the same amount of Nile Red released. The efficacy of the NPs to release the NR was probed upon incubation with activated neutrophils, simulating a physiologically relevant ROS-rich environment in vitro, where the NPs formulated from a polymer of arylboronic esters with ether linkage showed a two-fold enhancement of release if compared with the NPs with directly linked arylboronic esters while controls showed a nonspecific response to ROS producing cells [125]. In a similar approach, Jäger et al., prepared polymers containing phenylboronic esters and monomers bearing alkyne moieties for the attachment of fluorescent dyes via polycondensation reaction. The polymers were intended for the monitoring of the polymer fate in vitro. The polymers display triggered self-immolative degradation in the presence of ROS with the capability of cellular imaging. This was demonstrated after preparation of NPs encapsulating the fluorescent model probe NR (NR is fluorescent in the hydrophobic environment with quenched fluorescent in aqueous medium due to polarity changes in the micro-surrounding). The quenching of the NR probe was much higher in prostate cancer cells (PC-3 cells) compared to in Human fibroblast cells (HF cells). Moreover, the quenching of the NR was 2.5 times higher in PC-3 cells for the ROS-responsive polymer when compared with the NR quenched from one prepared polymer counterpart (without the phenylboronic ester monomer). These studies indicated that ROS-induced polymer degradation and NR release demonstrating the polymer's potential for specifically release the cargo in ROS-rich intracellular environments. Further the authors covalently attached a fluorescent dye Alexa-Fluor 647 azide (Alx) by click-chemistry and monitored simultaneously the polymer degradation and the NR release in different cells by fluorescence life-time images (FLIM) and compared with the polymer counterpart. After 8 h incubation the NR and the Alx-bounded to the ROS-responsive polymer were co-localized to a high extent in HF cells whereas the cytoplasm was more homogeneously colored with the released NR observed in ROS-producing PC-3 cells. Finally the chemotherapeutic drug paclitaxel (PTX) was loaded, and enhanced in vitro cytotoxicity was observed for H_2O_2-responsive particles compared to the counterpart polymer-loaded to PTX (non-responsive to H_2O_2) in three different cancer (PC-3, HeLa and DLD1) cell lines [126].

2.3.4. Polyoxalates

Oxalate based polyesters has been well known for being easily, quickly and specifically oxidized by H_2O_2 to form the corresponding alcohols and 1,2-dioxetanedione or other kinds of high energy intermediates, which can rapidly react with an appropriate fluorophore molecule to form an activated complex. After decomposition of the complex along with CO_2 release, the excited fluorophore decays to the ground state with a fluorescent emission [127,128]. Thus, strategically placing aryloxalate ester bonds within polymeric NPs backbones is a particularly straightforward approach that can induce their degradation and release the cargo upon exposing to H_2O_2. In this way, polyoxalate polymers are usually prepared in one-pot synthetic pathway by polycondensation reaction. This strategy was explored

for example by Lee et al., via the condensation reaction of oxalyl chloride with 4-hydroxybenzyl alcohol and 1,8-octanediol. Polyoxalate NPs were prepared by the oil/water (o/w) emulsion technique encapsulating different fluorescent dyes (perylene, rubrene or pentacene). Upon exposure to H_2O_2, the polyoxalate NPs degraded along with high energy intermediates production and subsequent dye emission showing high sensitivity to H_2O_2 in vitro over a linear range from 0.25 to 10 mM. The Pentacene-loaded polyoxalate NPs were capable of imaging hydrogen peroxide in the peritoneal cavity of mice during a lipopolysaccharide-induced inflammatory response in a mouse leg [127].

In a similar approach, Kang et al., designed H_2O_2-responsive copolymer NPs with strong antioxidant properties for therapeutic and diagnostic purposes based on the utilization of p-hydroxybenzyl alcohol (HBA), oxalyl chloride and 1,4-cyclohexanedimethanol. HBA is a major active pharmaceutical ingredient in *Gastrodia elata* Blume, which has been widely used as herbal agents for the treatment of oxidative stress-related diseases. These newly synthesized HBA polyoxalate NPs undergo complete H_2O_2-mediated degradation, releasing the active form of HBA and exerting its therapeutic effect demonstrated in in vitro experiments by using LPS-activated RAW 264.7 cells. The HBA based polyoxalate NPs demonstrated strong antioxidant and anti-inflammatory activities by inhibiting the production of nitric oxide and reducing TNF-α levels [129]. In forthcoming work, Lee et al., prepared polyoxalate NPs comprising oxalyl chloride, 1,4-cyclohexanedimethanol and vanillyl alcohol (VA) as backbones building blocks. VA is also an active pharmaceutical ingredient in *Gastrodia elata* Blume with probed antioxidant and anti-inflammatory properties. These polyoxalate NPs containing VA were designed to degrade and release VA, which is able to reduce the generation of ROS, and exert anti-inflammatory and anti-apoptotic activity. The polyoxalate vanillyl NPs specifically reacted with overproduced H_2O_2 and exerted highly potent anti-inflammatory and anti-apoptotic activities that reduced cellular damages as demonstrated in models of hind-limb ischemia/reperfusion injuries in vivo [130]. By taking advantage of such a strategy, Jäger et al. re-utilized a chemotherapeutic drug withdrawn from market due to dose-related adverse effects. Via a one-pot condensation reaction new ROS-sensitive, self-immolative biodegradable polyoxalate prodrug based on the anticancer chemotherapeutic hormone analog diethylstilbestrol was synthesized. The NPs prepared from the diethylstilbestrol prodrug undergoes self-immolative degradation releasing diethylstilbestrol in ROS-rich niches, e.g., in the cancer cells. This new ROS self-immolative diethylstilbestrol polymeric based prodrug circumvents the necessity of a linker between the polymeric chain and the chemotherapeutic drug, exhibiting more specific drug release and minimum adverse effects to non-ROS overproducing cells as demonstrated in in vitro experiments. Altogether these new NPs based on the diethylstilbestrol polymeric prodrug reduced the adverse effects of an effective and largely applied chemotherapeutic drug applied for hormone-dependent cancers [131].

Despite the use of oxalates as main building blocks agents, alternatively oxalate groups were also employed as pendant phenyl alkyl hybrid oxalate groups in a polynorborene-type copolymer with oligo(ethylene glycol) chains synthesized by ring-opening metathesis polymerization for the preparation of ROS-sensitive micelles [132]. They were also used as block linkages between a PLGA and a poly(ethylene glycol block) in a AB-type amphiphilic ROS-triggered nanoparticle-based antigen delivery system with pronounced vaccine-induced immune responses in vivo [133]. Recently, they increase the degradation kinetics profile of polycaprolactone. In the latter case, oxalyl chloride was reacted with α,ω-dihydroxy oligocaprolactone to generate an oligocaprolactone multiblock copolymer-oxalate. Microspheres prepared form the new PCL-oxalate copolymer were completely cleared two months after in vivo implantation in the mice model demonstrating similar degradation rate as the PLGA microspheres prepared as controls [134].

2.4. Enzymatically Labile Polyesters

The aliphatic polyesters excel in the biodegradation processes among the polymers. It is given by the nature of the chemical structure because the ester bond undergoes a hydrolysis reaction readily. The rate of the process is very slow in the mild condition but it rises up when the temperature increases,

the pH of solution deviates from neutral or, especially, when certain enzymes—the esterases—are present in the solution. This chemical process can cause troubles in material applications in respect of the loss of mechanical properties. However, when considering application as stimuli-responsive polymers where the degradation process is desirable, the hydrolysis can play a crucial role in the system. The polymeric materials for drug delivery applications are deliberately designed from degradable polymers so the encapsulated drug is released with the respect of the mass loss given by the rate of degradation [135,136].

The rate of the enzymatic hydrolysis can be tuned by the chemical structure and physical properties of the polyester. In addition, the polymer structure is often intentionally designed and synthetized in the way of faster degradability for these applications. The degradability of aliphatic polyesters generally increases with a lower content of the crystalline structure and it can be done by the introduction of irregularities to the polymeric structure e.g., by the presence of the side groups [137].

The very important factor in the enzymatic degradation is the enzyme itself. It is well known that the enzymes serve as selective biocatalysts in living systems. Many enzymes became very substrate-selective during evolution (e.g., polymerases). On the other hand, there are enzymes that do not exhibit such strict selectivity [138]. The digestive enzymes break down the macromolecules in the nutrients so the need of accurate scission is not essential as it is in the case of reproduction. In addition, there are several digestive enzymes that have the same effect but the kinetics changes depending on the nature of the substrate. It was already demonstrated in many publications, e.g., the rate of enzymatic degradation of polyester backbone in poly(ethylene oxide)-block-poly(ω-caprolactone) was significantly faster when the bacterial lipase from *Pseudomonas* sp. was used compared to the porcine pancreatic lipase [139].

The rate would differ in different environments, in medical terms—in different biological compartments. Therefore, the polyester-based polymers have become very popular in the smart drug delivery systems. The elevated concentration of hydrolases with the combination of lowered pH in some biological compartments such as, for example, in endosomes or lysosomes would cause an increased degradation rate of ester bond. The rate of the enzymatic hydrolysis is very individual because of the enzyme specificity, as mentioned above [140,141].

In the study of Trousil et al., the self-assembled nanoparticles based on poly(ethylene oxide)-block-poly(ω-caprolactone) were loaded with rifampicin, a first-line antituberculotic agent and cornerstone of modern antituberculotic therapy. It was shown that the degradation rate depends not only on the nature of the substrate but also on the blocks' sizes and the final nanoparticles' sizes and their distribution, suggesting that the nanobead-based intervention's trafficking is a complex phenomenon. Despite this fact, some trends in the relationships have been seen. What is more, the antituberculotic effect has been demonstrated both in vitro and in vivo. Using a well-established in vitro model of infected macrophage-like cells, it was found that the polyester-based nanoparticles are safe and able to suppress the virulent mycobacterial strain H37Rv-caused infect. Additionally, *Mycobacterium marinum*-infected zebrafish embryos were used to assess the treatment effect in vivo. The zebrafish larvae treated by the rifampicin-loaded nanobead-based intervention have shown higher survival values in Figure 9. Given these results, it is believed that these kinds of nanoparticles have a potential for the treatment of intracellularly persisting bacteria-caused infections such as tuberculosis due to passive targeting to macrophage-like cells. The enzymatic degradation of the polyester part of nanoparticles causes the drug release in the endosomes so the drug gets closer and at a higher concentration at the site of the mycobacteria-caused infection. Hence, the treatment is more efficient [142].
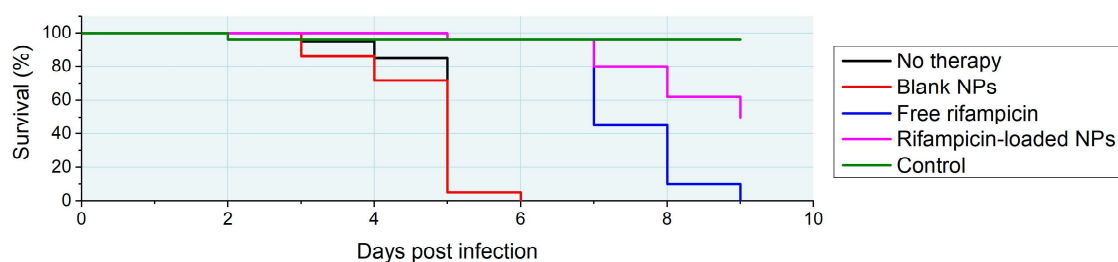
Figure 9. In vivo testing of antituberculotic nanobead-based intervention. Zebrafish larvae were infected with *Mycobacterium marinum* and treated with free rifampicin, rifampicin-loaded nanoparticles and blank nanoparticles at a dose of 10 mg/kg. Cumulative mortality is shown. Modified based on data from reference [142].

Altogether the potential application of the selectively biodegradable polyesters mentioned along the manuscript is summarized in Table 2.

Table 2. Selectively biodegradable polyesters and their biomedical applications.

Polyester	Sensitive Linkage	Biomedical Application	References
pH-sensitive	Ketal	Anti-inflammatory drug (Dexamethasone);	[80]
	Orthoester	Injectable drug release device, Cell scaffold;	[77]
	Cis-aconityl	Chemotherapy (Doxorubicin);	[79]
Reductive-labile	Azo groups	Colon therapy (Imaging);	[86]
	Disulfide	Chemotherapy (Paclitaxel);	[99]
	Propylene sulfide	Chemotherapy (Doxorubicin);	[109]
	Propylene sulfide	Vaccination (antigens);	[105]
	Propylene sulfide	Chemotherapy (Paclitaxel);	[107]
ROS-labile	Selenide, diselenide	Chemotherapy (Doxorubicin);	[112,113]
	Aryl boronic esters	Chemotherapy (Paclitaxel);	[118]
	Oxalate	Chemotherapy (Dyethylstilbestrol);	[123]
	Oxalate	Antioxidant and anti-inflammatory (Vanilyl alcohol);	[122]
Enzymatically-labile	Ester bond	Antituberculotic (Rifampicin);	[134]

3. Conclusions

Degradable polyesters have been subject of great attention along decades because of their nature characteristics and because they can be degraded into smaller, biocompatible molecules that are easily cleared via conventional paths, such as renal filtration and hepatic metabolization. With the advances in polyester synthesis, several polymers were built-up with varied morphologies, stereocomplexations, chemical compositions and with different degradation profiles. Major progress in the field of degradable polyesters was achieved tailoring the polymers to be responsive to changes in physiological conditions. In this review we presented the state-of-the-art of the synthesis, structure-properties, degradation characteristics and biomedical applications of biologically responsive polyesters. Polyesters responsive to enzymes, to the changes on pH, reductive degradable polyesters and reactive oxygen species degraded polyesters were discussed in detail. These new stimuli-responsive polyesters were employed as biomaterials in several fields such as in surgery, tissue repair and regeneration, tissue engineering and sustained drug delivery systems for various kinds of bioactive molecules demonstrating their broad applicability, their success and the generally bright future of the field of stimuli-responsive polyester. However, progresses in the field are still necessary with more studies and methods for a better understanding of polyester degradation characteristics as well as for the development of novel degradable polyester devices for actual medical and pharmaceutical application challenges. With the enormous possibility of monomer selection and polymerization processes a multitude of polyesters can be designed with control over degradation, biocompatibility and physical properties to obtain diverse materials for biomedical applications. Furthermore, novel materials with several

different responsiveness' can be created by the combination of different monomers, which holds promises for several different applications. As demonstrated just from one small sort of responsive polyesters described herein, they offer a facile route to a plethora of materials with a variety of thermal, degradation and mechanical properties. Altogether, the development and production of synthetic selectively degradable polymers for applications as biomaterials is of the upmost importance for the advancement of effective biomedical therapeutics and the future of the field.

Conflicts of Interest: The authors declare no conflict of interest.

References

1. Sivaram, S.J.R. Wallace hume carothers and the birth of rational polymer synthesis. *Resonance* **2017**, *22*, 339–353. [CrossRef]
2. Kumar, M.N.V.R. *Handbook of Polyester Drug Delivery Systems*; Pan Stanford Publishing: Singapore, 2017.
3. Albertsson, A.-C.; Varma, I.K. Aliphatic polyesters. In *Biopolymers Online*; Wiley-VCH: Weinheim, Germany, 2005.
4. Ding, D.; Pan, X.; Zhang, Z.; Li, N.; Zhu, J.; Zhu, X. A degradable copolymer of 2-methylene-1,3-dioxepane and vinyl acetate by photo-induced cobalt-mediated radical polymerization. *Polym. Chem.* **2016**, *7*, 5258–5264. [CrossRef]
5. Sun, L.F.; Zhuo, R.X.; Liu, Z.L. Synthesis and enzymatic degradation of 2-methylene-1,3-dioxepane and methyl acrylate copolymers. *J. Polym. Sci. A Polym. Chem.* **2003**, *41*, 2898–2904. [CrossRef]
6. Edlund, U.; Albertsson, A.C. Polyesters based on diacid monomers. *Adv. Drug Deliv. Rev.* **2003**, *55*, 585–609. [CrossRef]
7. Duda, A.; Penczek, S. Mechanism of aliphatic polyester formation. In *Biopolymers*; Wiley-VCH: Weinheim, Germany, 2005.
8. Jäger, A.; Gromadzki, D.; Jäger, E.; Giacomelli, F.C.; Kozlowska, A.; Kobera, L.; Brus, J.; Říhová, B.; El Fray, M.; Ulbrich, K.; et al. Novel "soft" biodegradable nanoparticles prepared from aliphatic based monomers as a potential drug delivery system. *Soft Matter* **2012**, *8*, 4343–4354. [CrossRef]
9. Jäger, E.; Jäger, A.; Etrych, T.; Giacomelli, F.C.; Chytil, P.; Jigounov, A.; Putaux, J.-L.; Říhová, B.; Ulbrich, K.; Štěpánek, P. Self-assembly of biodegradable copolyester and reactive hpma-based polymers into nanoparticles as an alternative stealth drug delivery system. *Soft Matter* **2012**, *8*, 9563–9575. [CrossRef]
10. Albertsson, A.C.; Varma, I.K. Aliphatic polyesters: Synthesis, properties and applications. In *Degradable Aliphatic Polyesters*; Springer: Berlin/Heidelberg, Germany, 2002.
11. Carothers, W.H. Polymers and polyfunctionality. *Trans. Faraday Soc.* **1936**, *32*, 39–49. [CrossRef]
12. Carothers, W.H. Studies on polymerization and ring formation. I. An introduction to the general theory of condensation polymers. *J. Am. Chem. Soc.* **1929**, *51*, 2548–2559. [CrossRef]
13. Bikiaris, D.N.; Papageorgiou, G.Z.; Papadimitriou, S.A.; Karavas, E.; Avgoustakis, K. Novel biodegradable polyester poly(propylene succinate): Synthesis and application in the preparation of solid dispersions and nanoparticles of a water-soluble drug. *AAPS Pharmscitech* **2009**, *10*, 138–146. [CrossRef] [PubMed]
14. Bikiaris, D.; Karavelidis, V.; Karavas, E. Novel biodegradable polyesters. Synthesis and application as drug carriers for the preparation of raloxifene hcl loaded nanoparticles. *Molecules* **2009**, *14*, 2410–2430. [CrossRef] [PubMed]
15. Xu, J.; Guo, B.-H. Microbial succinic acid, its polymer poly(butylene succinate), and applications. In *Plastics from Bacteria: Natural Functions and Applications*; Chen, G.G.-Q., Ed.; Springer: Berlin/Heidelberg, Germany, 2010; pp. 347–388.
16. Yang, J.; Zhang, S.; Liu, X.; Cao, A. A study on biodegradable aliphatic poly(tetramethylene succinate): The catalyst dependences of polyester syntheses and their thermal stabilities. *Polym. Degrad. Stab.* **2003**, *81*, 1–7. [CrossRef]

17. Luo, S.; Li, F.; Yu, J.; Cao, A. Synthesis of poly(butylene succinate-co-butylene terephthalate) (pbst) copolyesters with high molecular weights via direct esterification and polycondensation. *J. Appl. Polym. Sci.* **2010**, *115*, 2203–2211. [CrossRef]

18. Jacquel, N.; Freyermouth, F.; Fenouillot, F.; Rousseau, A.; Pascault, J.P.; Fuertes, P.; Saint-Loup, R. Synthesis and properties of poly(butylene succinate): Efficiency of different transesterification catalysts. *J. Polym. Sci. A Polym. Chem.* **2011**, *49*, 5301–5312. [CrossRef]

19. Bikiaris, D.N.; Achilias, D.S. Synthesis of poly(alkylene succinate) biodegradable polyesters i. Mathematical modelling of the esterification reaction. *Polymer* **2006**, *47*, 4851–4860. [CrossRef]

20. Bikiaris, D.N.; Achilias, D.S. Synthesis of poly(alkylene succinate) biodegradable polyesters, part ii: Mathematical modelling of the polycondensation reaction. *Polymer* **2008**, *49*, 3677–3685. [CrossRef]

21. Gallardo, A.; San Román, J.; Dijkstra, P.J.; Feijen, J. Random polyester transesterification: Prediction of molecular weight and mw distribution. *Macromolecules* **1998**, *31*, 7187–7194. [CrossRef]

22. Jérôme, C.; Lecomte, P. Recent advances in the synthesis of aliphatic polyesters by ring-opening polymerization. *Adv. Drug Deliv. Rev.* **2008**, *60*, 1056–1076. [CrossRef]

23. Jérôme, R.; Lecomte, P. 4-new developments in the synthesis of aliphatic polyesters by ring-opening polymerisation. In *Biodegradable Polymers for Industrial Applications*; Smith, R., Ed.; Woodhead Publishing: Cambridge, UK, 2005; pp. 77–106.

24. Lecomte, P.; Jérôme, C. Recent developments in ring-opening polymerization of lactones. In *Synthetic Biodegradable Polymers*; Rieger, B., Künkel, A., Coates, G.W., Reichardt, R., Dinjus, E., Zevaco, T.A., Eds.; Springer: Berlin/Heidelberg, Germany, 2012; pp. 173–217.

25. Penczek, S.; Cypryk, M.; Duda, A.; Kubisa, P.; Słomkowski, S. Living ring-opening polymerizations of heterocyclic monomers. *Prog. Polym. Sci.* **2007**, *32*, 247–282. [CrossRef]

26. Albertsson, A.-C.; Varma, I.K. Recent developments in ring opening polymerization of lactones for biomedical applications. *Biomacromolecules* **2003**, *4*, 1466–1486. [CrossRef]

27. Jain, R.; Shah, N.H.; Malick, A.W.; Rhodes, C.T. Controlled drug delivery by biodegradable poly(ester) devices: Different preparative approaches. *Drug Dev. Ind. Pharm.* **1998**, *24*, 703–727. [CrossRef]

28. Dash, T.K.; Konkimalla, V.B. Poly-ε-caprolactone based formulations for drug delivery and tissue engineering: A review. *Off. J. Controll. Release Soc.* **2012**, *158*, 15–33. [CrossRef] [PubMed]

29. Woodruff, M.A.; Hutmacher, D.W. The return of a forgotten polymer—polycaprolactone in the 21st century. *Prog. Polym. Sci.* **2010**, *35*, 1217–1256. [CrossRef]

30. Garlotta, D. A literature review of poly(lactic acid). *J. Polym. Environ.* **2001**, *9*, 63–84. [CrossRef]

31. Raquez, J.-M.; Habibi, Y.; Murariu, M.; Dubois, P. Polylactide (pla)-based nanocomposites. *Prog. Polym. Sci.* **2013**, *38*, 1504–1542. [CrossRef]

32. Danhier, F.; Ansorena, E.; Silva, J.M.; Coco, R.; Le Breton, A.; Préat, V. Plga-based nanoparticles: An overview of biomedical applications. *J. Controll. Release* **2012**, *161*, 505–522. [CrossRef]

33. Idris, S.B.; Dånmark, S.; Finne-Wistrand, A.; Arvidson, K.; Albertsson, A.-C.; Bolstad, A.I.; Mustafa, K. Biocompatibility of polyester scaffolds with fibroblasts and osteoblast-like cells for bone tissue engineering. *J. Bioact. Compat. Polym.* **2010**, *25*, 567–583. [CrossRef]

34. Anderson, J.M.; Shive, M.S. Biodegradation and biocompatibility of pla and plga microspheres. *Adv. Drug Deliv. Rev.* **1997**, *28*, 5–24. [CrossRef]

35. Pamula, E.; Dobrzynski, P.; Szot, B.; Kretek, M.; Krawciow, J.; Plytycz, B.; Chadzinska, M. Cytocompatibility of aliphatic polyesters—In vitro study on fibroblasts and macrophages. *J. Biomed. Mater. Res. Part A* **2008**, *87*, 524–535. [CrossRef]

36. Knight, P.T.; Kirk, J.T.; Anderson, J.M.; Mather, P.T. In vivo kinetic degradation analysis and biocompatibility of aliphatic polyester polyurethanes. *J. Biomed. Mater. Res. Part A* **2010**, *94*, 333–343. [CrossRef]

37. Chandra, R.; Rustgi, R. Biodegradable polymers. *Prog. Polym. Sci.* **1998**, *23*, 1273–1335. [CrossRef]

38. Nair, L.S.; Laurencin, C.T. Biodegradable polymers as biomaterials. *Prog. Polym. Sci.* **2007**, *32*, 762–798. [CrossRef]

39. Vert, M.; Li, S.M.; Spenlehauer, G.; Guerin, P. Bioresorbability and biocompatibility of aliphatic polyesters. *J. Mater. Sci. Mater. Med.* **1992**, *3*, 432–446. [CrossRef]

40. Sokolsky-Papkov, M.; Agashi, K.; Olaye, A.; Shakesheff, K.; Domb, A.J. Polymer carriers for drug delivery in tissue engineering. *Adv. Drug Deliv. Rev.* **2007**, *59*, 187–206. [CrossRef] [PubMed]

41. Kretlow, J.D.; Klouda, L.; Mikos, A.G. Injectable matrices and scaffolds for drug delivery in tissue engineering. *Adv. Drug Deliv. Rev.* **2007**, *59*, 263–273. [CrossRef] [PubMed]

42. Pan, Z.; Ding, J. Poly(lactide-co-glycolide) porous scaffolds for tissue engineering and regenerative medicine. *Interface Focus* **2012**, *2*, 366–377. [CrossRef] [PubMed]

43. Bartus, C.; William Hanke, C.; Daro-Kaftan, E. A decade of experience with injectable poly-l-lactic acid: A focus on safety. *Off. Publ. Am. Soc. Dermatol. Surg.* **2013**, *39*, 698–705. [CrossRef] [PubMed]

44. Panyam, J.; Labhasetwar, V. Biodegradable nanoparticles for drug and gene delivery to cells and tissue. *Adv. Drug Deliv. Rev.* **2003**, *55*, 329–347. [CrossRef]

45. Bakhru, S.H.; Furtado, S.; Morello, A.P.; Mathiowitz, E. Oral delivery of proteins by biodegradable nanoparticles. *Adv. Drug Deliv. Rev.* **2013**, *65*, 811–821. [CrossRef]

46. Vasir, J.K.; Labhasetwar, V. Biodegradable nanoparticles for cytosolic delivery of therapeutics. *Adv. Drug Deliv.Rev.* **2007**, *59*, 718–728. [CrossRef]

47. Acharya, S.; Sahoo, S.K. Plga nanoparticles containing various anticancer agents and tumour delivery by epr effect. *Adv. Drug Deliv.Rev.* **2011**, *63*, 170–183. [CrossRef]

48. Li, H.; Chang, J.; Cao, A.; Wang, J. In vitro evaluation of biodegradable poly(butylene succinate) as a novel biomaterial. *Macromol. Biosci.* **2005**, *5*, 433–440. [CrossRef] [PubMed]

49. Yang, J.; Tian, W.; Li, Q.; Li, Y.; Cao, A. Novel biodegradable aliphatic poly(butylene succinate-co-cyclic carbonate)s bearing functionalizable carbonate building blocks: Ii. Enzymatic biodegradation and in vitro biocompatibility assay. *Biomacromolecules* **2004**, *5*, 2258–2268. [CrossRef] [PubMed]

50. Bechthold, I.; Bretz, K.; Kabasci, S.; Kopitzky, R.; Springer, A. Succinic acid: A new platform chemical for biobased polymers from renewable resources. *Chem. Eng. Technol.* **2008**, *31*, 647–654. [CrossRef]

51. Jäger, E.; Donato, R.K.; Perchacz, M.; Jäger, A.; Surman, F.; Höcherl, A.; Konefał, R.; Donato, K.Z.; Venturini, C.G.; Bergamo, V.Z.; et al. Biocompatible succinic acid-based polyesters for potential biomedical applications: Fungal biofilm inhibition and mesenchymal stem cell growth. *RSC Adv.* **2015**, *5*, 85756–85766. [CrossRef]

52. Jäger, A.; Jäger, E.; Giacomelli, F.C.; Nallet, F.; Steinhart, M.; Putaux, J.-L.; Konefał, R.; Spěváček, J.; Ulbrich, K.; Štěpánek, P. Structural changes on polymeric nanoparticles induced by hydrophobic drug entrapment. *Physicochem. Eng. Asp.* **2018**, *538*, 238–249. [CrossRef]

53. Jäger, A.; Jäger, E.; Syrová, Z.; Mazel, T.; Kováčik, L.; Raška, I.; Höcherl, A.; Kučka, J.; Konefal, R.; Humajova, J.; et al. Poly(ethylene oxide monomethyl ether)-block-poly(propylene succinate) nanoparticles: Synthesis and characterization, enzymatic and cellular degradation, micellar solubilization of paclitaxel, and in vitro and in vivo evaluation. *Biomacromolecules* **2018**, *19*, 2443–2458. [CrossRef]

54. Van Dijkhuizen-Radersma, R.; Roosma, J.R.; Kaim, P.; Métairie, S.; Péters, F.L.A.M.A.; de Wijn, J.; Zijlstra, P.G.; de Groot, K.; Bezemer, J.M. Biodegradable poly(ether-ester) multiblock copolymers for controlled release applications. *J. Biomed. Mater. Res.* **2003**, *67*, 1294–1304. [CrossRef] [PubMed]

55. Van Dijkhuizen-Radersma, R.; Roosma, J.R.; Sohier, J.; Péters, F.L.A.M.A.; van den Doel, M.; van Blitterswijk, C.A.; de Groot, K.; Bezemer, J.M. Biodegradable poly(ether-ester) multiblock copolymers for controlled release applications: An in vivo evaluation. *J. Biomed. Mater. Res.* **2004**, *71*, 118–127. [CrossRef]

56. Wang, L.-C.; Chen, J.-W.; Liu, H.-L.; Chen, Z.-Q.; Zhang, Y.; Wang, C.-Y.; Feng, Z.-G. Synthesis and evaluation of biodegradable segmented multiblock poly(ether ester) copolymers for biomaterial applications. *Polym. Int.* **2004**, *53*, 2145–2154. [CrossRef]

57. Lindström, A.; Albertsson, A.-C.; Hakkarainen, M. Quantitative determination of degradation products an effective means to study early stages of degradation in linear and branched poly(butylene adipate) and poly(butylene succinate). *Polym. Degrad. Stab.* **2004**, *83*, 487–493. [CrossRef]

58. Bremer, J.; Osmundsen, H. Chapter 5 fatty acid oxidation and its regulation. In *New Comprehensive Biochemistry*; Numa, S., Ed.; Elsevier: Amsterdam, The Netherlands, 1984; Volume 7, pp. 113–154.

59. Domb, A.J.; Maniar, M. Absorbable biopolymers derived from dimer fatty acids. *J. Polym. Sci. A Polym. Chem.* **1993**, *31*, 1275–1285. [CrossRef]

60. Jain, J.P.; Sokolsky, M.; Kumar, N.; Domb, A.J. Fatty acid based biodegradable polymer. *Polym. Rev.* **2008**, *48*, 156–191. [CrossRef]

61. Jäger, E.; Jäger, A.; Chytil, P.; Etrych, T.; Říhová, B.; Giacomelli, F.C.; Štěpánek, P.; Ulbrich, K. Combination chemotherapy using core-shell nanoparticles through the self-assembly of hpma-based copolymers and degradable polyester. *J. Controll. Release* **2013**, *165*, 153–161. [CrossRef] [PubMed]

62. Burkersroda, F.v.; Schedl, L.; Göpferich, A. Why degradable polymers undergo surface erosion or bulk erosion. *Biomaterials* **2002**, *23*, 4221–4231. [CrossRef]

63. Ge, H.; Hu, Y.; Yang, S.; Jiang, X.; Yang, C. Preparation, characterization, and drug release behaviors of drug-loaded ε-caprolactone/l-lactide copolymer nanoparticles. *J. Appl. Polym. Sci.* **2000**, *75*, 874–882. [CrossRef]

64. Liu, Q.; Cai, C.; Dong, C.-M. Poly(l-lactide)-b-poly(ethylene oxide) copolymers with different arms: Hydrophilicity, biodegradable nanoparticles, in vitro degradation, and drug-release behavior. *J. Biomed. Mater. Res.* **2009**, *88*, 990–999. [CrossRef] [PubMed]

65. Karavelidis, V.; Karavas, E.; Giliopoulos, D.; Papadimitriou, S.; Bikiaris, D. Evaluating the effects of crystallinity in new biocompatible polyester nanocarriers on drug release behavior. *Int. J. Nanomed.* **2009**, *6*, 3021–3032.

66. Kang Moo, H.; Hyun Su, M.; Sang Cheon, L.; Hong Jae, L.; Sungwon, K.; Kinam, P. A new hydrotropic block copolymer micelle system for aqueous solubilization of paclitaxel. *J. Controll. Release* **2008**, *126*, 122–129. [CrossRef]

67. Mahmud, A.; Patel, S.; Molavi, O.; Choi, P.; Samuel, J.; Lavasanifar, A. Self-associating poly(ethylene oxide)-b-poly(α-cholesteryl carboxylate-ε-caprolactone) block copolymer for the solubilization of stat-3 inhibitor cucurbitacin i. *Biomacromolecules* **2009**, *10*, 471–478. [CrossRef]

68. Patel, S.K.; Lavasanifar, A.; Choi, P. Roles of nonpolar and polar intermolecular interactions in the improvement of the drug loading capacity of peo-b-pcl with increasing pcl content for two hydrophobic cucurbitacin drugs. *Biomacromolecules* **2009**, *10*, 2584–2591. [CrossRef]

69. Washington, K.E.; Kularatne, R.N.; Karmegam, V.; Biewer, M.C.; Stefan, M.C. Recent advances in aliphatic polyesters for drug delivery applications. *WIREs Nanomed. Nanobiotechnol.* **2017**, *9*, e1446. [CrossRef] [PubMed]

70. Ulbrich, K.; Šubr, V.R. Polymeric anticancer drugs with ph-controlled activation. *Adv. Drug Deliv. Rev.* **2004**, *56*, 1023–1050. [CrossRef] [PubMed]

71. Qiao, Z.-Y.; Qiao, S.-L.; Fan, G.; Fan, Y.-S.; Chen, Y.; Wang, H. One-pot synthesis of ph-sensitive poly(rgd-co-β-amino ester)s for targeted intracellular drug delivery. *Polym. Chem.* **2014**, *5*, 844–853. [CrossRef]

72. Yi, Y.; Lin, G.; Chen, S.; Liu, J.; Zhang, H.; Mi, P. Polyester micelles for drug delivery and cancer theranostics: Current achievements, progresses and future perspectives. *Mater. Sci. Eng. C* **2018**, *83*, 218–232. [CrossRef] [PubMed]

73. Xiong, X.-B.; Mahmud, A.; Uludağ, H.; Lavasanifar, A. Multifunctional polymeric micelles for enhanced intracellular delivery of doxorubicin to metastatic cancer cells. *Pharm. Res.* **2008**, *25*, 2555–2566. [CrossRef] [PubMed]

74. Xiong, X.-B.; Ma, Z.; Lai, R.; Lavasanifar, A. The therapeutic response to multifunctional polymeric nano-conjugates in the targeted cellular and subcellular delivery of doxorubicin. *Biomaterials* **2010**, *31*, 757–768. [CrossRef] [PubMed]

75. Sawant, R.M.; Hurley, J.P.; Salmaso, S.; Kale, A.; Tolcheva, E.; Levchenko, T.S.; Torchilin, V.P. "Smart" drug delivery systems: Double-targeted ph-responsive pharmaceutical nanocarriers. *Bioconj. Chem.* **2006**, *17*, 943–949. [CrossRef] [PubMed]

76. Bae, Y.; Nishiyama, N.; Fukushima, S.; Koyama, H.; Yasuhiro, M.; Kataoka, K. Preparation and biological characterization of polymeric micelle drug carriers with intracellular ph-triggered drug release property: Tumor permeability, controlled subcellular drug distribution, and enhanced In Vivo antitumor efficacy. *Bioconj. Chem.* **2005**, *16*, 122–130. [CrossRef]

77. Almutairi, A.; Guillaudeu, S.J.; Berezin, M.Y.; Achilefu, S.; Fréchet, J.M.J. Biodegradable ph-sensing dendritic nanoprobes for near-infrared fluorescence lifetime and intensity imaging. *J. Am. Chem. Soc.* **2008**, *130*, 444–445. [CrossRef]

78. Pang, Y.; Liu, J.; Su, Y.; Wu, J.; Zhu, L.; Zhu, X.; Yan, D.; Zhu, B. Design and synthesis of thermo-responsive hyperbranched poly(amine-ester)s as acid-sensitive drug carriers. *Polym. Chem.* **2011**, *2*, 1661–1670. [CrossRef]

79. Honglawan, A.; Ni, H.; Weissman, D.; Yang, S. Synthesis of random copolymer based ph-responsive nanoparticles as drug carriers for cancer therapeutics. *Polym. Chem.* **2013**, *4*, 3667–3675. [CrossRef]

80. Gillies, E.R.; Fréchet, J.M.J. Ph-responsive copolymer assemblies for controlled release of doxorubicin. *Bioconj. Chem.* **2005**, *16*, 361–368. [CrossRef] [PubMed]

81. Gillies, E.R.; Goodwin, A.P.; Fréchet, J.M.J. Acetals as ph-sensitive linkages for drug delivery. *Bioconj. Chem.* **2004**, *15*, 1254–1263. [CrossRef] [PubMed]

82. Heller, J. Controlled drug release from poly(ortho esters). *J. Controll. Release* **1985**, *446*, 51–66. [CrossRef] [PubMed]

83. Tang, R.; Palumbo, R.N.; Ji, W.; Wang, C. Poly(ortho ester amides): Acid-labile temperature-responsive copolymers for potential biomedical applications. *Biomacromolecules* **2009**, *10*, 722–727. [CrossRef] [PubMed]

84. Srinophakun, T.; Boonmee, J. Preliminary study of conformation and drug release mechanism of doxorubicin-conjugated glycol chitosan, via cis-aconityl linkage, by molecular modeling. *Int. J. Mol. Sci.* **2011**, *12*, 1672. [CrossRef] [PubMed]

85. Yoo, H.S.; Lee, E.A.; Park, T.G. Doxorubicin-conjugated biodegradable polymeric micelles having acid-cleavable linkages. *J. Controll. Release* **2002**, *82*, 17–27. [CrossRef]

86. Heffernan, M.J.; Murthy, N. Polyketal nanoparticles: A new ph-sensitive biodegradable drug delivery vehicle. *Bioconj. Chem.* **2005**, *16*, 1340–1342. [CrossRef] [PubMed]

87. Heller, J.; Barr, J. Poly(ortho esters)from concept to reality. *Biomacromolecules* **2004**, *5*, 1625–1632. [CrossRef]

88. Van Den Mooter, G.; Maris, B.; Samyn, C.; Augustijns, P.; Kinget, R. Use of azo polymers for colon-specific drug delivery. *J. Pharm. Sci.* **1997**, *86*, 1321–1327. [CrossRef]

89. Mutlu, H.; Geiselhart, C.M.; Barner-Kowollik, C. Untapped potential for debonding on demand: The wonderful world of azo-compounds. *Mater. Horiz.* **2018**, *5*, 162–183. [CrossRef]

90. Coelho, P.J.; Castro, M.C.R.; Fernandes, S.S.M.; Fonseca, A.M.C.; Raposo, M.M.M. Enhancement of the photochromic switching speed of bithiophene azo dyes. *Tetrahedron Lett.* **2012**, *53*, 4502–4506. [CrossRef]

91. Brown, J.P. Reduction of polymeric azo and nitro dyes by intestinal bacteria. *Appl. Environ. Microbiol.* **1981**, *41*, 1283–1286. [PubMed]

92. Eom, T.; Yoo, W.; Kim, S.; Khan, A. Biologically activatable azobenzene polymers targeted at drug delivery and imaging applications. *Biomaterials* **2018**, *185*, 333–347. [CrossRef] [PubMed]

93. Samyn, C.; Kalala, W.; Van den Mooter, G.; Kinget, R. Synthesis and in vitro biodegradation of poly(ether-ester) azo polymers designed for colon targeting. *Int. J. Pharm.* **1995**, *121*, 211–216. [CrossRef]

94. Lu, L.; Chen, G.; Qiu, Y.; Li, M.; Liu, D.; Hu, D.; Gu, X.; Xiao, Z.J.S.B. Nanoparticle-based oral delivery systems for colon targeting: Principles and design strategies. *Sci. Bull.* **2016**, *61*, 670–681. [CrossRef]

95. Rajpurohit, H.; Sharma, P.; Sharma, S.; Bhandari, A. Polymers for colon targeted drug delivery. *Indian J. Pharm. Sci.* **2010**, *72*, 689–696. [CrossRef]

96. Balendiran, G.K.; Dabur, R.; Fraser, D. The role of glutathione in cancer. *Cell Biochem. Funct.* **2004**, *22*, 343–352. [CrossRef]

97. Quinn, J.F.; Whittaker, M.R.; Davis, T.P. Glutathione responsive polymers and their application in drug delivery systems. *Polym. Chem.* **2017**, *8*, 97–126. [CrossRef]

98. Ling, X.; Tu, J.; Wang, J.; Shajii, A.; Kong, N.; Feng, C.; Zhang, Y.; Yu, M.; Xie, T.; Bharwani, Z.; et al. Glutathione-responsive prodrug nanoparticles for effective drug delivery and cancer therapy. *ACS Nano* **2019**, *13*, 357–370. [CrossRef]

99. Song, N.; Liu, W.; Tu, Q.; Liu, R.; Zhang, Y.; Wang, J. Preparation and in vitro properties of redox-responsive polymeric nanoparticles for paclitaxel delivery. *Colloids Surfaces B Biointerfaces* **2011**, *87*, 454–463. [CrossRef] [PubMed]

100. Yang, Q.; Tan, L.; He, C.; Liu, B.; Xu, Y.; Zhu, Z.; Shao, Z.; Gong, B.; Shen, Y.-M. Redox-responsive micelles self-assembled from dynamic covalent block copolymers for intracellular drug delivery. *Acta Biomat.* **2015**, *17*, 193–200. [CrossRef] [PubMed]

101. Son, S.; Namgung, R.; Kim, J.; Singha, K.; Kim, W.J. Bioreducible polymers for gene silencing and delivery. *Acc. Chem. Res.* **2012**, *45*, 1100–1112. [CrossRef] [PubMed]

102. Bauhuber, S.; Hozsa, C.; Breunig, M.; Göpferich, A. Delivery of nucleic acids via disulfide-based carrier systems. *Adv. Mater.* **2009**, *21*, 3286–3306. [CrossRef] [PubMed]

103. Liu, H.; Wang, H.; Yang, W.; Cheng, Y. Disulfide cross-linked low generation dendrimers with high gene transfection efficacy, low cytotoxicity, and low cost. *J. Am. Chem. Soc.* **2012**, *134*, 17680–17687. [CrossRef] [PubMed]

104. Song, L.; Ding, A.-X.; Zhang, K.-X.; Gong, B.; Lu, Z.-L.; He, L. Degradable polyesters via ring-opening polymerization of functional valerolactones for efficient gene delivery. *Org. Biomol. Chem.* **2017**, *15*, 6567–6574. [CrossRef] [PubMed]

105. Sies, H. Glutathione and its role in cellular functions. *Free Radic. Biol. Med.* **1999**, *27*, 916–921. [CrossRef]

106. Zhu, W.; Wang, Y.; Cai, X.; Zha, G.; Luo, Q.; Sun, R.; Li, X.; Shen, Z. Reduction-triggered release of paclitaxel from in situ formed biodegradable core-cross-linked micelles. *J. Mater. Chem. B* **2015**, *3*, 3024–3031. [CrossRef]

107. Yameen, B.; Vilos, C.; Choi, W.I.; Whyte, A.; Huang, J.; Pollit, L.; Farokhzad, O.C. Drug delivery nanocarriers from a fully degradable peg-conjugated polyester with a reduction-responsive backbone. *Chem. Eur. J.* **2015**, *21*, 11325–11329. [CrossRef]

108. Vo, C.D.; Kilcher, G.; Tirelli, N. Polymers and sulfur: What are organic polysulfides good for? Preparative strategies and biological applications. *Macromol. Rapid Commun.* **2009**, *30*, 299–315. [CrossRef]

109. Song, C.-C.; Du, F.-S.; Li, Z.-C. Oxidation-responsive polymers for biomedical applications. *J. Mater. Chem. B* **2014**, *2*, 3413–3426. [CrossRef]

110. Napoli, A.; Valentini, M.; Tirelli, N.; Müller, M.; Hubbell, J.A. Oxidation-responsive polymeric vesicles. *Nat. Mater.* **2004**, *3*, 183–189. [CrossRef] [PubMed]

111. Rehor, A.; Tirelli, N.; Hubbell, J.A. A new living emulsion polymerization mechanism: Episulfide anionic polymerization. *Macromolecules* **2002**, *35*, 8688–8693. [CrossRef]

112. Allen, B.L.; Johnson, J.D.; Walker, J.P. Encapsulation and enzyme-mediated release of molecular cargo in polysulfide nanoparticles. *ACS Nano* **2011**, *5*, 5263–5272. [CrossRef] [PubMed]

113. Hirosue, S.; Kourtis, I.C.; van der Vlies, A.J.; Hubbell, J.A.; Swartz, M.A. Antigen delivery to dendritic cells by poly(propylene sulfide) nanoparticles with disulfide conjugated peptides: Cross-presentation and t cell activation. *Vaccine* **2010**, *28*, 7897–7906. [CrossRef] [PubMed]

114. Gupta, M.K.; Meyer, T.A.; Nelson, C.E.; Duvall, C.L. Poly(ps-b-dma) micelles for reactive oxygen species triggered drug release. *J. Controll. Release* **2012**, *162*, 591–598. [CrossRef]

115. Poole, K.M.; Nelson, C.E.; Joshi, R.V.; Martin, J.R.; Gupta, M.K.; Haws, S.C.; Kavanaugh, T.E.; Skala, M.C.; Duvall, C.L. Ros-responsive microspheres for on demand antioxidant therapy in a model of diabetic peripheral arterial disease. *Biomaterials* **2015**, *41*, 166–175. [CrossRef]

116. Zhang, J.; Tokatlian, T.; Zhong, J.; Ng, Q.K.T.; Patterson, M.; Lowry, W.E.; Carmichael, S.T.; Segura, T. Physically associated synthetic hydrogels with long-term covalent stabilization for cell culture and stem cell transplantation. *Adv. Mater.* **2011**, *23*, 5098–5103. [CrossRef]

117. Kim, K.; Lee, C.-S.; Na, K. Light-controlled reactive oxygen species (ros)-producible polymeric micelles with simultaneous drug-release triggering and endo/lysosomal escape. *Chem. Commun.* **2016**, *52*, 2839–2842. [CrossRef]

118. Caucheteux, S.M.; Mitchell, J.P.; Ivory, M.O.; Hirosue, S.; Hakobyan, S.; Dolton, G.; Ladell, K.; Miners, K.; Price, D.A.; Kan-Mitchell, J.; et al. Polypropylene sulfide nanoparticle p24 vaccine promotes dendritic cell-mediated specific immune responses against hiv-1. *J. Investig. Dermatol.* **2016**, *136*, 1172–1181. [CrossRef]

119. Cao, W.; Wang, L.; Xu, H. Selenium/tellurium containing polymer materials in nanobiotechnology. *Nano Today* **2015**, *10*, 717–736. [CrossRef]

120. Ma, N.; Li, Y.; Xu, H.; Wang, Z.; Zhang, X. Dual redox responsive assemblies formed from diselenide block copolymers. *J. Am. Chem. Soc.* **2010**, *132*, 442–443. [CrossRef] [PubMed]

121. Han, P.; Li, S.; Cao, W.; Li, Y.; Sun, Z.; Wang, Z.; Xu, H. Red light responsive diselenide-containing block copolymer micelles. *J. Mater. Chem. B* **2013**, *1*, 740–743. [CrossRef]

122. Yu, L.; Zhang, M.; Du, F.-S.; Li, Z.-C. Ros-responsive poly(ε-caprolactone) with pendent thioether and selenide motifs. *Polym. Chem.* **2018**, *9*, 3762–3773. [CrossRef]

123. Wang, C.; An, X.; Pang, M.; Zhang, Z.; Zhu, X.; Zhu, J.; Du Prez, F.E.; Pan, X. Dynamic diselenide-containing polyesters from alcoholysis/oxidation of γ-butyroselenolactone. *Polym. Chem.* **2018**, *9*, 4044–4051. [CrossRef]

124. Broaders, K.E.; Grandhe, S.; Fréchet, J.M.J. A biocompatible oxidation-triggered carrier polymer with potential in therapeutics. *J. Am. Chem. Soc.* **2011**, *133*, 756–758. [CrossRef] [PubMed]

125. De Gracia Lux, C.; Joshi-Barr, S.; Nguyen, T.; Mahmoud, E.; Schopf, E.; Fomina, N.; Almutairi, A. Biocompatible polymeric nanoparticles degrade and release cargo in response to biologically relevant levels of hydrogen peroxide. *J. Am. Chem. Soc.* **2012**, *134*, 15758–15764. [CrossRef]

126. Jäger, E.; Höcherl, A.; Janoušková, O.; Jäger, A.; Hrubý, M.; Konefał, R.; Netopilik, M.; Pánek, J.; Šlouf, M.; Ulbrich, K.; et al. Fluorescent boronate-based polymer nanoparticles with reactive oxygen species (ros)-triggered cargo release for drug-delivery applications. *Nanoscale* **2016**, *8*, 6958–6963. [CrossRef]

127. Lee, D.; Khaja, S.; Velasquez-Castano, J.C.; Dasari, M.; Sun, C.; Petros, J.; Taylor, W.R.; Murthy, N. In vivo imaging of hydrogen peroxide with chemiluminescent nanoparticles. *Nat. Mater.* **2007**, *6*, 765. [CrossRef]

128. Kim, S.; Seong, K.; Kim, O.; Kim, S.; Seo, H.; Lee, M.; Khang, G.; Lee, D. Polyoxalate nanoparticles as a biodegradable and biocompatible drug delivery vehicle. *Biomacromolecules* **2010**, *11*, 555–560. [CrossRef]

129. Lee, D.; Bae, S.; Ke, Q.; Lee, J.; Song, B.; Karumanchi, S.A.; Khang, G.; Choi, H.S.; Kang, P.M. Hydrogen peroxide-responsive copolyoxalate nanoparticles for detection and therapy of ischemia–reperfusion injury. *J. Controll. Release* **2013**, *172*, 1102–1110. [CrossRef] [PubMed]

130. Lee, D.; Bae, S.; Hong, D.; Lim, H.; Yoon, J.H.; Hwang, O.; Park, S.; Ke, Q.; Khang, G.; Kang, P.M. H_2O_2-responsive molecularly engineered polymer nanoparticles as ischemia/reperfusion-targeted nanotherapeutic agents. *Sci. Rep.* **2013**, *3*, 2233. [CrossRef] [PubMed]

131. Höcherl, A.; Jäger, E.; Jäger, A.; Hrubý, M.; Konefał, R.; Janoušková, O.; Spěváček, J.; Jiang, Y.; Schmidt, P.W.; Lodge, T.P.; et al. One-pot synthesis of reactive oxygen species (ros)-self-immolative polyoxalate prodrug nanoparticles for hormone dependent cancer therapy with minimized side effects. *Polym. Chem.* **2017**, *8*, 1999–2004. [CrossRef]

132. Dongwon, L.; Madhuri, D.; Venkata, E.; Niren, M.; Junhua, Y.; Robert, D. Detection of hydrogen peroxide with chemiluminescent micelles. *Int. J. Nanomed.* **2008**, *3*, 471–476.

133. Liang, X.; Duan, J.; Li, X.; Zhu, X.; Chen, Y.; Wang, X.; Sun, H.; Kong, D.; Li, C.; Yang, J. Improved vaccine-induced immune responses via a ros-triggered nanoparticle-based antigen delivery system. *Nanoscale* **2018**, *10*, 9489–9503. [CrossRef] [PubMed]

134. Chang, S.H.; Lee, H.J.; Park, S.; Kim, Y.; Jeong, B. Fast degradable polycaprolactone for drug delivery. *Biomacromolecules* **2018**, *19*, 2302–2307. [CrossRef] [PubMed]

135. Azevedo, H.S.; Santos, T.C.; Reis, R.L. 4-controlling the degradation of natural polymers for biomedical applications. In *Natural-Based Polymers for Biomedical Application*; Reis, R.L., Neves, N.M., Mano, J.F., Gomes, M.E., Marques, A.P., Azevedo, H.S., Eds.; Woodhead Publishing: Cambridge, UK, 2008; pp. 106–128.

136. Azevedo, H.S.; Reis, R.L. Understanding the enzymatic degradation of biodegradable polymers and strategies to control their degradation rate. In *Biodegradable Systems in Tissue Engineering and Regenerative Medicine*; Reis, R.L., Román, J.S., Eds.; CRC Press: Boca Raton, FL, USA, 2004; pp. 186–210.

137. Buchholz, V.; Agarwal, S.; Greiner, A. Synthesis and enzymatic degradation of soft aliphatic polyesters. *Macromol. Biosci.* **2016**, *16*, 207–213. [CrossRef]

138. Berg, J.M.; Tymoczko, J.L.; Gatto, G.J.; Stryer, L. *Biochemistry*, 5th ed.; W.H. Freeman: New York, NY, USA, 2015.

139. Trousil, J.; Filippov, S.K.; Hrubý, M.; Mazel, T.; Syrová, Z.; Cmarko, D.; Svidenská, S.; Matějková, J.; Kováčik, L.; Porsch, B.; et al. System with embedded drug release and nanoparticle degradation sensor showing efficient rifampicin delivery into macrophages. *Nanomed. Nanotechnol. Biol. Med.* **2017**, *13*, 307–315. [CrossRef]

140. Brulé, E.; Robert, C.; Thomas, C.M. Sequence-controlled ring-opening polymerization: Synthesis of new polyester structures. In *Sequence-Controlled Polymers: Synthesis, Self-Assembly, and Properties*; American Chemical Society: Washington, DC, USA, 2014; Volume 1170, pp. 349–368.

141. Rasal, R.M.; Janorkar, A.V.; Hirt, D.E. Poly(lactic acid) modifications. *Prog. Polym. Sci.* **2010**, *35*, 338–356. [CrossRef]

142. Trousil, J.; Syrová, Z.; Dal, N.-J.K.; Rak, D.; Konefał, R.; Pavlova, E.; Matějková, J.; Cmarko, D.; Kubíčková, P.; Pavliš, O.; et al. Rifampicin nanoformulation enhances treatment of tuberculosis in zebrafish. *Biomacromolecules* **2019**, *20*, 1798–1815. [CrossRef]

Appendix 2

Urbánek, T.; Trousil, J.; Rak, D.; Gunár, K.; Konefał, R.; Šlouf, M.; Sedlák, M.; Janoušková Šebestová, O.; Hrubý, M. γ-Butyrolactone Copolymerization with the Well-Documented Polymer Drug Carrier Poly(ethylene oxide)-block-poly(ε-caprolactone) to Fine-Tune Its Biorelevant Properties. *Macromolecular Bioscience* **2020**, 20 (5). IF = 4.979

γ-Butyrolactone Copolymerization with the Well-Documented Polymer Drug Carrier Poly(ethylene oxide)-*block*-poly(ε-caprolactone) to Fine-Tune Its Biorelevant Properties

Tomáš Urbánek, Jiří Trousil, Dmytro Rak, Kristýna Gunár, Rafał Konefał, Miroslav Šlouf, Marián Sedlák, Olga Šebestová Janoušková, and Martin Hrubý*

Polymeric drug carriers exhibit excellent properties that advance drug delivery systems. In particular, carriers based on poly(ethylene oxide)-*block*-poly(ε-caprolactone) are very useful in pharmacokinetics. In addition to their proven biocompatibility, there are several requirements for the efficacy of the polymeric drug carriers after internalization, e.g., nanoparticle behavior, cellular uptake, the rate of degradation, and cellular localization. The introduction of γ-butyrolactone units into the hydrophobic block enables the tuning of the abovementioned properties over a wide range. In this study, a relatively high content of γ-butyrolactone units with a reasonable yield of ≈60% is achieved by anionic ring-opening copolymerization using 1,5,7-triazabicyclo[4.4.0]dec-5-ene as a very efficient catalyst in the nonpolar environment of toluene with an incorporated γ-butyrolactone content of ≈30%. The content of γ-butyrolactone units can be easily modulated according to the feed ratio of the monomers. This method enables control over the rate of degradation so that when the content of γ-butyrolactone increases, the rate of degradation increases. These findings broaden the application possibilities of polyester-polyether-based nanoparticles for biomedical applications, such as drug delivery systems.

1. Introduction

Amphiphilic polymeric nanoparticles (NPs) are nanomaterials generated by the self-association of polymeric amphiphiles above a critical aggregation concentration, and their use of intervention is based on their physicochemical properties and architecture; the array of hydrophilic and hydrophobic domains can vary.[1–3] A class of important biodegradable and/or biocompatible polymers, aliphatic polyesters, have been widely studied due to their large-scale accessibility by the ring-opening polymerization (ROP) of cyclic esters or lactones.[4] In contrast to the commonly used lactones or esters for the synthesis of aliphatic copolyesters, γ-butyrolactone (γBL) is a very promising monomer, as introduction of γBL into other aliphatic polyesters might modify the degradation rate to meet the desired application demand.[5–8] Notably, the biocompatibility of poly(γ-butyrolactone) (P4HB) has been shown to be better than that of poly(glycolic acid) and poly(lactide-*co*-glycolide), which are copolymers that have been widely studied in terms of drug delivery in vivo.[7,9] Given this, γBL has been suggested to be a suitable comonomer for drug delivery system tuning.

Although γBL seems to be the perfect choice as a monomer for polymers in medical applications, its thermodynamic parameters do not allow for it to undergo ROP to a sufficient extent.[10,11] In the 1930s, γBL was proclaimed as a nonpolymerizable substance[12] and the corresponding research slowed. Polymerization conditions have been considered the key factors that determine the polymerizability of a substance, and in the 1960s, γBL was successfully converted into low-molecular-weight polyester (1200–3500 g mol⁻¹) under extreme conditions (2 GPa, 165 °C);[13] the high-pressure homopolymerization of γBL has been reported several times, and the molecular weight was increased by acid catalysis.[14] Attempts were made to prepare high-molecular-weight P4HB under less extreme conditions, and in 2016, these attempts resulted in success when a lanthanum

T. Urbánek, J. Trousil, Dr. K. Gunár, Dr. R. Konefał, M. Šlouf,
Dr. O. Šebestová Janoušková, Dr. M. Hrubý
Institute of Macromolecular Chemistry
Czech Academy of Sciences
Heyrovského náměstí 2, 162 00 Prague 6, Czechia
E-mail: mhruby@centrum.cz
J. Trousil
Department of Analytical Chemistry
Charles University
Faculty of Science
Hlavova 8, 128 43 Prague 2, Czechia
Dr. D. Rak, Dr. M. Sedlák
Institute of Experimental Physics
Slovak Academy of Sciences
Watsonova 47, 040 01 Košice, Slovakia

ADVANCED
SCIENCE NEWS
www.advancedsciencenews.com

Macromolecular
Bioscience
www.mbs-journal.de

complex was employed as a catalyst.[15] However, currently, as biologic and electronic applications are at the forefront of interest, the purity of polymers is taken into account, and thus, nonmetallic catalysts are preferred.[16–21] A viable strategy for the incorporation of γBL into a polymeric chain is its copolymerization with thermodynamically favorable monomers.[8,22,23]

Amphiphilic diblock copolymers composed of hydrophobic biodegradable polyester blocks and hydrophilic polymer blocks are very suitable for the construction of micellar/nanoparticle drug delivery systems with core-corona structures because hydrophobic drugs can be encapsulated into micelle cores, while the hydrophobic portion can be degraded into low-molecular-weight fragments after drug release, allowing for elimination from the system of the organism while the hydrophilic corona-forming block protects the core from unwanted interactions in the organism. Among such copolymers, methoxy poly(ethylene oxide)-*block*-poly(ε-caprolactone) is very popular for the construction of drug delivery systems. However, the tuning of its properties is limited by the chemical properties of the polymer block from which it is composed.

In this work, we report the synthesis and characterization of an amphiphilic block copolymer composed of mPEO and poly(ε-caprolactone-*co*-γ-butyrolactone) (PCL-*co*-P4HB) possessing a favorable amount of P4HB. This copolymer undergoes self-association in an aqueous medium and forms spherical amphiphilic assemblies, as determined by cryo-transmission electron microscopy (cryo-TEM). This intervention was found to be enzymatically degradable by two different approaches (dynamic light scattering, DLS, and flow cytometry) and noncytotoxic. In addition, the low-molecular-weight hydrolytic products of the polyester block (6-hydroxyhexanoic acid and 4-hydroxybutyric acid) are fully metabolizable into carbon dioxide and water. The novel copolymerization of P4HB into the hydrophobic polyester block of mPEO-PCL block copolymers of this article was found to be an excellent tool for the adjustment of the properties critical for its use in drug delivery systems (NP behavior, cell uptake, biodegradation rate, and intracellular localization) over a very wide range, strongly increasing the variety of possible uses.

2. Experimental Section

2.1. Materials

γBL (≥99%) and ε-caprolactone (εCL, 97%) were purchased from Sigma-Aldrich Ltd. (Prague, Czechia), dried over calcium hydride for 24 h, subsequently distilled under reduced pressure, and stored under an inert atmosphere prior to use.

Benzyl alcohol (BA, ≥99%, Sigma-Aldrich Ltd.) was dried over calcium oxide for 24 h and subsequently distilled under reduced pressure twice and stored under an inert atmosphere prior to use. Poly(ethylene oxide) monomethyl ether, 2 and 5 kDa (mPEO$_{45}$ and mPEO$_{114}$, Sigma-Aldrich Ltd.), were azeotropically dried with toluene prior to use.

3,5-Bis(trifluoromethyl)phenyl isothiocyanate (98%), 1-(4,5-dimethylthiazol-2-yl)-3,5-diphenylformazan (MTT, BioReagent), cyclohexylamine (≥99.9%), 1,8-diazabicyclo[5.4.0]undec-7-ene (DBU), diphenyl phosphate (DPP), hydrochloric acid (in diethyl

ether, 2 M), lipase from *Pseudomonas* sp. (type XIII) (Sigma-Aldrich Ltd.), paraformaldehyde, 1,5,7-triazabicyclo[4.4.0]dec-5-ene (TBD, 98%), 7-(diethylamino)coumarin-3-carbonyl azide (DACCA), and γ-hydroxybutyric acid sodium salt were purchased from Sigma-Aldrich Ltd. and used as received.

7-Aminoactinomycin D (7AAD), amphotericin B (250 µg mL^{-1}), CellMask Deep Red, Dulbecco's modified Eagle medium (DMEM, high glucose, GlutaMAX), fetal bovine serum (FBS, heat-inactivated), LysoTracker Deep Red, penicillin-streptomycin solution (10 000 U mL^{-1}), and Triton X-100 solution (1%) were purchased from Life Technologies Ltd. (Prague, Czechia).

2.2. Synthesis of *N*-(3,5-bistrifluoromethyl)phenyl-*N'*-cyclohexylthiourea (TU)

Cyclohexylamine (210 µL, 1.84 mmol) was added to 10 mL of dry dichloromethane (DCM) under an argon atmosphere. This solution was cooled in an ice bath and 3,5-bis(trifluoromethyl) phenyl isothiocyanate (337 µL, 1.85 mmol) was added.[24] The reaction was maintained overnight (16 h) at room temperature. The product precipitated from the solution, the solvent was evaporated under reduced pressure and the product was purified by recrystallization from petroleum ether with a yield of 91%. The product was further used as a cocatalyst of DBU for the ROP of γBL with εCL.

2.3. Synthesis of Poly(ε-caprolactone-*co*-γ-butyrolactone) (PCL-*co*-P4HB)

Polymerization reactions (**Figure 1**A) were carried out in dry vessels under an argon atmosphere for 24 h. The desired amounts of initiator (BA), catalyst (HCl/Et$_2$O, DPP, TBD or DBU/TU), and solvent were added into the vessels equipped with magnetic stirring bars. The solutions were stirred while the monomers (εCL and γBL) were added. The feed ratios are listed in the Tables S1 and S2 in the Supporting Information. The products were washed with ice-cold Et$_2$O.
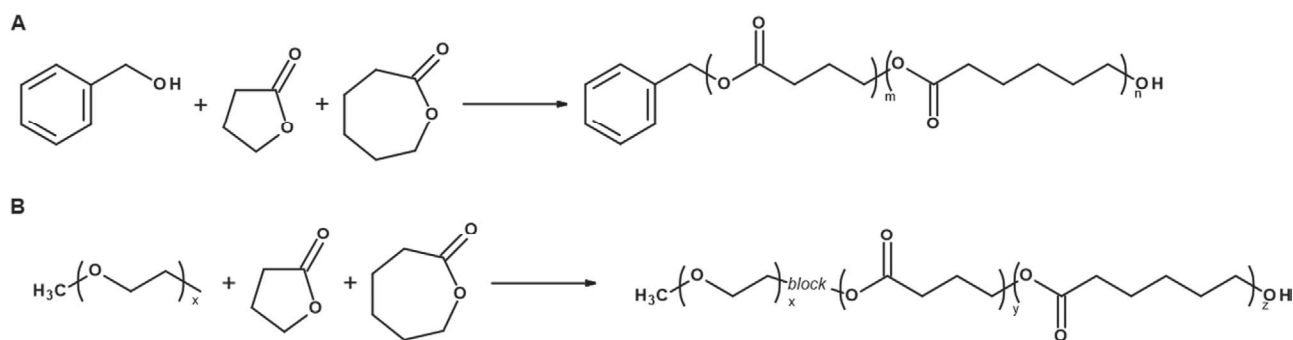
2.4. Synthesis of Poly[ethylene oxide-*block*-(ε-caprolactone-*co*-γ-butyrolactone)] [mPEO-*b*-(PCL-*co*-P4HB)]

Polymerization reactions (Figure 1B) were carried out in the same manner as the polymerization of PCL-*co*-P4HB. In this case, the poly(ethylene oxide) monomethyl ethers were used as the macroinitiators and only TBD was used as the catalyst. Feed amounts are listed in Table S3 in the Supporting Information.

2.5. Fluorescent Labeling of mPEO-*b*-(PCL-*co*-P4HB)

Chosen samples of the prepared copolymers were labeled with DACCA for biological analysis, synthesis scheme shown in Figure S12 in the Supporting Information. Each sample of 80 mg of mPEO-*b*-(PCL-*co*-P4HB) was dissolved in 10 mL of toluene, and 2 molar equivalents of DACCA were added to this

**ADVANCED
SCIENCE NEWS**
www.advancedsciencenews.com

**Macromolecular
Bioscience**
www.mbs-journal.de

A

B

Figure 1. Synthesis scheme of A) copolymer PCL-*co*-P4HB and B) block copolymer mPEO-*b*-(PCL-*co*-P4HB).

solution. The reactions were maintained at 80 °C under an argon atmosphere for 24 h.[25] The products were purified by dialysis and freeze-dried. The UV–vis spectra were measured with a UV–vis spectrophotometer (Evolution 220 Spectrometer, Thermo Scientific, USA). Fluorescence spectra of the samples were recorded (90° angle geometry, 1 × 1 cm quartz cell) with an Aminco Bowman Series 2 spectrofluorometer (Aminco, Lake Forest, CA, USA) at an excitation wavelength of 420 nm and are shown in Figure S13 in the Supporting Information.

2.6. Preparation of Nanoformulations

Nanoparticles were prepared by the nanoprecipitation method. Samples of mPEO-*b*-(PCL-*co*-P4HB) (10 mg) were diluted in acetone (1 mL), and subsequently, an aqueous phase [distilled water or phosphate-buffered saline (PBS)] (10 mL) was rapidly added while stirring at 200 rpm. The excess acetone was evaporated under reduced pressure. The final concentrations of the samples were 1 mg mL^{-1}. Nanoformulations were always prepared fresh for each characterization.

2.7. Characterization of PCL-*co*-P4HB and mPEO-*b*-(PCL-*co*-P4HB)

Proton nuclear magnetic resonance (^{1}H NMR), size-exclusion chromatography (SEC), and Fourier transform infrared spectroscopy (FTIR) were used for fundamental characterization of the synthetized copolymer structures.

A Bruker AVANCE DPX 300 (and/or AVANCE III 600 MHz) spectrometer (Bruker Daltonik GmbH, Bremen, Germany) operating at 300.1 or 600.2 MHz was utilized for chemical structure determination. All samples were dissolved in deuterated chloroform at 25 °C. The chemical shifts were relative to tetramethylsilane (TMS) using hexamethyldisiloxane (HMDSO, δ = 0.05 ppm from TMS) as the internal standard.[26] ^{13}C NMR spectrum was recorded using Bruker AVANCE III 600 MHz operating at 150.9 MHz in deuterated chloroform at 25 °C. The chemical shift was relative to TMS using HMDSO (δ = 2.00 ppm from TMS) as the internal standard.

A Perkin Elmer PARAGON 1000 PC FTIR spectrometer was utilized for chemical structure confirmation. The spectrometer had a resolution of 4 cm^{-1}, 32 accumulated scams, and strong apodization. The reflective measurements were performed

using an ATR-Specac MKII Golden Gate Single Reflection system with a diamond crystal and an angle of incidence of 45°. The samples were characterized in powder form.

Physical characterization of the synthetized copolymers was determined by SEC. Namely, the mass-average molar mass M_n, the number-average molar mass M_w, and their ratio M_w/M_n provided information about the chain length distribution–dispersity, Đ. The separation was carried out using a DeltaChrom pump (Watrex Ltd., Prague, Czechia), a Midas Spark autosampler (DataApex Ltd., Prague, Czechia), and two PLgel MIXED-B-LS columns. The samples were dissolved in tetrahydrofuran (THF), which served as the mobile phase in the chromatographic system with a flow rate of 1 mL min^{-1} at 25 °C. A PL ELS-1000 evaporative light scattering detector (Polymer Laboratories, Varian Inc., Amherst, USA) was used for the detection. The evaluation of the sample chromatograms was performed using Clarity Software Version 6.0.0.295 (DataApex Ltd.) with polystyrene standard calibration.[27]

2.8. Characterization of the Nanoparticles Prepared by mPEO-*b*-(PCL-*co*-P4HB)

Different techniques were used for the characterization of the nanoparticles. DLS measurements were carried out on a ZEN3600 Nano-ZS instrument (Malvern Instruments Ltd., UK) using an angle of 173°. A He–Ne laser (4.0 mW, operating at 633 nm) was used. The hydrodynamic diameter of the particles was calculated from the diffusion coefficient using the Stokes–Einstein equation.

Static light scattering (SLS) measurements were performed on an ALV-6010 instrument (ALV GmbH, Germany) equipped with a 22 mW He–Ne laser in the angular range of 30°–150°. The data were analyzed by using a Zimm plot. The dn/dc values were measured as described below.

The additional method for characterizing the prepared nanoparticles was asymmetric-flow field-flow fractionation (AF4). The instrument setup for AF4 consisted of an Eclipse 3+ separation system (Wyatt Technology Europe, Dernbach, Germany) coupled to a 1260 Infinity isocratic pump and degasser (Agilent Technologies, Santa Clara, CA, USA), a DAWN HELEOS II MALS detector with a 120 mW gallium-arsenide laser at a wavelength of 661 nm (Wyatt Technology, Santa Barbara, CA, USA), and an RI-101 RI detector (Shodex, Munich, Germany). Prepared nanoparticles in filtered

**ADVANCED
SCIENCE NEWS**

www.advancedsciencenews.com

**Macromolecular
Bioscience**

www.mbs-journal.de

deionized water underwent measurements using a 275 mm long trapezoidal channel consisting of a 490 μm spacer and a regenerated cellulose membrane with a 5 kDa cutoff. Collected data were processed using ASTRA 6 software.

The measurements followed the established procedure in ref. [28]. As a result, the mass-average molar mass M_w and the diameter of gyration D_g were obtained.

The refractive index increment dn/dc of the solutions was measured with a BI-DNDCW differential refractometer (Brookhaven Instruments Corporation, USA). The dn/dc values were obtained using a potassium chloride calibration solution.

2.9. Morphology of the NPs

The nanoparticle morphology was observed by transmission electron microscopy. To characterize the morphology of the nanoparticles, 3 μL of sample solution was applied to a formvar-carbon electron microscopy grid. Samples were observed without staining at 100 kV using an FEI Morgagni TEM equipped with a MegaView III side-entry charge-coupled device camera. For cryo-TEM, where the hydrated samples were imaged without the perturbation generated by drying, the sample solution was applied to a carbon-covered polymer-grid supporting film (lacey-carbon grids, Electron Microscopy Sciences, Hatfield, USA) and glow discharged for 40 s with a 5 mA current. Most of the sample was removed by blotting and the grid was immediately plunged into liquid ethane at −183 °C. The sample was then transferred without rewarming into a Tecnai Sphera G20 electron microscope (FEI) using a Gatan 626 cryo-specimen holder (Gatan Inc., Pleasanton, CA, USA). Images were recorded at a 120 kV accelerating voltage using a Gatan UltraScan 1000 slow-scan charge-coupled device camera (achieving a final pixel size from 2 to 0.7 nm) in low-dose mode.

2.10. Enzymatic Degradation of NPs

The ^{1}H NMR and SEC measurements were used to determine the enzymatic degradation of the prepared nanoparticles and the procedure is described in ref. [28]. The degradation was studied in the presence of lipase from *Pseudomonas* sp. The appropriate amount of lipase (aqueous solution in PBS, 4 U mL^{-1}) was added to the nanoformulation (1 mg mL^{-1} in PBS) to initiate the degradation process, giving final concentrations of the copolymer and lipase of 0.98 mg mL^{-1} and 0.06 U mL^{-1}, respectively. The degradation was performed at 37 °C inside an NMR cuvette. In case of SEC measurements, the purification of the organic content was needed to be done after the degradation period. The PBS solution of the sample incubated with the lipase was poured into excess of cold diethyl ether, so the organic content precipitated. The precipitate was separated by centrifugation at 7000 rpm and 0 °C and dried. This material was dissolved in mobile phase of SEC and the analysis was performed.

2.11. Critical Aggregation Concentration (CAC) Determination

The NP formulations of the synthesized copolymers were prepared by the protocol described above. Series of concentrations

reaching 10^{-6} mg mL^{-1} were obtained by serial dilution in PBS. A solution of Nile red in ethanol was added to each sample to obtain a final concentration of 10^{-6} mol L^{-1}. A Synergy H1 Hybrid Reader instrument (BioTek, Winooski, USA) was utilized to record the fluorescence of the samples. The excitation wavelength was 550 nm and the emission intensity was measured at 650 nm. The CACs were determined as the intersection points of the lines from two different parts of the graph of fluorescence intensity versus the negative logarithm of the concentrations, as seen in Figure S8 in the Supporting Information.[28]

2.12. Hemolysis assay

The determination of blood compatibility with the prepared NPs was carried out following the procedure in ref. [28]. Fresh human blood was collected for the analysis into heparin-coated vacutainers (Becton Dickinson Czechia Ltd., Prague, Czechia). Red blood cells (RBCs) were obtained by centrifugation of the blood at 3000 rpm for 10 min. The plasma was removed and RBCs were washed with PBS. The final concentration of RBCs in PBS for the hemolysis measurements was at a full blood dilution of 1:49.

To 0.3 mL of diluted RBCs, 1.2 mL of the appropriately diluted nanoformulation (in PBS) was added. With this procedure, several dilutions of NPs were prepared (100, 200, 400, and 800 μg mL^{-1}). Triton X-100 (1% in PBS) and PBS served as positive and negative controls, respectively.

After incubation at 37 °C for 8 h, the samples were centrifuged (3000 rpm, 10 min). Subsequently, the supernatants were collected and subjected to absorbance measurement at 541 nm on a Synergy H1 Hybrid Reader instrument (BioTek, Winooski, Vermont, USA). The percent hemolysis of RBCs in each sample was calculated by the following Equation (1)

$$\text{Hemolysis} = \frac{\text{sample absorbance} - \text{negative control}}{\text{positive control} - \text{negative control}} \times 100 \qquad (1)$$

The results of the hemolysis assays were expressed as a percentage of the positive control (1% Triton X-100 in PBS), which was considered 100%. Hemoglobin release up to 2% was classified as nonhemolytic, according to the ASTM F756-08 standard.[29] The results of this assay are expressed as mean values of triplicate analysis.

2.13. Cell Culture

The murine monocyte-macrophage (Mϕ) cell line J774A.1[30] was purchased from Sigma-Aldrich Ltd. The cells were maintained in DMEM supplemented with FBS (10%), penicillin (100 U mL^{-1}), streptomycin (100 μg mL^{-1}), and amphotericin B (2.5 μg mL^{-1}) in a humidified atmosphere containing 5% CO$_2$ at 37 °C.

2.14. Cytotoxicity Study

Cytotoxicity was evaluated using the MTT assay. For this purpose, J774A.1 Mϕs were seeded in 96-well plates at a density of 5000 cells per well. The cells were then incubated overnight at 37 °C and 5%

**ADVANCED
SCIENCE NEWS**
www.advancedsciencenews.com

**Macromolecular
Bioscience**
www.mbs-journal.de

CO_2 with subsequent replacement of the medium with 100 µL of fresh culture medium containing the tested formulations. After 24 h of incubation, the medium was replaced with 100 µL of MTT solution (0.5 mg mL^{-1} in PBS), and the plates were incubated for 2–4 h prior to aspiration of the medium and dimethyl sulfoxide addition (100 µL). After 15 min of blue formazan solubilization (37 °C), a Synergy H1 Hybrid Reader instrument (Biotek, Winooski, USA) was used to assess cell viability by spectrophotometry at 570 nm. The results of the MTT assay were expressed as a percent of the control (cells in control medium), which was considered 100 %. A reduction in cell viability by more than 30% was considered a cytotoxic effect according to the ISO 10993-5.[31] The tests were performed in at least three separate experiments.

2.15. Microscopic Investigation of Cellular Uptake

Confocal laser scanning microscopy (CLSM) was used to study cellular uptake and lysosome-nanoparticle colocalization. For the uptake study, J774A.1 cells were seeded at the bottom of ibidi µ-dishes (ibidi GmbH, Planegg/Martinsried, Germany) and left to adhere overnight. Subsequently, the medium was replaced with fresh medium (full DMEM) containing DACCA-labeled NPs (2.8 nmol mL^{-1}). After 40 min of incubation, the cells were washed with prewarmed PBS (37 °C) three times, stained with CellMask Deep Red according to the manufacturer's protocol for 10 min, washed with warm PBS, fixed using a paraformaldehyde solution (4% in PBS), and kept under PBS until subsequent analysis. Cells were visualized on an Olympus FV 10 confocal laser scanning microscope (Olympus Czech Group Ltd., Prague, Czech Republic) using a 60 × oil objective. Signal detection was observed in channels 1 (DACCA, exc. 405 nm, em. 425–475 nm) and 2 (CellMask Deep Red, exc. 650 nm, em. 655–750 nm).

Similarly, the lysosome-nanoparticle colocalization study was carried out using overnight-adhered macrophages (Mφs). The medium was replaced with fresh DMEM containing DACCA-labeled NPs (2.8 nmol mL^{-1}) and LysoTracker (0.0125 × 10^{-6} M) and incubated for 40 min. Subsequently, the cells were washed and fixed as described above. Visualization was carried out using the same instrument under the same conditions. Before image analysis, the images were converted to eight-bit grayscale pictures, and the levels of colocalization were determined using ImageJ software. An image of the product of the differences from the mean (PDM), i.e., for each pixel: (blue intensity − mean blue intensity) × (red intensity − mean red intensity), was used to analyze the colocalization. In addition, Pearson correlation coefficient (PCC) values were calculated using the same software. For this purpose, at least six fields were used for the PCC calculation. PCC is a positive correlation between different channels that generates values ranging from −1 to 1. A value of 1 suggests a perfect positive linear correlation. Hence, in this case, a value of 1 would indicate total colocalization of the DACCA-labeled nanobead-based intervention with LysoTracker-positive compartments.

2.16. Flow Cytometry Investigations

Cellular internalization and intracellular degradation were studied by flow cytometry. Cell uptake of the fabricated DACCA-labeled NPs was measured via a BD FACSVerse flow cytometer (BD Biosciences, Franklin Lakes, NJ, USA). For this purpose, J774A.1 cells were incubated at 37 °C and 5% CO_2 in full DMEM. The overnight culture was seeded at a density of 200 000 cells per sample. NPs were added at a final concentration of 2 nmol mL^{-1} to the wells and incubated for 1, 5, 20, 40, 60, or 80 min. After washing with warm PBS, the cells were suspended in 0.5% bovine serum albumin (BSA, in PBS solution). Dead cells were stained with 7AAD according to the manufacturer's protocol. The measurement was repeated independently three times and in duplicate. Cell-associated fluorescence was analyzed using FlowJo 10.5.0 software (Tree Star Inc., Ashland, OR, USA).

Intracellular degradation estimation was based on a previously described method.[28] The overnight J774A.1 culture was seeded at a density of 200 000 cells per sample. NPs at a concentration of 2 nmol mL^{-1} were added to the appropriate wells and incubated for 60 min in full DMEM (37 °C, 5% CO_2). The incubation length was chosen according to the above-described internalization-related experiment, where the macrophages showed the maximum internalized NPs between 60 and 80 min of incubation. After washing with warm PBS, the cells were further incubated in particle-free full DMEM for 0, 10, 20, 30, 40, or 80 min. Cells were washed with PBS and suspended in 0.5% BSA (PBS solution); dead cells were stained with 7AAD and measured by BD FACSVerse. The measurement was repeated independently three times and in duplicate. Cell-associated fluorescence was analyzed using FlowJo 10.5.0 software.

3. Results and Discussion

3.1. Synthesis and Content of 4HB in PCL-*co*-P4HB

Previous studies that have focused on the polymerization of five-membered lactones have shown their unwillingness to undergo ring-opening polymerizations due to the low ceiling temperature.[10] However, this does not mean that the ring of five-membered lactones cannot be opened and that only the cyclic form is thermodynamically preferred. These rings do open, but there is no impetus to form high-molecular-weight polymers under normal conditions.[32,33] This is the reason why these compounds are difficult to homopolymerize but, on the other hand, are easy to incorporate into a polymer chain when copolymerization occurs with another appropriate heterocycle with a high ceiling temperature. Moreover, the extent of incorporation can also be tuned by the polymerization conditions.[10,34]

Hence, for the systematic investigation of incorporating γBL into polymer chains during copolymerization with εCL, a series of copolymerizations initiated by benzyl alcohol were performed (Figure 1A) with different copolymerization conditions. The polymerization parameters and resulting characterizations are given in Tables S1 and S2 in the Supporting Information. The data in Table S1 in the Supporting Information show the parameters depending on the feed ratio of monomers, whereas the data in Table 2 show the parameters depending on the nature of the catalyst and the solvent and the initial monomer concentrations. In total, four different catalytic systems were evaluated (structures shown in **Figure 2**A).
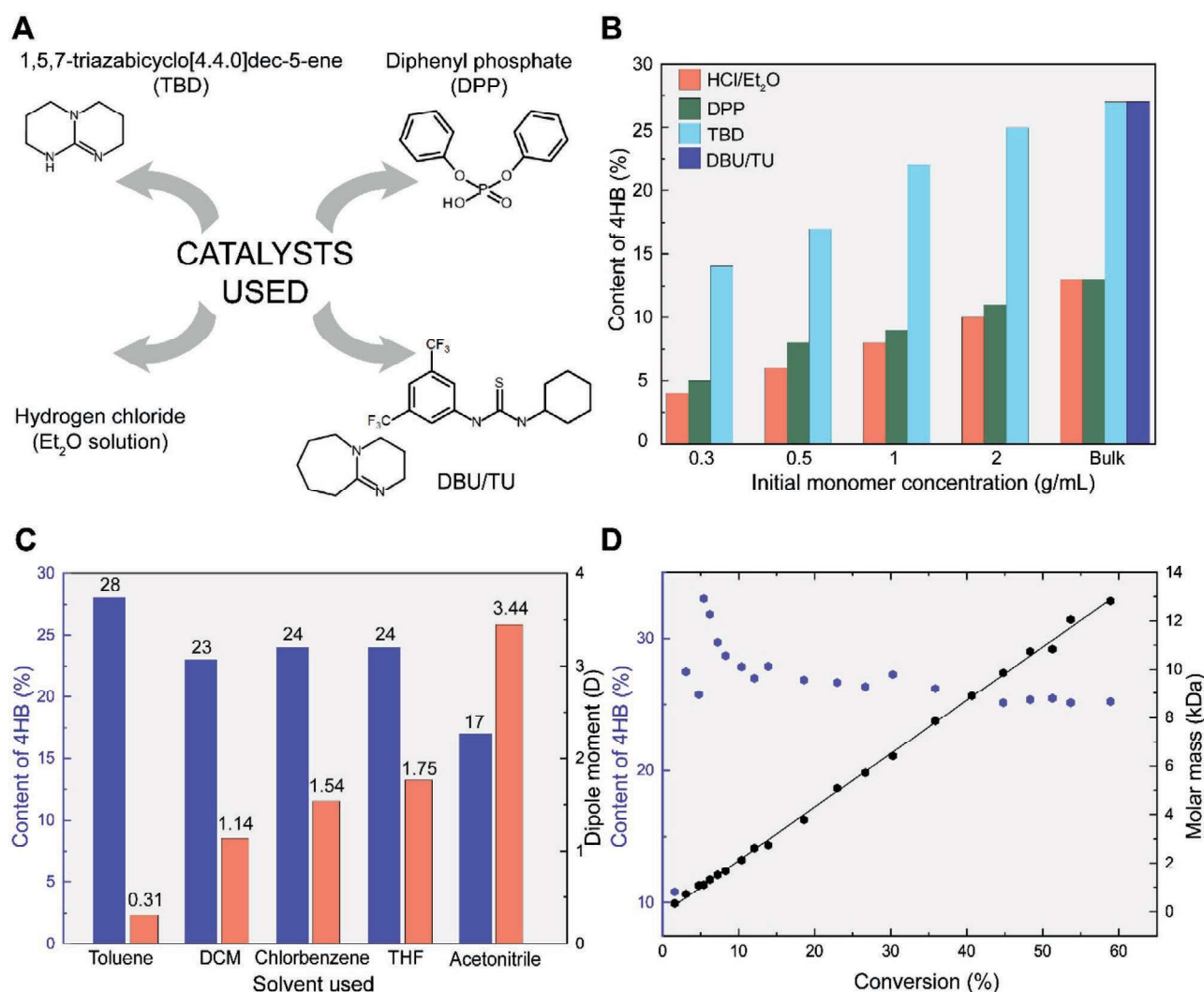
Figure 2. Copolymerization optimization. A) Different catalysts were used in subsequent studies of the content of 4HB in copolymers. B) Different initial monomer concentrations with DCM as the solvent as well as C) different solvents possessing various dipole moments were studied with TBD used the catalyst. D) The relationship between monomer consumption and the content of 4HB in the polymer chain and molar mass was studied. The εCL/γBL molar feed ratio was in all cases 1.15. Abbreviations: TBD, 1,5,7-triazabicyclo[4.4.0]dec-5-ene; DPP, diphenyl phosphate; Et$_2$O, diethyl ether; DBU, 1,8-diazabicyclo[5.4.0]undec-7-ene; TU, *N*-(3,5-bistrifluoromethyl)phenyl-*N'*-cyclohexylthiourea; DCM, dichloromethane; THF, tetrahydrofuran.

The data in Table S1 in the Supporting Information show the relationship between the monomer feed ratio and the amount of incorporated γBL. Not surprisingly, the higher the ratio of γBL in the feed, the more γBL was incorporated. The disadvantage of copolymerization with high amounts of γBL is its relatively low yield. The difference in the incorporated amount of γBL is remarkable when different catalysts were used (**P1–P4** catalyzed by HCl/Et$_2$O and **P5–P8** by TBD).

The data schematically plotted in Figure 2B show a significant difference in the incorporated amount of γBL when different catalysts were used. A higher content of 4HB units in the prepared copolymers was observed when anionic catalysts (TBD and DBU/TU) were used compared to that observed in the copolymers prepared with cationic catalysts (HCl/Et$_2$O and DPP). This fact implies that different polymerization mechanisms significantly affect the amount of incorporated γBL.

The bulk copolymerization catalyzed by DBU/TU resulted in a yield of 39% and a copolymer containing 27% 4HB units but there was no high-molecular-weight copolymer formed when solution copolymerization was carried out at any concentration. TBD was identified as the most efficient and versatile catalytic system in this study. TBD is able to incorporate a relatively high amount of γBL at any initial monomer concentration. The trend of increasing incorporated γBL amount with increasing initial monomer concentration is evident in Figure 2B.

Solvent polarity is a considerable parameter when a certain amount of γBL incorporation is needed in the polymer chain. As shown in Figure 2C, there was a marked difference in 4HB content in the copolymer composition of PCL-*co*-P4HB when the nonpolar solvent toluene was used compared to the 4HB content when polar acetonitrile was used. It should be noted that TBD is a bifunctional catalyst, in which the base site works as a H-bonding acceptor to activate the alcohol initiator, while

**ADVANCED
SCIENCE NEWS**
www.advancedsciencenews.com

**Macromolecular
Bioscience**
www.mbs-journal.de

the H-bonding donor component can activate the monomer via the coordination of the ester functionality. Thus, the noncoordinating solvent toluene enables higher incorporation of γBL in the evaluated copolymerization reaction.

The prepared copolymers were characterized by ^{1}H NMR and FTIR spectroscopy, and their structures were confirmed. The ^{1}H NMR spectra and FTIR spectra are shown in Figures S2 and S3 in the Supporting Information, respectively. The table of polymerization parameters and copolymer characteristics obtained by ^{1}H NMR spectroscopy and size exclusion chromatography can be found in Table S2 in the Supporting Information.

In addition, a ^{1}H NMR spectroscopic kinetic study was performed to understand the copolymerization behavior. TBD was used as the catalyst for this purpose and deuterated DCM was used as the solvent. The polymerization was performed in an NMR cuvette in situ and ^{1}H NMR spectra were taken periodically over time. The relative intensities of peaks corresponding to the γBL unit (δ 1.91 ppm) and the εCL unit (δ 1.33 ppm) were integrated and the following parameters were calculated. The resulting graph in Figure 2D shows the dependence of the content of 4HB and molar mass on the conversion. A moderate decrease in the content of 4HB units in the growing polymer chain with increasing conversion was observed, and the linear dependence of molar mass on conversion indicated the controlled manner of ring opening copolymerization. Additionally, the rate constants of the incorporation of γBL and εCL were determined. As the graphs in Figure S7 in the Supporting Information of the supplemental information show, εCL has been incorporated according to first-order kinetics with a rate constant of $k_{\varepsilon CL} = 4.3 \times 10^{-5}$ s^{-1}, and the incorporation of γBL follows second-order kinetics with a rate constant of $k_{\gamma BL} = 5.8 \times 10^{-6}$ dm^3 mol^{-1} s^{-1}.

3.2. Synthesis of mPEO-*b*-(PCL-*co*-P4HB)

Many studies have shown that assemblies based on poly(ethylene oxide)-*block*-polycaprolactone can be successfully used as drug carriers for many medical applications.[35,36] Copolymerization with mPEO and other hydrophilic polymers ensures or enhances the solubility of these assemblies based on the copolymers and improves the biocompatibility/nonimmunogenicity of the whole system.[37] When mPEO is

used for copolymerization, the assemblies do not show any toxicity at reasonable concentrations and are efficient when loaded with hydrophobic drugs,[27] suggesting an attractive polymeric matrix for drug delivery system preparation.

Thus, this work aimed to study the impact of 4HB disturbance on hydrophobic block regularity and on the biorelevant properties of mPEO-based assemblies. Given this, the most efficient conditions for incorporating γBL via the copolymerization initiated by BA were implemented (see above) and the copolymerization was conducted via ROP in the same manner and in the presence of the macroinitiator mPEO (Figure 1B). The macromolecular parameters of the prepared block copolymers are listed in **Table 1**. Samples **B2–B5** differ in hydrophobic ratio and macromolecular molar mass (i.e., mPEO) and in the molar mass of the samples themselves. The ^{1}H NMR spectrum of mPEO-*b*-(PCL-*co*-P4HB) with signal assignment is shown in Figure S6 in the Supporting Information. Moreover, the ^{13}C NMR spectrum in Figure S14 in the Supporting Information gave as detailed information about the copolymer microstructure. It proved that the distribution of CL and 4HB units along polyester block is very likely random.[38]

Sample mPEO$_{44}$-*b*-PCL$_{81}$ **B1** was synthesized in the absence of γBL for comparison of the properties with those of samples **B2** and **B3**. The critical aggregation concentrations were determined and the values are listed in Table 1. The CAC-related curves are shown in Figure S8 in the Supporting Information.

The one-step synthesis of labeled mPEO-*b*-(PCL-*co*-P4HB) with fluorescent dye was performed. DACCA was used for this purpose and the reaction scheme is shown in Figure S12 in the Supporting Information. The efficiencies of the reactions were determined by the standard addition method (free 7-(diethylamino)coumarin-3-carboxylic acid) and were found to be ≈45% by UV–vis spectroscopy. The absolute amounts of DACCA occurring in the polymeric matrices are listed in Table 1. The excitation and emission spectra at the excitation wavelength of 420 nm of free 7-(diethylamino)coumarin-3-carboxylic acid and samples of **B1–B5** are shown in Figure S13 in the Supporting Information.
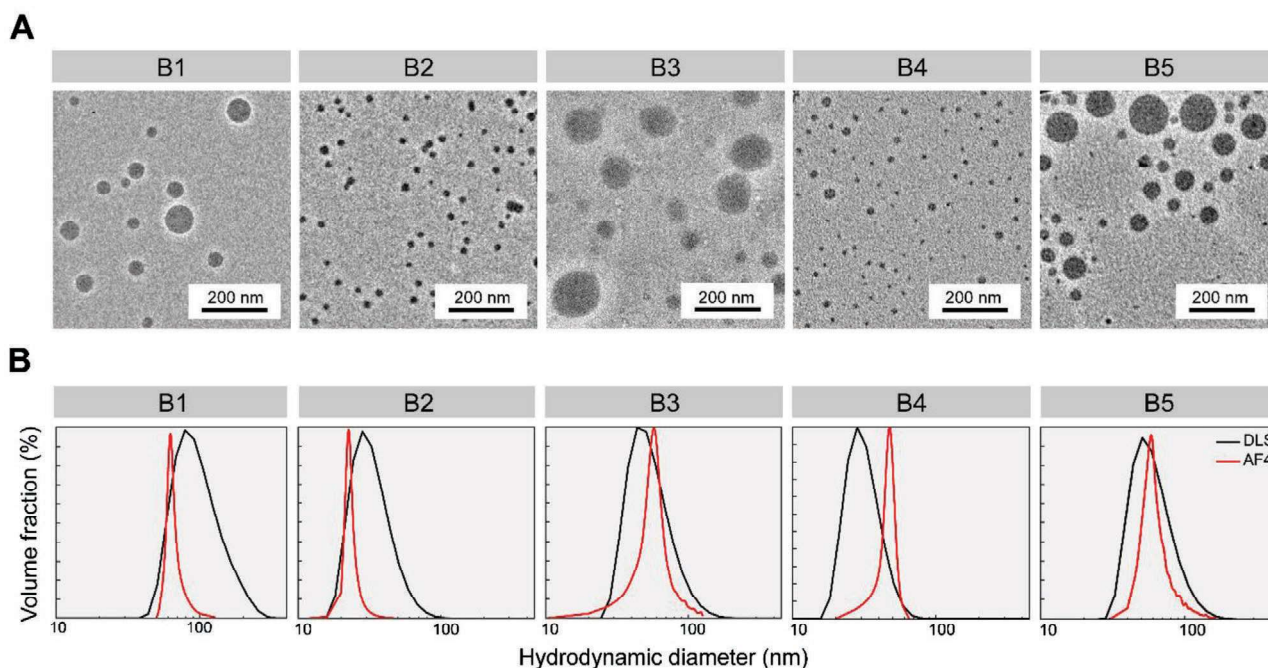
3.3. Characterization of the Nanoparticles

The fabricated copolymers (**B1–B5**) were used for NP preparation. For this purpose, the nanoprecipitation method described

Table 1. Composition and characteristics of polymers initiated by poly(ethylene oxide) monomethyl ether (mPEO) using TBD as the catalyst.

No.	Copolymer	HH-ratio[a]	Yield [%]	$f_{\gamma BL}$[b] [%]	$M_n^{NMRc)}$	$M_n^{SECd)}$	$Đ^{SECd)}$	CAC[e] [μg mL^{-1}]	DACCA[f] [μg mg^{-1}]
B1	mPEO$_{45}$-*b*-PCL$_{81}$	4.6	92	0	11 200	8300	1.21	9	20
B2	mPEO$_{45}$-*b*-(PCL$_{39}$-*co*-P4HB$_{13}$)	2.8	62	20	7500	6700	1.45	15	9
B3	mPEO$_{45}$-*b*-(PCL$_{55}$-*co*-P4HB$_{19}$)	4.0	60	21	9900	10 500	1.58	11	10
B4	mPEO$_{114}$-*b*-(PCL$_{41}$-*co*-P4HB$_{12}$)	1.1	63	18	10 800	7600	1.25	14	7
B5	mPEO$_{114}$-*b*-(PCL$_{124}$-*co*-P4HB$_{45}$)	3.6	59	21	23 000	12 300	1.61	10	4

[a]The hydrophobic ratio was defined as (M_n, hydrophobic block)/(M_n, hydrophilic block), where the M_n of the hydrophilic block was held at either 2000 or 5000 depending on which macroinitiator was used; [b]The polymer composition ratios of hydrophobic blocks were calculated using ^{1}H NMR data by dividing the integrated peaks of the repeating unit of γBL (δ 1.95 ppm) by the sum of the integrated peaks of γBL and εCL (δ 1.37 ppm); [c]The molecular weights were calculated using ^{1}H NMR by integrating the methoxy peak of mPEO at 3.37 ppm and the peak for the repeating units of εCL and γBL; [d]Determined by SEC using tetrahydrofuran as the eluent; [e]Critical aggregation concentrations were determined at room temperature in PBS; [f]When DACCA-labeled copolymers were used, the content of DACCA was determined by UV–vis spectroscopy.

ADVANCED
SCIENCE NEWS
www.advancedsciencenews.com

Macromolecular
Bioscience
www.mbs-journal.de

A

B

Figure 3. A) Cryo-TEM images and B) curves obtained from DLS and AF4.

in detail in the Experimental Section was used. The physico-chemical characterization of the NPs was performed via cryo-TEM, DLS, SLS, and AF4 experiments.

It was hypothesized that the supramolecular structure of the mPEO-*b*-(PCL-*co*-P4HB)-based assemblies correlated to the structure of mPEO-*b*-PCL in some respects, as the only difference was the aliphatic chain length between the ester bonds in the repeating units. In the context of mPEO-*b*-PCL assemblies, several architectures were described in the literature, depending on the hydrophobic/hydrophilic ratio.[35,39] Note that if the solvent switch is fast during NP preparation, block copolymers tend to form spherical structures instead of cylindrical or planar ones because this is the fastest way to reduce the interfacial area.[28] This is in line with the cryo-TEM investigations that revealed that all of the samples inspected were found to largely be spherical polymeric nanoparticles (**Figure 3**A) with diameters in mutual agreement with those found by DLS, SLS, and AF4 (**Table 2**).

The DLS distribution functions (Figure 3B) are portrayed as relatively narrow peaks, with diameters ranging from ≈40–110 nm

depending on the block lengths. To verify these findings, we performed additional AF4 experiments that provided the actual sizes and molecular weights. These values are in mutual agreement with those obtained by DLS or SLS. It should be noted, however, that light scattering techniques usually overestimate the size of particles.[36,40] In addition, the samples for the AF4 measurements were filtered through large-pore polyvinylidene fluoride filters (0.8 μm), as AF4 is not as sensitive to dust as conventional light scattering techniques. Thus, any influence of filtration on the size distribution of the nanoparticles can be excluded.

The DLS and AF4 results together with the cryo-TEM investigations allowed for us to obtain insight into the structure of the NPs. In the literature,[39,41,42] mPEO-*b*-PCL-based assemblies are often stated to be micelles. The AF4-estimated molecular weight values (Table 2), however, indicate that ≈400–9000 polymer chains comprise one nanoparticle. Micelles, in contrast, contain ≈10–100 polymer chains.[43]

The apparent structural density (ρ) of the particles was calculated as an equivalent average density from the average of the

Table 2. Characterization of nanoparticles.

Sample	$D_H^{DLS\,a)}$ [nm]	PDI$^{a)}$ DLS	$D_G^{SLS\,b)}$ [nm]	$M_W^{SLS\,b)}$ [kDa]	$\rho^{SLS\,c)}$ [g mL^{-1}]	$D_G^{AF4\,b)}$ [nm]	$M_W^{AF4\,b)}$ [kDa]	$\rho^{AF4\,c)}$ [g mL^{-1}]	$N_{agg}^{AF4\,d)}$
B1	109	0.113	91	14 900	0.029	77	101 400	0.324	9050
B2	41	0.188	40	5800	0.134	26	8160	0.690	710
B3	71	0.166	120	13 800	0.012	85	24 700	0.060	1110
B4	36	0.109	48	1000	0.013	47	4180	0.060	420
B5	71	0.111	170	38 100	0.011	103	66 700	0.091	2510

$^{a)}$The Z-average of the hydrodynamic diameter D_H and polydispersity index PDI; $^{b)}$The molecular weight M_W and the Z-average of the diameter of gyration D_G; $^{c)}$The apparent structural density was calculated from the equation $\rho = 6M_W/\pi N_A D^3$ considering a spherical shape ($D = 1.29 \cdot D_G$); $^{d)}$The aggregation number is the quotient of the M_W of the particles (AF4) and the M_W of the polymer (SEC).

ADVANCED
SCIENCE NEWS
www.advancedsciencenews.com

Macromolecular
Bioscience
www.mbs-journal.de

molecular weight M_w using the model of a sphere with a diameter of $D = 1.29 \, D_G$; therefore, $\rho = 6M_w/\pi N_A D^3$. On average, the density of the mPEO-*b*-(PCL-*co*-P4HB) nanoparticles was three times lower than the density of the mPEO-*b*-PCL nanoparticles. Given this finding, we hypothesized that the 4HB-possessing NPs were less dense due to their irregular structure (two repeating units) within the hydrophobic core. This also means that the core of the mPEO-*b*-(PCL-*co*-P4HB) nanoparticles was less hydrophobic than that of the mPEO-*b*-PCL nanoparticles, which may influence cargo encapsulation. However, this issue was not addressed further.

One of the advantages of the AF4 method over conventional light scattering methods or cryo-TEM is the capability of AF4 to detect eventual nonassembled polymers in solution. The AF4 investigations revealed that no free nonassembled polymer was found in any of the samples investigated in this work. This is probably due to the favorably low estimated CAC values (i.e., 9–15 µg mL⁻¹) and supports the above-discussed fact that our assemblies are not micelles, which are known to be in thermodynamic equilibrium with unimers, but instead are probably nanogel-like polymeric NPs.

The described complex characterization of NPs allowed for us to fine-tune the nanoparticle parameters so that the particles could be designed more precisely in the future according to the particular application requirements.

3.4. ¹H NMR-Assessed Degradation

The enzyme-catalyzed degradation of the NPs was investigated using ¹H NMR. The degradation was observed as a decrease in the intensity of the proton signal of ε-caprolactone units in sample **B1** and ε-caprolactone and γ-butyrolactone units in sample **B3** during the experiment. Samples **B1** and **B3** were chosen for this more detailed study due to the comparable sizes of the blocks in these copolymers. For the quantitative characterization of the enzymatic degradation of the PCL and PCL-*co*-P4HB blocks, the time dependence of PCL and PCL-*co*-P4HB consumption was calculated for the measured samples. The integral intensity of the signal marked as "g" (Figure S9, Supporting Information) was defined as 2 (there are two equivalent protons) and used as an internal standard for monitoring degradation in the NMR spectra. Subsequently, the integral intensity of the signal "i + l" (Figure S9, Supporting Information) was used to calculate the percentage of PCL and PCL-*co*-P4HB blocks according to the relationship $[(I_t^{i+l}/I_0^{i+l}) \times 100]$, where the subscripts 0 and t represent the time points during degradation with $t = 0$ (i.e., before lipase addition) and $t = t$ (i.e., after lipase addition), respectively.

The results are shown in Figure S10 in the Supporting Information. It is evident that sample **B1** degraded faster than sample **B3**. Figure S9 in the Supporting Information shows the ¹H NMR spectra of **B3**-based NPs that were measured in deuterated PBS at 37 °C before (A) and after (B, C) lipase addition. The chemical structures and signal assignments are presented in the same figure. The comparison between the spectra was recorded in a solvent suitable for all of the blocks (deuterated chloroform, cf. Figure S6, Supporting Information) and PBS (Figure S9, Supporting Information), showing that the

broader signals obtained from the PCL-*co*-P4HB hydrophobic block and the strong signals obtained from the hydrophilic mPEO demonstrate the presence of core–shell formation in the deuterated PBS system. These results demonstrate that the PCL-*co*-P4HB protons were restricted in mobility in the moderately hydrated solid-like core of the NPs, while the mPEO blocks created a liquid-like shell. After the addition of lipase, the intensity of the side methyl signals from the PCL-*co*-P4HB monomer unit ("i + l" and "j, e" protons, see Figure S9, Supporting Information) decreased, while the singlets related to the "f + h" and "k" protons split and the mPEO signals ("a", "b") remained unchanged. The second effect observed in this spectrum was the appearance of new signals related to the degradation products, which were identified as 6-hydroxyhexanoic acid and 4-hydroxybutanoic acid (Figure S9, Supporting Information).

Additionally, due to the appearance of the signals at 4.1, 2.2, and 2.0 ppm in Figure S9 in the Supporting Information, there was confirmation of an intermediate product during the degradation appeared before final the products (6-hydroxyhexanoic acid and 4-hydroxybutyric acid). From the chemical shifts of signals of this intermediate product, especially the peak at 4.1 ppm, which was shifted downfield to its respective signal from the polymer (i + l at 4.0 ppm), there was a high probability that this compound was a small cycle made from a small amount of CL and BL units. To support these considerations, one sample was chosen for ¹H 2D diffusion-ordered NMR spectroscopy experiments, which were measured before lipase addition (Figure S11, Supporting Information red spectrum) and 24 h after lipase addition (Figure S11, Supporting Information blue spectrum). From those spectra it followed that the intermediate product was still not fully degraded after this time and had a slightly lower self-diffusion coefficient (higher molecular weight) than that of the final products (6-hydroxyhexanoic acid).

The degradation process of the copolymer was confirmed by SEC analysis. The products of degradation were collected in different times. As evident in Figure S15 in the Supporting Information, the degradation of the copolymer was already significant in the first hour of the action of the lipase.

3.5. Cytotoxicity Evaluation

To assess the biorelevant properties of the manufactured NPs, their cytotoxicity and hemolytic activity were analyzed in terms of their interactions with red blood cells (RBCs) and their behavior in monocyte-macrophage cultures, as these cells are one of the first contact partners after systemic administration. In addition, the goal of this evaluation was to answer the questions of whether our synthetized NPs are safe and whether the biocompatibility of P4HB-based assemblies is affected when P4HB is introduced within the Food and Drug Administration-approved mPEO-*b*-PCL copolymer.[44] The mPEO-*b*-PCL copolymer was found to possess no or only minor toxic effects on the cell viability of different cells, such as the murine monocyte-macrophage cell line Raw 264.7,[27,28] zebrafish embryonic fibroblast cell line ZF4,[28] human hepatocellular carcinoma cell line HepG2,[42,45] and prostate cancer cell lines LNCaP and PC-3.[46]

ADVANCED
SCIENCE NEWS
www.advancedsciencenews.com

Macromolecular
Bioscience
www.mbs-journal.de
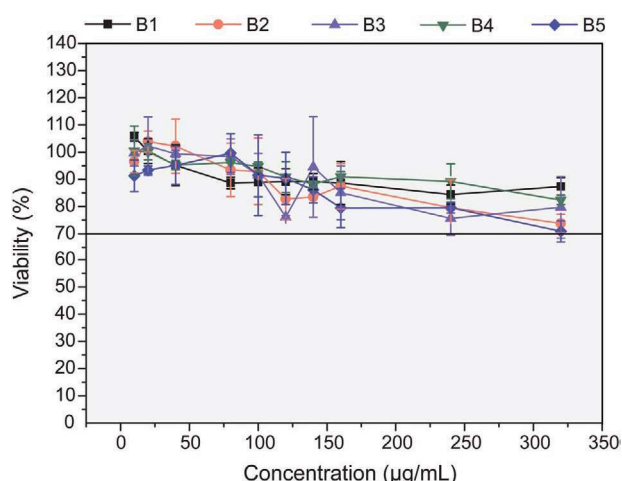
Figure 4. Viability of J774A.1 cells as detected by an MTT assay. Mϕs were incubated with different concentrations of the fabricated NPs for 24 h and their viability was analyzed via measurement of the concentration of metabolically produced formazan. The horizontal line in the panel indicates the level at which, in terms of cell viability, the distinction between cytotoxic (above) and noncytotoxic (below) was made.

First, we studied the effects of the prepared formulations **B1–B5** in terms of possible cytotoxicity by using the MTT method after a 24 h incubation of J774A.1 Mϕs with each prepared nanoformulation. As evident in **Figure 4**, the cell viability was influenced very little. The copolymer cytotoxicity was nearly negligible at clinically relevant concentrations. In the hemolytic study, none of the analyzed formulations (**B1–B5**) induced hemolysis within the tested concentration range (100–800 µg mL^{-1}) after an 8 h incubation at 37 °C.

Not surprisingly, the use of nanomedicines bears the risk of unwanted side effects.[44] Hence, an important step in the development of nanobead-based products is the assessment of any safety risks. Considering this, our results demonstrate that P4HB introduction within the copolymeric matrix did not affect its acute biocompatibility with both J774A.1 cells and RBCs.

3.6. Uptake and Intracellular Degradation Study

Our research group strives to rationally design nanobead-based interventions to benefit from the combination of the specific properties of NPs and those of biocompatible and biodegradable polymers in one self-assembled formulation allowing for drug delivery. Given this background, one of the crucial studied aspects was the question of whether the 4HB unit-possessing NPs could be taken up by J774A.1 Mϕs as a model cell type, which is an important subject of drug delivery research. Mϕs are the main hosts of intracellular pathogens and, thus, are pursued as a therapeutic target for the intracellular delivery of antibiotics. In addition, Mϕs have gained increasing interest as a therapeutic target for cancer immunotherapy due to its complex roles in the tumor microenvironment.[47]

The DACCA-labeled copolymers were visualized inside the J774A.1 cells using CLSM after an incubation time of 40 min. The microscopy study showed that all of the formulations tested, i.e., mPEO-*b*-PCL and mPEO-*b*-(PCL-*co*-P4HB), were

successfully internalized in Mϕs (**Figure 5**), suggesting that such systems are usable as a logical strategy for effectively killing intracellular microbes.[48] Note that slight differences between the intracellular distribution patterns were evident. In other words, some of the samples revealed bright cytosolic localization (e.g., **B4**) compared to the vesicle-localized samples (e.g., **B1**). These findings seem to be in line with our previous mPEO-*b*-PCL-focused study,[28] which confirmed that control of the NP physicochemical properties also allows for control of their biorelevant behavior.

Given this, for a better view of the interactions between the NPs and J774A.1 cells, a marker for low pH compartments (i.e., presumably lysosomes) was applied to visualize the colocalization of the NPs. The cells were incubated for 40 min with DACCA-labeled NPs and LysoTracker Deep Red. These experiments indicated that all of the NP samples tested (**B1–B5**) were able to target acidic organelles (**Figure 6**), which was also proven by the analysis in terms of the PDM images and PCC value calculations. However, the DACCA-labeled nanoparticle colocalization with lysosomes was not found to be exclusive, as suggested by the PCC values found (0.43–0.59, **Figure 6**). As mentioned above, Pearson correlation analysis generates values ranging from −1 to 1, where a value of 1 suggests full colocalization. In other words, these results suggest that the nanocarriers are within low-pH compartments. It should be noted that this finding seems to be in line with our previous study.[27,28] Ultrastructural analysis by TEM revealed that mPEO-*b*-PCL nanoparticles can be found both within vesicular structures and freely in the cytoplasm within Raw 264.7 macrophage-like cells.

To study the cellular internalization kinetics of the NPs within J774A.1 Mϕs, DACCA-labeled NPs (2 nmol mL^{-1}) were added to Mϕ monolayers and incubated for different times. Subsequently, the cellular uptake was analyzed using flow cytometry (**Figure 7**A). All of the obtained cell-associated fluorescence data were normalized to the maximum fluorescence values to ensure the comparability of the results determined from samples with variable total cell fluorescence intensities.[28]
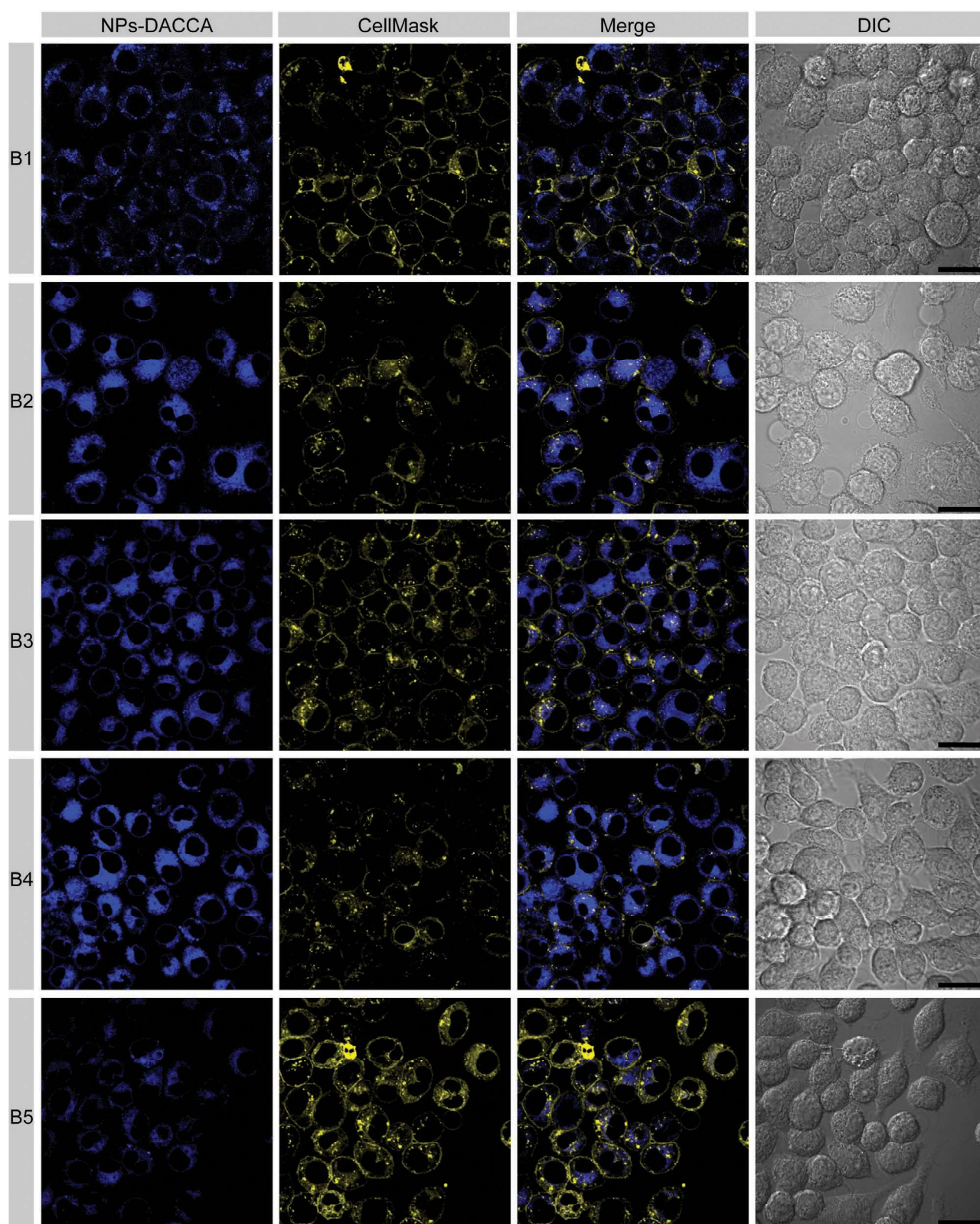
As shown in Figure 7A, the fabricated NPs were successfully taken up by J774A.1 cells, and the cell-associated fluorescence intensity increased as the incubation time increased for all of the samples tested. A maximum cell fluorescence intensity was reached after 60–100 min of incubation (Figure 7A); the data were normalized to the plateau-corresponding values of fluorescence, individually. Subsequently, internalization half-time values (Figure 7A) were calculated based on the internalization time course by curve-fitting of the data using the following equation[49]

$$F(t) = F_0 + (F_{\text{plateau}} - F_0)\left(1 - e^{-tk}\right) \qquad (2)$$

where $F(t)$ is the cell fluorescence signal at time t, F_0 and F_{plateau} are the initial fluorescence signal and the maximum signal, respectively, and k is the internalization rate constant. The half-time of internalization ($\tau_{1/2}$) was calculated as the ratio of ln 2 and k.
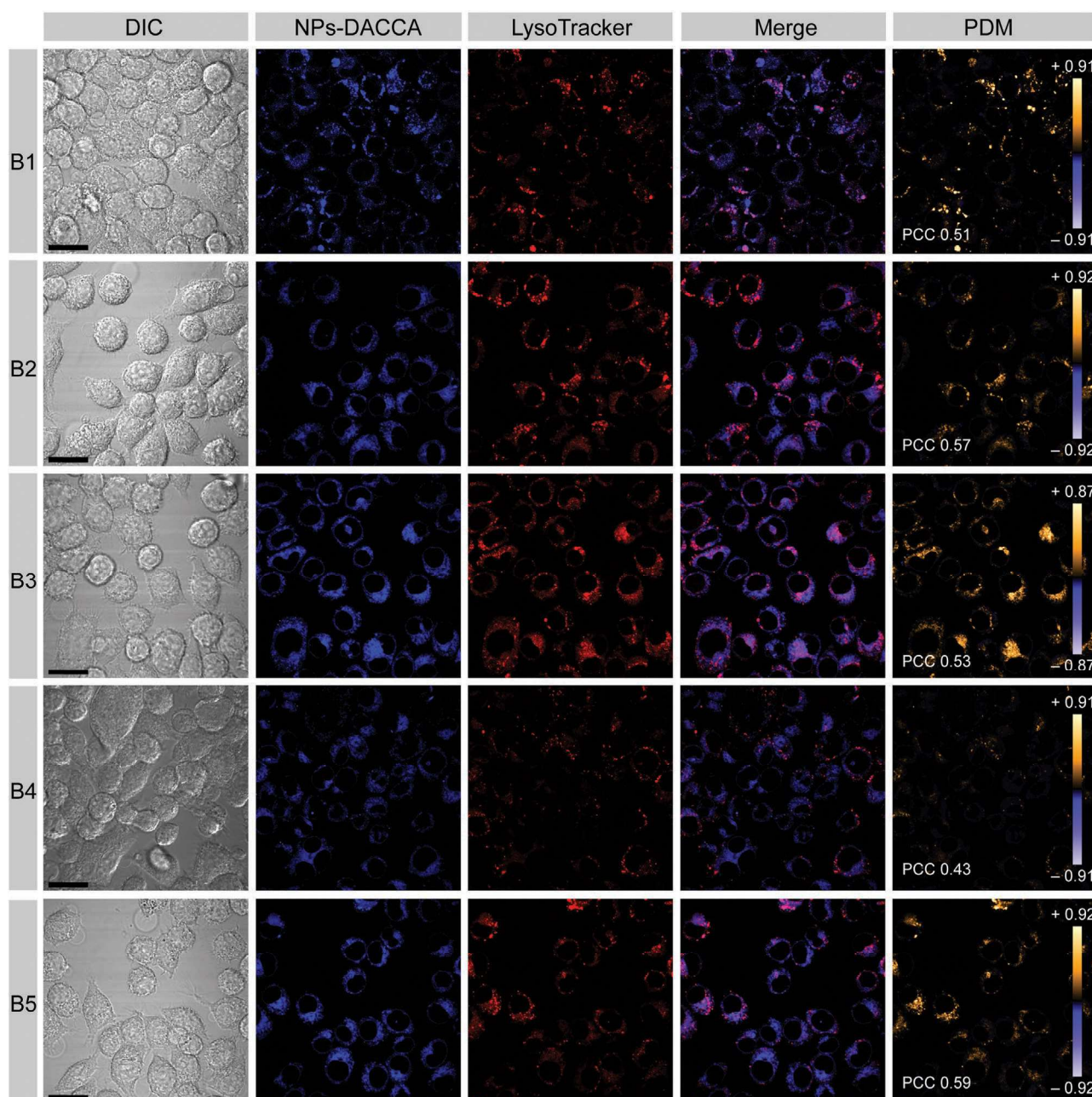
The cellular uptake of nanobeads, in general, depends on several factors, such as the size, charge, shape, and

ADVANCED
SCIENCE NEWS

www.advancedsciencenews.com

Macromolecular
Bioscience

www.mbs-journal.de

Figure 5. Study of DACCA-labeled NP uptake by J774A.1 cells. Fluorescence and differential interference contrast (DIC) images of J774A.1 cells are shown 40 min after the addition of DACCA-labeled NPs (2.8 nmol mL^{-1}, blue fluorescence). The plasma membrane-related CellMask Deep Red signal is pseudocolored in yellow. Scale bars: 20 µm.
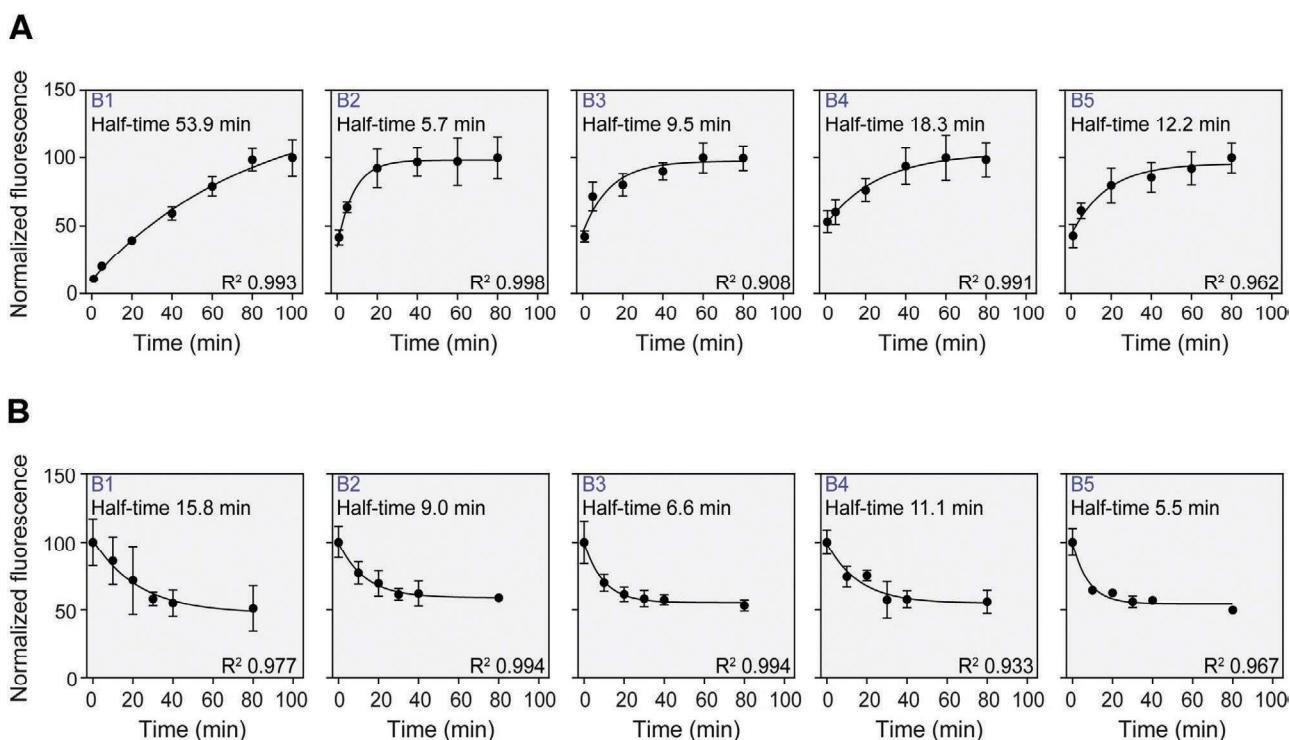
1900408 (11 of 15)

**ADVANCED
SCIENCE NEWS**
www.advancedsciencenews.com

**Macromolecular
Bioscience**
www.mbs-journal.de

Figure 6. Study of DACCA-labeled NP localization within J774A.1 cells. CLSM images of J774A.1 Mϕs 40 min after the addition of DACCA-labeled NPs (2.8 nmol mL^{-1}) and LysoTracker. The analysis of colocalization was allowed by both the product of the differences from the mean (PDM) images and Pearson correlation coefficient (PCC) values. The PDM images are pseudocolored; each pixel is equal to the PDM value at that location and a PDM scale bar was inserted. The orange color indicates colocalized pixels and the blue color suggests segregation. Scale bars: 20 μm. DIC denotes differential interference contrast.

hydrophilic/hydrophobic ratio of the NPs.[42,50] Not surprisingly, the resulting uptake kinetics are then based on a combination of such parameters. Thus, a group of nanocarriers possessing several different variable properties makes interpretation of the kinetic results harder.[28] Despite this fact, the kinetics study carried out revealed a phenomenon worth mentioning; it was found that the P4HB-free mPEO$_{45}$-b-PCL$_{81}$-based sample **B1** exhibited a considerably high internalization $\tau_{1/2}$ value ($\approx$54 min) compared to that of the rest of the samples analyzed.

Notably, the mPEO$_{45}$-b-(PCL$_{55}$-co-P4HB$_{19}$) copolymer (**B3**) exhibited an internalization $\tau_{1/2}$ of $\approx$9.5 min, even when having the same hydrophilic/hydrophobic ratio as that of **B1** as well as the same molecular weight. This may be due to the change in crystallinity and/or NP size, one of the main physicochemical aspects that influence cellular uptake. This finding suggests that the introduction of P4HB can strongly affect the biorelevant properties of such nanobead-based interventions. Such a hypothesis, however, must be investigated in

**ADVANCED
SCIENCE NEWS**
www.advancedsciencenews.com

**Macromolecular
Bioscience**
www.mbs-journal.de

Figure 7. Study of DACCA-labeled NP fate. A) Time course of cell-associated fluorescence after the addition of 2 nmol mL^{-1} DACCA-labeled formulations. The data were normalized to the maximum fluorescence values (i.e., the plateau values reached). B) Time course of NP degradation observed after the monolayers were incubated with 2 nmol mL^{-1} DACCA-labeled formulations for 60 min. Both half-time and R squared values are shown. Note that **B1** exhibited different internalization as well as degradation kinetics compared to those of formulation **B3**, even when having the same hydrophilic/hydrophobic ratio as well as the same molecular weight.

more detail to come to any specific conclusions in terms of this phenomenon.

As mentioned above, a plateau in the cell-associated fluorescence was reached after 60–100 min of incubation with the DACCA-labeled formulations. Subsequently, a decrease in the cell-associated fluorescence values was observed (data not shown), as the enzymatic degradation of the DACCA-labeled matrix leads to quenching of its fluorescence.[27] Hence, to study the intracellular degradation kinetics, DACCA-labeled NPs (2 nmol mL^{-1}) were added to Mϕ monolayers and incubated for 60 min for each of the formulations tested. Subsequently, the cells were washed with PBS (i.e., time 0) and analyzed using flow cytometry at different time points (Figure 7B). The degradation rate constant values were determined by fitting the data to a single exponential decay model. The half-time of degradation was calculated as the ratio of ln 2 and the degradation rate constant.

In our recent study,[28] we suggested that there is a relationship between the lysosomal localization of a nanocarrier and its degradation kinetics in vitro. In other words, mPEO-b-PCL-based NPs with cytosolic localization within Raw 264.7 Mϕs exhibited slow intracellular degradation, and, vice versa, fast intracellular degradation was observed in the case of NPs colocalized with lysosomes, i.e., lipase-rich compartments.[51] It is evident from Figure 7B that all of the nanoformulations analyzed (i.e., **B1**, **B2**, **B3**, **B4**, and **B5**) revealed similar degradation patterns, probably because all of the samples exhibited similar colocalization within low-pH compartments. Similar to the uptake kinetics study, the P4HB-free sample **B1** was the

most distinct, as it revealed the slowest degradation rate ($\tau_{1/2}$ of ≈16 min), which also suggests that the introduction of P4HB seems to be able to tune the biorelevant properties of the NPs. Similar to our recent study,[28] the flow cytometry results were not in line with the above-described ^{1}H NMR degradation study. This is probably because the ^{1}H NMR study was carried out in PBS only (i.e., without the presence of FBS or cell proteins), as protein-NP interactions play a crucial role in the biorelevant behavior. For the same reason, the flow cytometry results may be deemed to be more relevant, because they reflect interactions in biorelevant environments (i.e., in the presence of serum and intracellular proteins).

It is worth mentioning that enzymatic degradability suggests favorable behavior in vivo, as it can be assumed that the mPEO-b-(PCL-co-P4HB) copolymers undergo degradation to mPEO, 6-hydroxyhexanoic acid (the degradation product of PCL) and 4-hydroxybutyric acid. Both mPEO$_{44}$ (2000 Da) and mPEO$_{113}$ (5000 Da) do not exceed the threshold for the renal filtration of polymers 30–50 kDa.[52] The biocompatible 6-hydroxyhexanoic acid is converted to adipic acid by ω-oxidation in the endoplasmic reticulum of liver and kidney cells in vivo. Adipic acid is then metabolized by β-oxidation and the Krebs cycle to carbon dioxide and water.[53] Similarly, 4-hydroxybutyric acid is a ubiquitous molecule in vivo, derived both endogenously and exogenously and is catabolized by processes including β-oxidation to acetyl-CoA and glycolate, α-oxidation to 3-hydroxypropionate-CoA and formate, and cleavage of C-4 to yield 3-hydroxypropionate and carbon dioxide.[54]

4. Conclusions

The aim of this work was to describe, fundamentally characterize, and perform biorelevant analyses of biocompatible and biodegradable nanocarriers based on mPEO-*b*-(PCL-*co*-P4HB), where the γBL introduction would hopefully serve as a biorelevant behavior-controlling mechanism.

First, it has been shown that the copolymer composition of PCL-*co*-P4HB can be tuned not only by the feed ratio of the monomers but also by choosing a feasible catalyst. The difference in γBL incorporation was demonstrated when anionic or cationic catalysts were employed. A notable increase in incorporation was observed when anionic catalysis in a nonpolar environment were employed. The content of incorporated γBL was $\approx$30% when TBD was used as a catalyst of the copolymerization in toluene.

Additionally, we studied the biorelevant properties of P4HB-based nanocarriers. Their biocompatibility, cellular uptake, and degradation were evaluated. By combining flow cytometry and CLSM, we demonstrated that these nanocarriers can be internalized by macrophage-like cells in which the NPs underwent intracellular degradation. The influence of the presence of the γBL units on the biological behavior was observed. This method enabled control over the rate of degradation so that when the content of γ-butyrolactone increased, the rate of degradation increased.

Given our findings, this study provides a generalizable strategy for the future improvement of polyester nanobead-based interventions in application fields where fine-tuned properties are needed.

Supporting Information

Supporting Information is available from the Wiley Online Library or from the author.

Conflict of Interest

The authors declare no conflict of interest.

Author Contributions

T.U. synthesized the polymers, carried out the physicochemical characterizations of both the polymers and nanoparticles, and wrote the paper. J.T. carried out the cytotoxicity and confocal microscopy experiments and wrote the paper. D.R. performed the AF4 experiments. K.G. performed the flow cytometry investigations. R.K. performed and evaluated the ^{1}H NMR analysis. M.Š. supervised the TEM investigations. M.S. supervised the AF4 experiments and evaluated the results. O.Š.J. supervised the flow cytometry investigations and cell-associated fluorescence data fitting. M.H. supervised the project and contributed to the final version of the paper.

[1] V. P. Torchilin, *Pharm. Res.* **2006**, *24*, 1.
[2] R. Palao-Suay, L. G. Gómez-Mascaraque, M. R. Aguilar, B. Vázquez-Lasa, J. S. Román, *Prog. Polym. Sci.* **2016**, *53*, 207.
[3] I. Schlachet, J. Trousil, D. Rak, K. D. Knudsen, E. Pavlova, B. Nyström, A. Sosnik. *Carbohydr. Polym.* **2019**, *212*, 412.
[4] A. C. Albertsson, I . K. Varma, *Biomacromolecules* **2003**, *4*, 1466.
[5] P. Markland, V. C. Yang, *Encyclopedia of Pharmaceutical Technology*, Vol. *1*, 3rd ed. (Ed: J. Swarbrick), Informa Helthcare USA, New York **2007**.
[6] L. S. Nair, C. T. Laurencin, *Prog. Polym. Sci.* **2007**, *32*, 762.
[7] T. Moore, R. Adhikari, P. Gunatillake, *Biomaterials* **2005**, *26*, 3771.
[8] A. Nakayama, N. Kawasaki, S. Aiba, Y. Maeda, I. Arvanitoyannis, N. Yamamoto, *Polymer* **1998**, *39*, 1213.
[9] D. P. Martin, S. F. Williams, *Biochem. Eng. J.* **2003**, *16*, 97.
[10] P. Olsén, K. Odelius, A. C. Albertsson, *Biomacromolecules* **2016**, *17*, 699.
[11] D. Myers, A. Cyriac, C. K. Williams, *Nat. Chem.* **2015**, *8*, 3.
[12] W. H. Carothers, *Chem. Rev.* **1931**, *8*, 353.
[13] F. Korte, W. Glet, *J. Polym. Sci, Part B: Polym. Lett.* **1966**, *4*, 685.
[14] K. Yamashita, K. Yamamoto, J.-i. Kadokawa, *Chem. Lett.* **2014**, *43*, 213.
[15] M. Hong, E. Y.-X. Chen, *Nat. Chem.* **2015**, *8*, 42.
[16] M. Hong, E. Y.-X. Chen, *Angew. Chem., Int. Ed.* **2016**, *55*, 4188.
[17] N. Zhao, C. Ren, H. Li, Y. Li, S. Liu, Z. Li, *Angew. Chem., Int. Ed.* **2017**, *56*, 12987.
[18] L. Lin, D. Han, J. Qin, S. Wang, M. Xiao, L. Sun, M. Yuezhong, *Macromolecules* **2018**, *51*, 9317.
[19] C.-J. Zhang, L.-F. Hu, H.-L. Wu, X.-H. Cao, X.-H. Zhang, *Macromolecules* **2018**, *51*, 8705.
[20] P. Walther, W. Frey, S. Naumann, *Polym. Chem.* **2018**, *9*, 3674.
[21] Y. Shen, Z. Zhao, Y. Li, S. Liu, F. Liu, Z. Li, *Polym. Chem.* **2019**, *10*, 1231.
[22] M. Hong, X. Tang, B. S. Newell, E. Y. X. Chen, *Macromolecules* **2017**, *50*, 8469.
[23] P. Walther, S. Naumann, *Macromolecules* **2017**, *50*, 8406.
[24] N. Dolan, D. P. Gavin, A. Eshwika, K. Kavanagh, J. McGinley, J. C. Stephens, *Bioorg. Med. Chem. Lett.* **2016**, *26*, 630.
[25] L. Luo, J. Tam, D. Maysinger, A. Eisenberg, *Bioconjugate Chem.* **2002**, *13*, 1259.
[26] S. Petrova, D. Klepac, R. Konefał, S. Kereïche, L. Kováčik, S. K. Filippov, *Macromolecules* **2016**, *49*, 5407.
[27] J. Trousil, S. K. Filippov, M. Hrubý, T. Mazel, Z. Syrová, D. Cmarko, S. Svidensk, J. Matějková, L. Kováčik, B. Porsch, R. Konefał, R. Lund, B. Nyström, I. Raškab, P. Štěpánek, *Nanomedicine* **2017**, *13*, 307.

**ADVANCED
SCIENCE NEWS**

www.advancedsciencenews.com

**Macromolecular
Bioscience**

www.mbs-journal.de

[28] J. Trousil, Z. Syrová, N.-J. K. Dal, D. Rak, R. Konefał, E. Pavlova, J. Matějková, D. Cmarko, P. Kubíčková, O. Pavliš, T. Urbánek, M. Sedlák, F. Fenaroli, I. Raška, P. Štěpánek, M. Hrubý, *Biomacromolecules* **2019**, *20*, 1798.

[29] M. Bauer, C. Lautenschlaeger, K. Kempe, L. Tauhardt, U. S. Schubert, D. Fischer, *Macromol. Biosci.* **2012**, *12*, 986.

[30] P. Ralph, M. A. Moore, K. Nilsson, *J. Exp. Med.* **1976**, *143*, 1528.

[31] *Biological Evaluation of Medical Devices – Part 5: Tests for In Vitro Cytotoxicity*, International Organization for Standardization, Geneva, Switzerland **2009**.

[32] A. Duda, S. Penczek, P. Dubois, D. Mecerreyes, R. Jérôme, *Macromol. Chem. Phys.* **1996**, *197*, 1273.

[33] M. Danko, J. Mosnáček, *Polimery* **2017**, *62*, 272.

[34] A. Bhaw-Luximon, D. Jhurry, S. Motala-Timol, Y. Lochee, *Macromol. Symp.* **2005**, *231*, 60.

[35] M. Dionzou, A. Morère, C. Roux, B. Lonetti, J. D. Marty, C. Mingotaud, P. Joseph, D. Goudounèche, B. Payré, M. Léonettie, A.-F. Mingotaud, *Soft Matter.* **2016**, *12*, 2166.

[36] R. F. Domingos, M. A. Baalousha, Y. Ju-Nam, M. M. Reid, N. Tufenkji, J. R. Lead, G. G. Leppard, K. J. Wilkinson, *Environ. Sci. Technol.* **2009**, *43*, 7277.

[37] O. Sedlacek, B. D. Monnery, S. K. Filippov, R. Hoogenboom, M. Hruby, *Macromol. Rapid Commun.* **2012**, *33*, 1648.

[38] S. Agarwal, X. Xie, *Macromolecules* **2003**, *36*, 3545.

[39] A. Ianiro, J. Patterson, Á. González García, M. M. J. van Rijt, M. M. R. M. Hendrix, N. A. J. M. Sommerdijk, I. K. Voets, A. C. C. Esteves, R. Tuinier, *J. Polym. Sci., Part B: Polym. Phys.* **2018**, *56*, 330.

[40] S. Zolls, R. Tantipolphan, M. Wiggenhorn, G. Winter, W. Jiskoot, W. Friess, A. Hawe, *J. Pharm. Sci.* **2012**, *101*, 914.

[41] M. Ukawala, T. Rajyaguru, K. Chaudhari, A. S. Manjappa, S. Pimple, A. K. Babbar, R. Mathur, A. K. Mishra, R. S. Murthy, *Drug Delivery* **2012**, *19*, 155.

[42] Z. Zhang, Q. Qu, J. Li, S. Zhou, *Macromol. Biosci.* **2013**, *13*, 789.

[43] K. Kolouchova, O. Sedlacek, D. Jirak, D. Babuka, J. Blahut, J. Kotek, M. Vit, J. Trousil, R. Konefał, O. Janouskova, B. Podhorska, M. Slouf, M. Hruby, *Biomacromolecules* **2018**, *19*, 3515.

[44] P. Grossen, D. Witzigmann, S. Sieber, J. Huwyler, *J. Controlled Release* **2017**, *260*, 46.

[45] P. Grossen, G. Québatte, D. Witzigmann, C. Prescianotto-Baschong, L.-H. Dieu, J. Huwyler, *J. Nanomater.* **2016**, *2016*, 13.

[46] J. Jin, B. Sui, J. Gou, J. Liu, X. Tang, H. Xu, Y. Zhang, X. Jin, *PLoS One* **2014**, *9*, e112200.

[47] Y. Pei, Y. Yeo, *J. Controlled Release* **2016**, *240*, 202.

[48] S. M. Abaza, *Parasitol. United J.* **2016**, *9*, 1.

[49] I. Vainshtein, L. K. Roskos, J. Cheng, M. A. Sleeman, B. Wang, M. Liang, *Pharm. Res.* **2015**, *32*, 286.

[50] S. Behzadi, V. Serpooshan, W. Tao, M. A. Hamaly, M. Y. Alkawareek, E. C. Dreaden, D. Brown, A. M. Alkilany, O. C. Farokhzad, M. Mahmoudi, *Chem. Soc. Rev.* **2017**, *46*, 4218.

[51] M. J. Czaja, A. M. Cuervo, *Autophagy* **2009**, *5*, 866.

[52] M. E. Fox, F. C. Szoka, J. M. J. Fréchet, *Acc. Chem. Res.* **2009**, *42*, 1141.

[53] A. Orchel, K. Jelonek, J. Kasperczyk, Z. Dzierzewicz, *Acta Pol. Pharm.* **2010**, *67*, 710.

[54] S. Sadhukhan, G.-F. Zhang, G. P. Tochtrop, *ACS Chem. Biol.* **2014**, *9*, 1706.

Supporting Information

#-Butyrolactone Copolymerization with the Well-Documented Polymer Drug Carrier Poly(ethylene oxide)-*block*-poly(#-caprolactone) to Fine-Tune Its Biorelevant Properties

Tomáš Urbánek, Jií Trousil, Dmytro Rak, Kristýna Gunár, Rafa# Konefa#, Miroslav Šlouf, Marián Sedlák, Olga Šebestová Janoušková, and Martin Hrubý*

γ-Butyrolactone as a Comonomer into the Well-Documented Polymer Drug Carrier Poly(Ethylene Oxide)-*block*-Poly(ε-Caprolactone) to Fine-Tune Bio-Relevant Properties

Tomáš Urbánek[1], Jiří Trousil[1,2], Dmytro Rak[3], Kristýna Gunár[1], Rafał Konefał[1], Miroslav Šlouf[1], Marián Sedlák[3], Olga Šebestová Janoušková[1], Martin Hrubý[1]*

[1] Institute of Macromolecular Chemistry, Czech Academy of Sciences, Heyrovského náměstí 2, 162 00 Prague 6, Czechia

[2] Department of Analytical Chemistry, Charles University, Faculty of Science, Hlavova 8, 128 43 Prague 2, Czechia

[5] Institute of Experimental Physics, Slovak Academy of Sciences, Watsonova 47, 040 01 Košice, Slovakia

* Corresponding author: M.H. (mhruby@centrum.cz)

Characterization of N-(3,5-bistrifluoromethyl)phenyl N′-cyclohexylthiourea (TU) by ^{1}H NMR spectroscopy

^{1}H NMR (300 MHz, CDCl$_3$) δ 8.15 (s, 1H, H3), 7.70 (s, 2H, H1), 7.65 (s, 1H, H2), 6.03 (s, 1H, H4), 4.19 (s, 1H, H5), 1.98-2.04 (m, 2H, H6), 1.55-1.67 (m, 3H, H6), 1.29-1.41 (m, 2H, H6), 1.11-1.20 (m, 3H, H6).
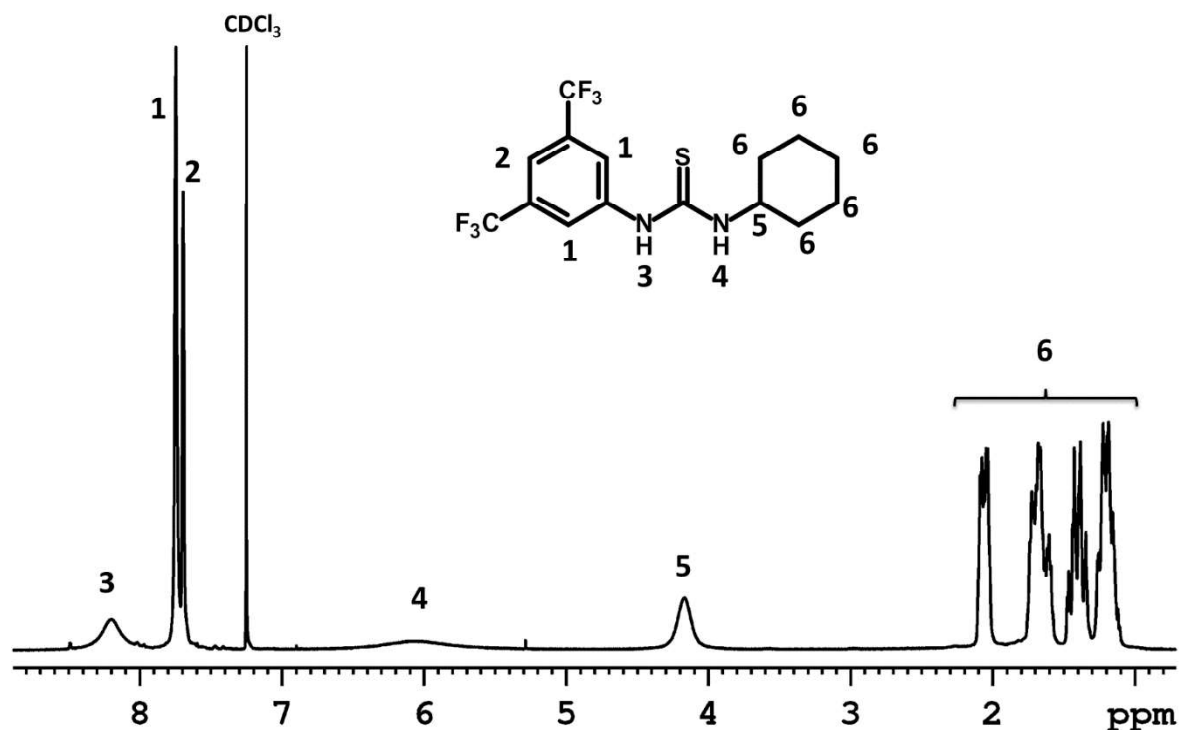
Figure S1 ^{1}H NMR spectrum of N-(3,5-bistrifluoromethyl)phenyl N′-cyclohexylthiourea (TU).

Characterization of PCL-*co*-P4HB by ^{1}H NMR spectroscopy

^{1}H NMR (600 MHz, CDCl$_3$) δ 7.30 (Ha), 5.07 (Hb), 4.04 (Hg, Hj), 3.59 (Hg' - the protons from of the methylene group on the end of the chain, next to the hydroxyl group), 2.33 (Hh), 2.25 (Hc), 1.91 (Hi), 1.59 (Hd, Hf), 1.33 (He).
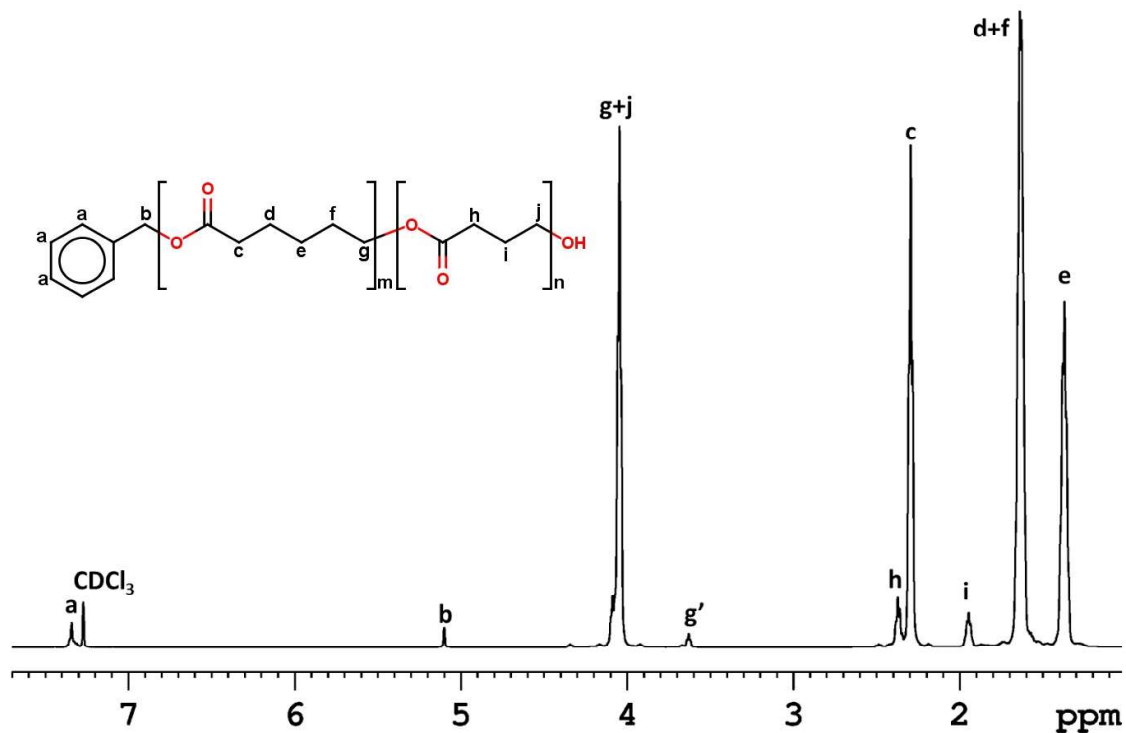
Figure S2 ^{1}H NMR spectrum of PCL-*co*-P4HB

Characterization of PCL-*co*-P4HB by FTIR

The ester bond was proved by FTIR with characteristic peaks for ester bond with maxima in 1720 cm^{-1}, 2866 cm^{-1} and 2944 cm^{-1}. The fingerprint regions were identical.
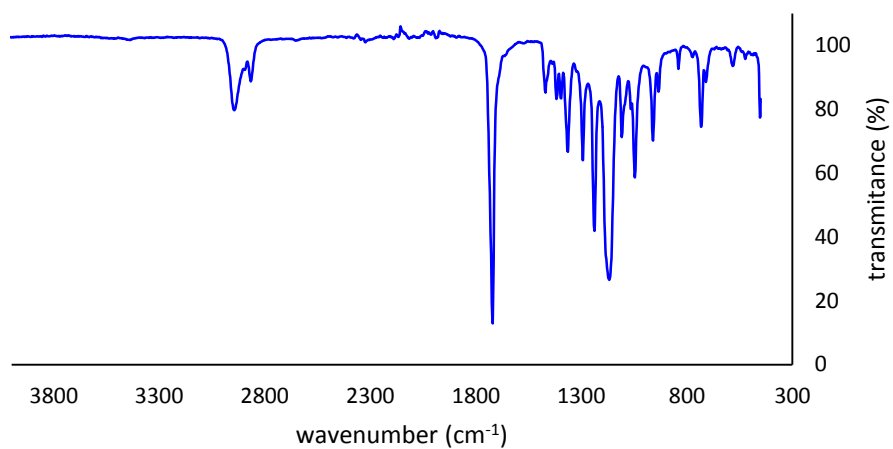
Figure S3 FTIR spectrum of PCL-*co*-P4HB

Copolymerization in NMR spectrometer and analyzing *in situ*

The copolymerization catalyzed by TBD and initiated by benzyl alcohol (BA) has been done in the same manner as the previous reactions, only deuterated DCM was used. The spectra have been taking during the copolymerization *in situ* periodically in time and the graph on **Figure 1D** have been ploted from these datas. The incorporation of εCL has been tracked by incresing of intensity of the peak *e* (δ 1.33 ppm) and incorporation of γBL by increasing of intensity of the peak *i* (δ 1.91) devided by the intensity of the peak *b* (δ 5.07 ppm). The intensity of peak *a*, assigned to initiator's benzene protons, was set as 5 and then the molar mass and the content of 4HB in polymer chain were calculated by the equations:

$$M_n = \left(\frac{I_e}{I_b} \cdot M_{\varepsilon CL}\right) + \left(\frac{I_i}{I_b} \cdot M_{\gamma BL}\right) + M_{BA} \tag{1}$$

$$f_{\gamma BL} = \frac{I_i}{I_e + I_i} \cdot 100\% \tag{2}$$
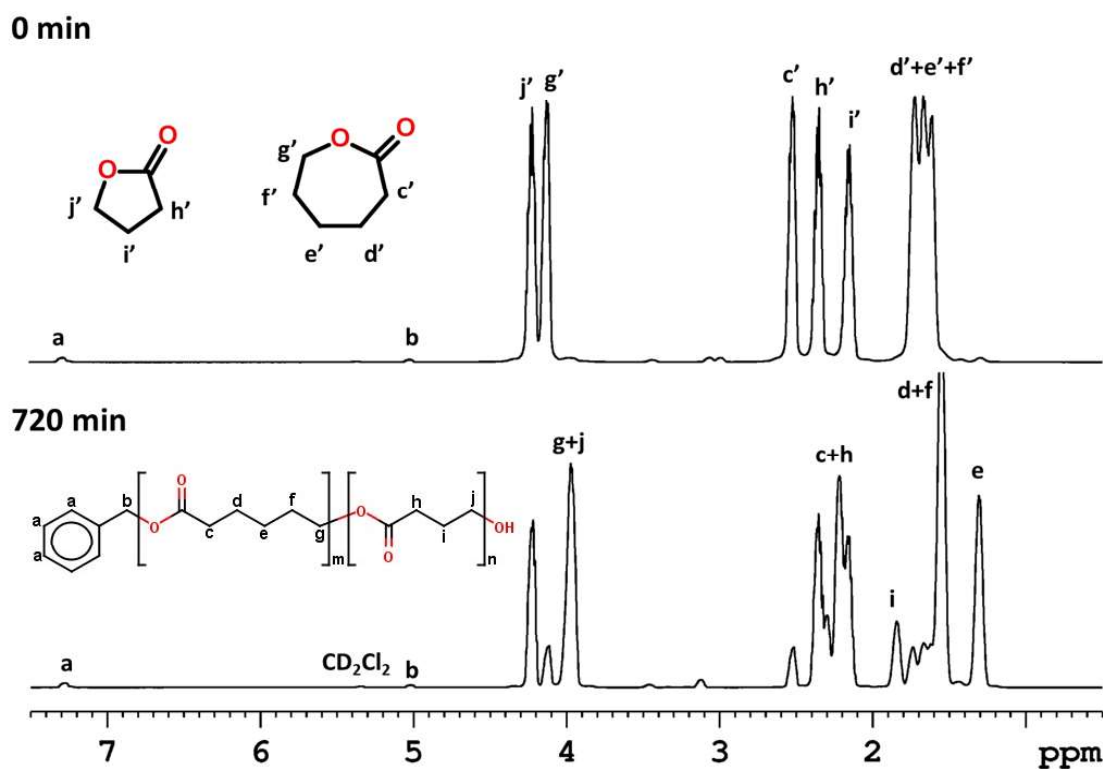
Figure S4 ^{1}H NMR spectra taken during copolymerization *in situ* in the beginning (0 min) and at the end (720 min)

Table S1 Polymerization conditons and composition of the copolymers initiated by benzyl alcohol with various feed ratios of the monomers. The TBD or HCl in diethylether (2M) was used as catalyst in DCM and initial monomers' concentration was 0.3 g/mL. [I]:[cat]:[εCL+γBL]=1:1:113.

Sample	Catalyst	Feed ratio of γBL (w%)	Yield (%)	fγBL (%)	M_n (NMR)	M_n (SEC)	Đ (SEC)
P1	HCl/Et$_2$O	0	84	0	12,100	13,100	1.14
P2		20	70	2	6,800	7,900	1.11
P3		30	61	3	7,700	6,400	1.11
P4		40	52	4	6,700	7,500	1.14
P5	TBD	0	90	0	11,300	13,300	1.36
P6		20	69	8	9,000	9,000	1.25
P7		30	60	11	8,700	7,600	1.31
P8		40	52	14	7,200	6,400	1.29

Table S2 Polymerization conditions and composition of the copolymers initiated by benzyl alcohol with the monomer-to-initiator ratio [I]:[cat.]:[εCL]:[γBL]=1:1:60:53 and the feed ratio of γBL=40 w%.

Sample	Catalyst	Solvent	Monomers' concentration[a]	Yield (%)	fγBL (%)	M_n (NMR)	M_n (SEC)	Đ (SEC)
A1	HCl/Et$_2$O	DCM	0.3	60	4	6,700	7,500	1.14
A2		DCM	0.5	60	6	10,700	8,600	1.24
A3		DCM	1	63	8	7,300	9,300	1.13
A4		DCM	2	62	10	8,500	9,500	1.22
A5		DCM	bulk*	64	13	11,300	10,900	1.28
A6	DPP	DCM	0.3	61	5	7,100	7,000	1.22
A7		DCM	0.5	60	8	8,800	8,800	1.22
A8		DCM	1	63	9	11,000	12,400	1.18
A9		DCM	2	62	11	9,700	10,200	1.19
A10		DCM	bulk*	66	13	9,400	8,900	1.32
A11	DBU/TU	DCM	0.3	0				
A12		DCM	0.5	0				
A13		DCM	1	0				
A14		DCM	2	0				
A15		DCM	bulk*	39	27	7,200	6,000	1.28
A16	TBD	DCM	0.3	60	14	7,700	9,000	1.29
A17		DCM	0.5	60	17	8,500	10,200	1.37
A18		DCM	1	63	23	11,100	12,600	1.51
A19		DCM	2	65	25	11,200	14,900	1.54
A20		DCM	bulk*	63	27	11,200	13,300	1.56
A21		toluene	1	64	28	11,400	13,700	1.42
A22		chlorobenzene	1	58	24	11,800	12,600	1.38
A23		THF	1	65	24	13,400	11,800	1.33
A24		acetonitrile	1	61	17	12,700	11,800	1.43

[a] Initial concentration of monomers in the reaction feed.
* Bulk copolymerization, no solvent was needed.

Table S3 Feed amounts for polymerization of mPEO-b-(PCL-co-P4HB)

	initiator	$m_{initiator}$ (mg)	m_{TBD} (mg)	M_{teor} (kDa)	$V_{\gamma BL}$ (mL)	$V_{\varepsilon CL}$ (mL)	V_{DCM} (mL)
B1	mPEO$_{45}$	200	14	10	0	0.78	0.5
B2	mPEO$_{45}$	200	14	6	0.14	0.23	0.5
B3	mPEO$_{45}$	200	14	10	0.28	0.47	0.5
B4	mPEO$_{114}$	200	6	10	0.12	0.07	0.5
B5	mPEO$_{114}$	200	6	20	0.21	0.35	0.5
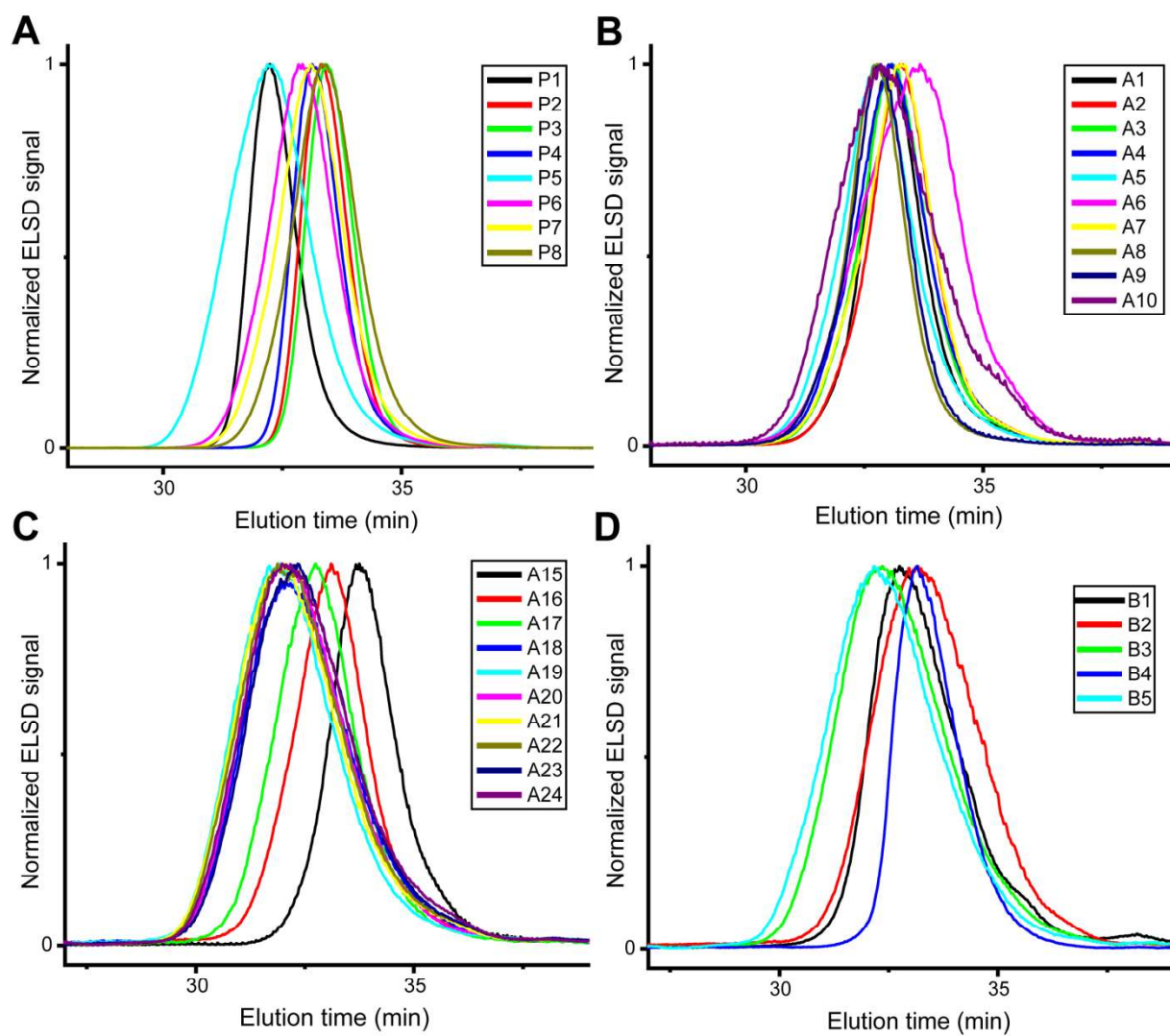
Figure S5 SEC curves of prepared copolymers (**A**) for samples **P1-P8**, (**B**) for samples **A1-A10**, (**C**) for samples **A15-A24** and (**D**) for samples **B1-B5**.
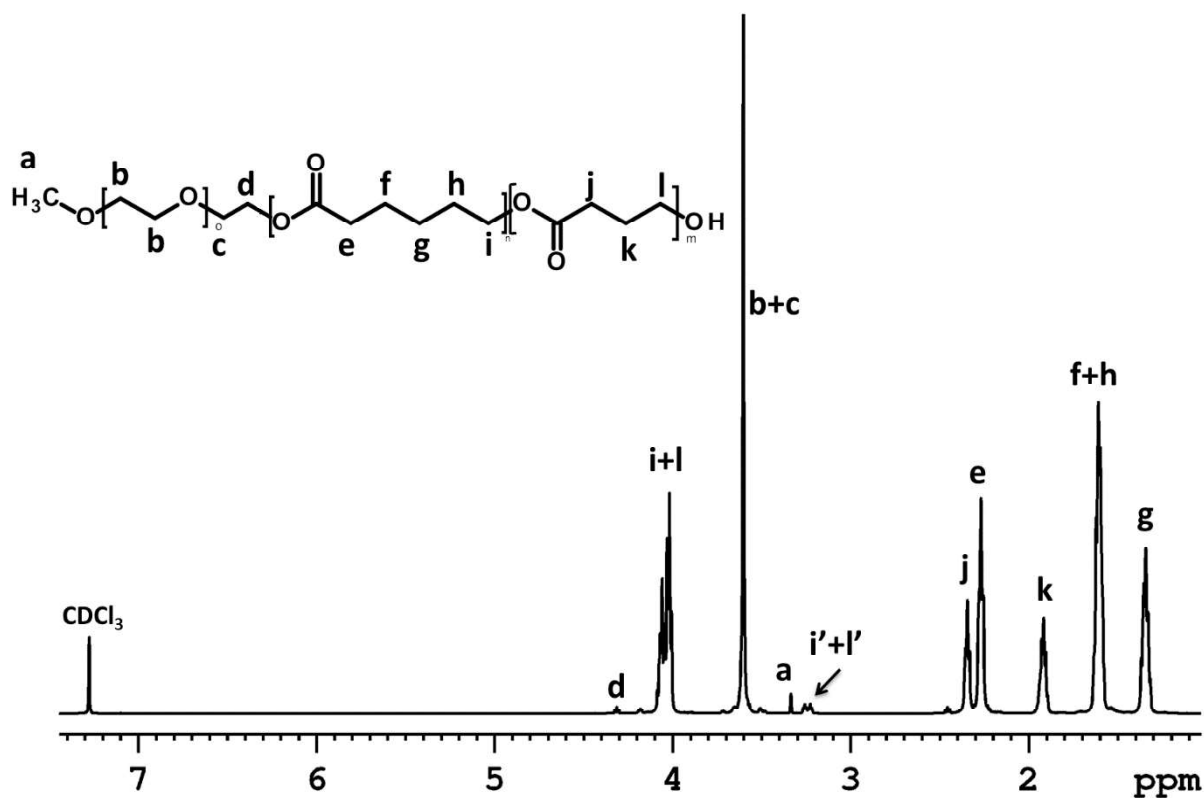
Figure S6 600 MHz ^{1}H NMR spectrum of PEG-*b*-(PCL-*co*-P4HB) measured in CDCl$_3$ at 25°C.
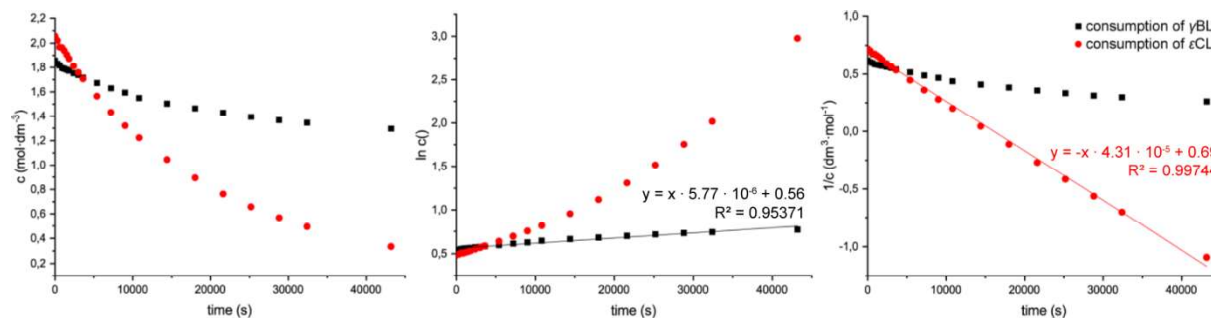
Figure S7 Consumption of γBL and εCL as (**A**) the concentration versus time, (**B**) the natural logarithm of concentration versus time and (**C**) the reverse value of concentration versus time, with highlighted linear regions and their

Critical aggregation concentration determination

The emmision of the samples was measured at the excitation wavelength of 560 nm. There are dependeces of relative intensities of fluorescence at 650 nm on concentration in logaritmic scale in **Figure S8**. Two regions in the graphs are apparent where the linear fitting has been done for each part and the intersection of the line was estimated as the critical aggregation concentration.
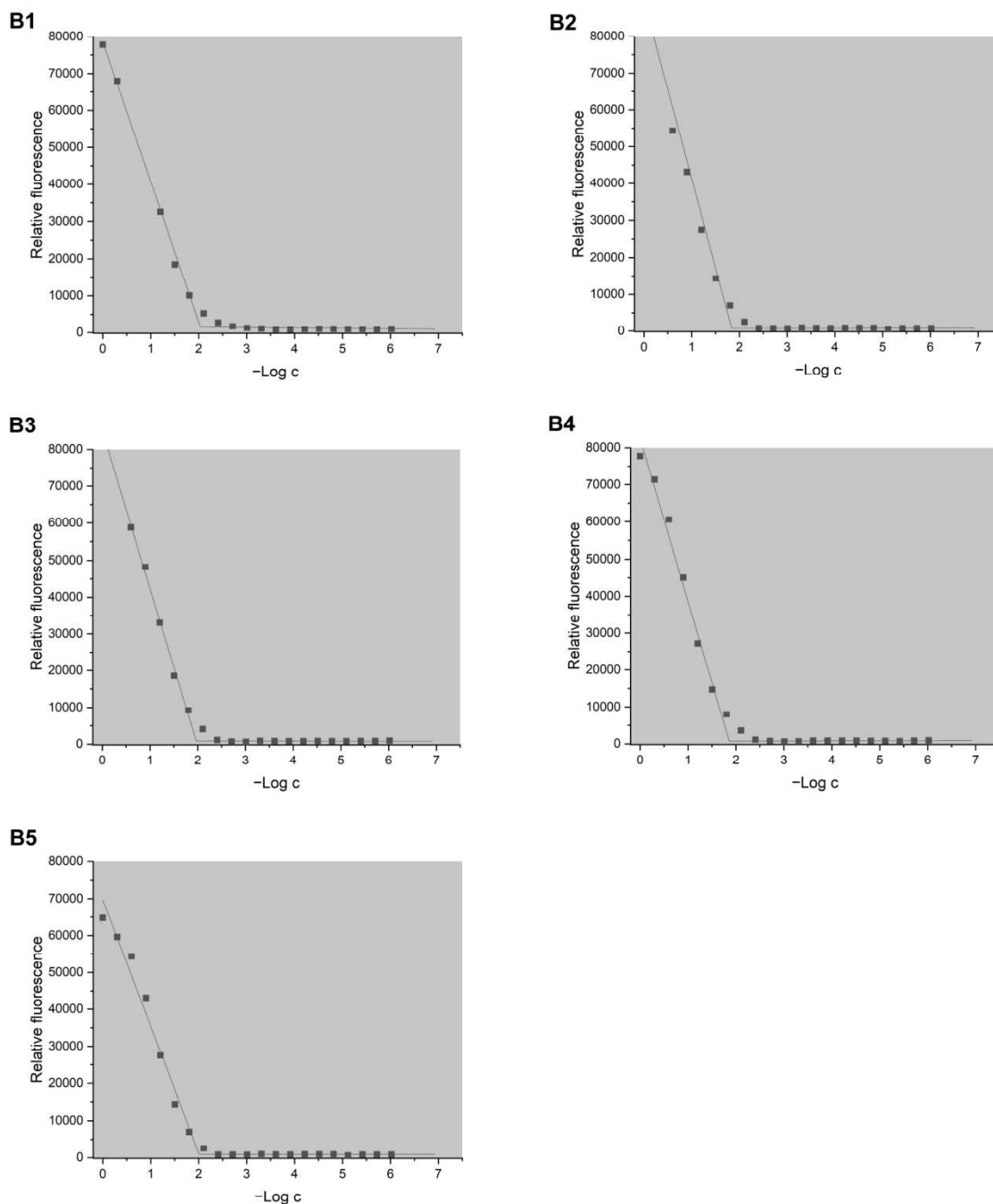
Figure S8 Critical aggregation concentration determination for samples **B1–B5**.
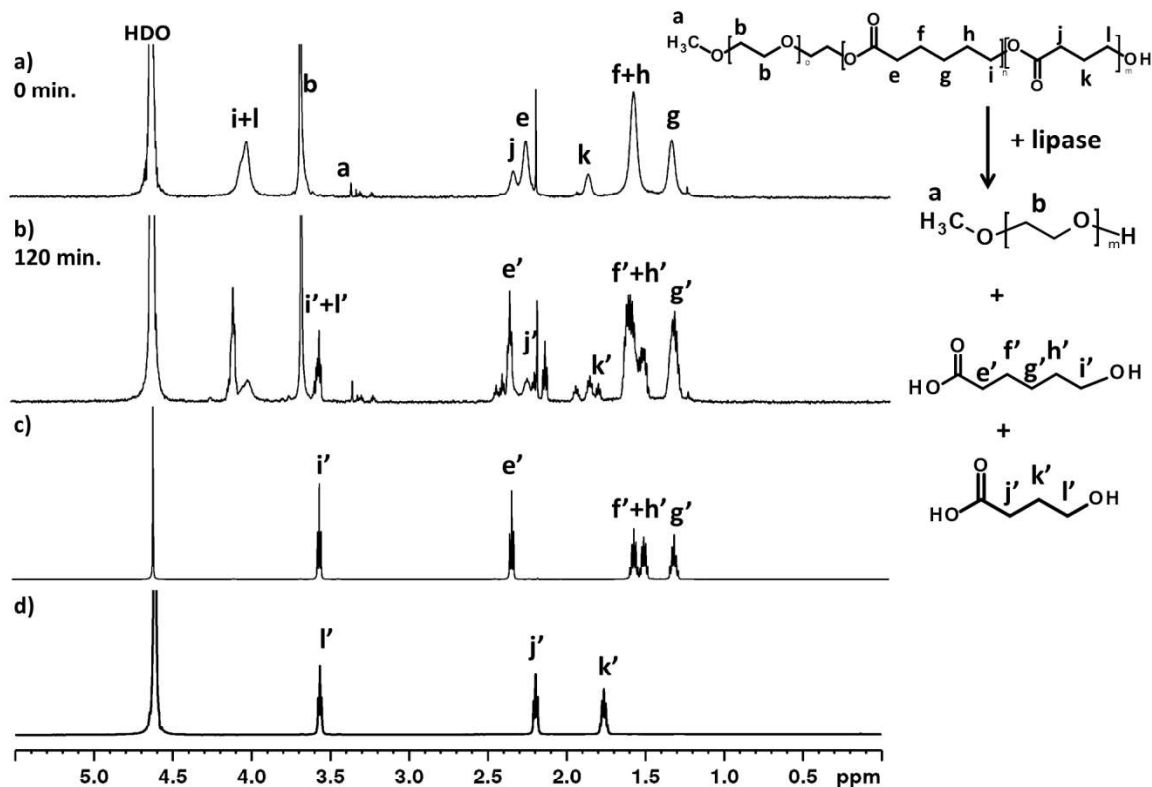
Figure S9 ^{1}H NMR spectra of NPs prepared from mPEO-*b*-PCL (**B1**) and mPEO-*b*-(PCL-*co*-P4HB) (**B2-B5**) measured in deuterated PBS at 37 °C before (**a**) and after (**b**) lipase addition. (**c**) 600MHz ^{1}H NMR spectrum of 6-hydroxyhexanoic acid measured in deuterated PBS at 37 °C. (**d**) ^{1}H NMR spectrum of 4-hydroxybutyric acid measured in deuterated PBS at 37 °C.
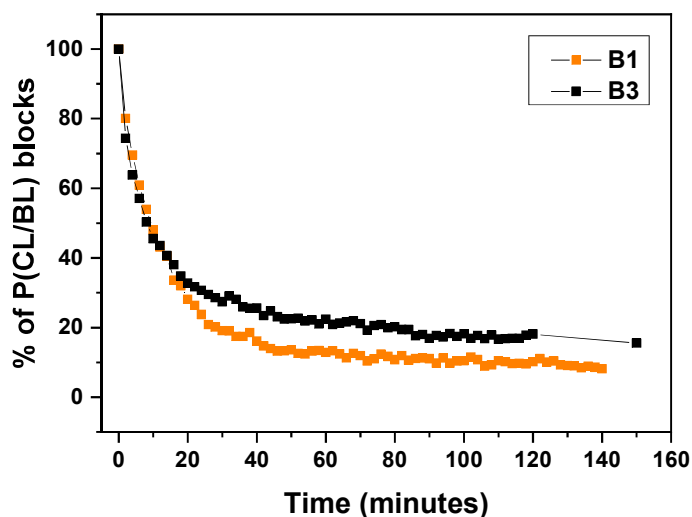
Figure S10 Enzymatic degradation of the NPs in presence of lipase from *Pseudomonas* sp. investigated by ^{1}H NMR, based on decrease of the intensity of the OCH_2 signal. Results related to the samples mPEO$_{44}$-*b*-PCL$_{81}$ (**B1**) and mPEO$_{45}$-*b*-(PCL$_{55}$-*co*-P4HB$_{19}$) (**B3**) are shown.
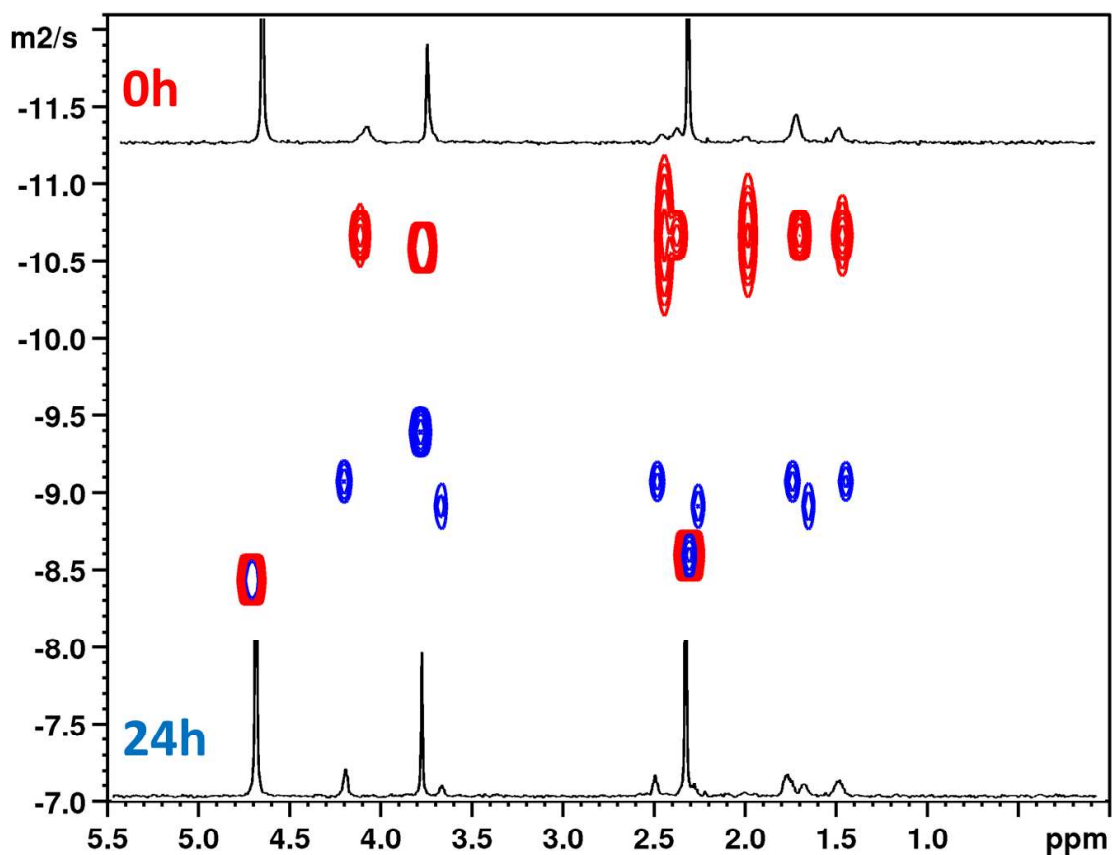
Figure 11 MHz 1H 2D DOSY NMR spectra of NPs prepared from mPEO-b-(PCL-co-P4HB) (B2-B5) measured in deuterated PBS at 37 °C before (**red**) and after (**blue**) lipase addition.

Fluorescent labelling of mPEO-*b*-(PLC-*co*-P4HB) with DACCA
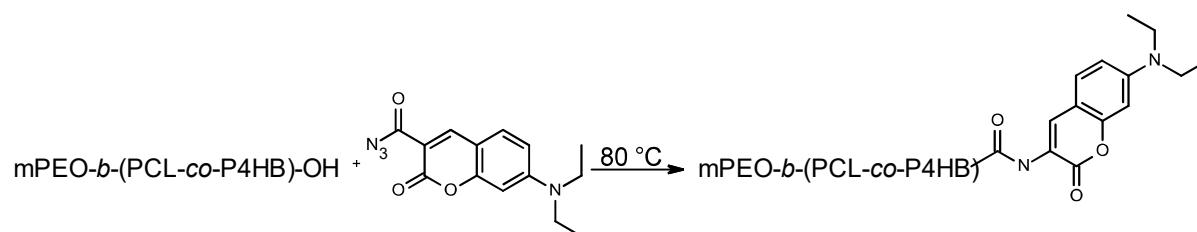
Figure S12 Scheme of fluorescent dye labelling.
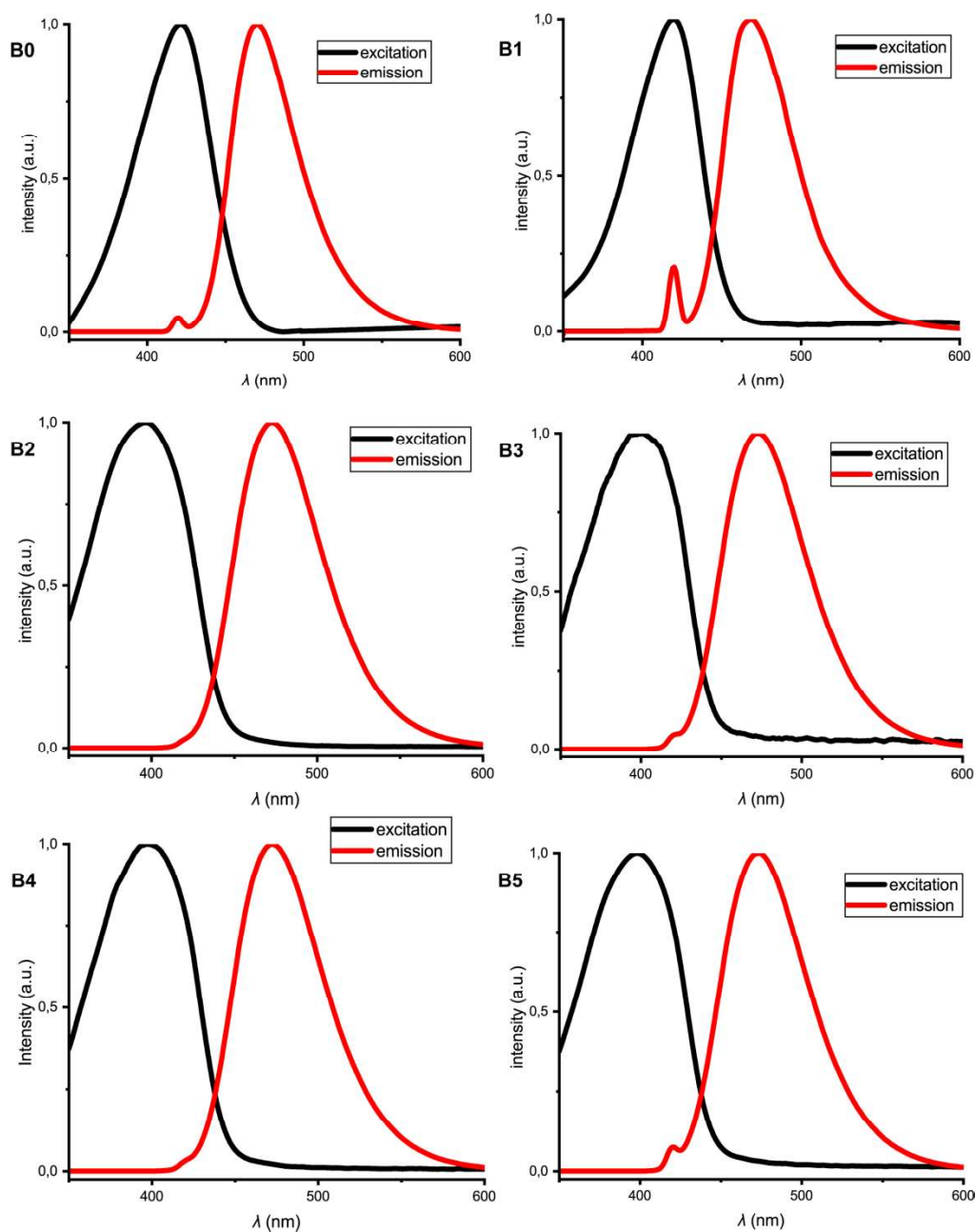
Figure S13 Excitation and emission spectra of free 7-(diethylamino)coumarin-3-carboxylic acid (**B0**) and 7-(diethylamino)coumarin-3-carbonyl azide (DACCA)-labelled samples **B1–B5**.
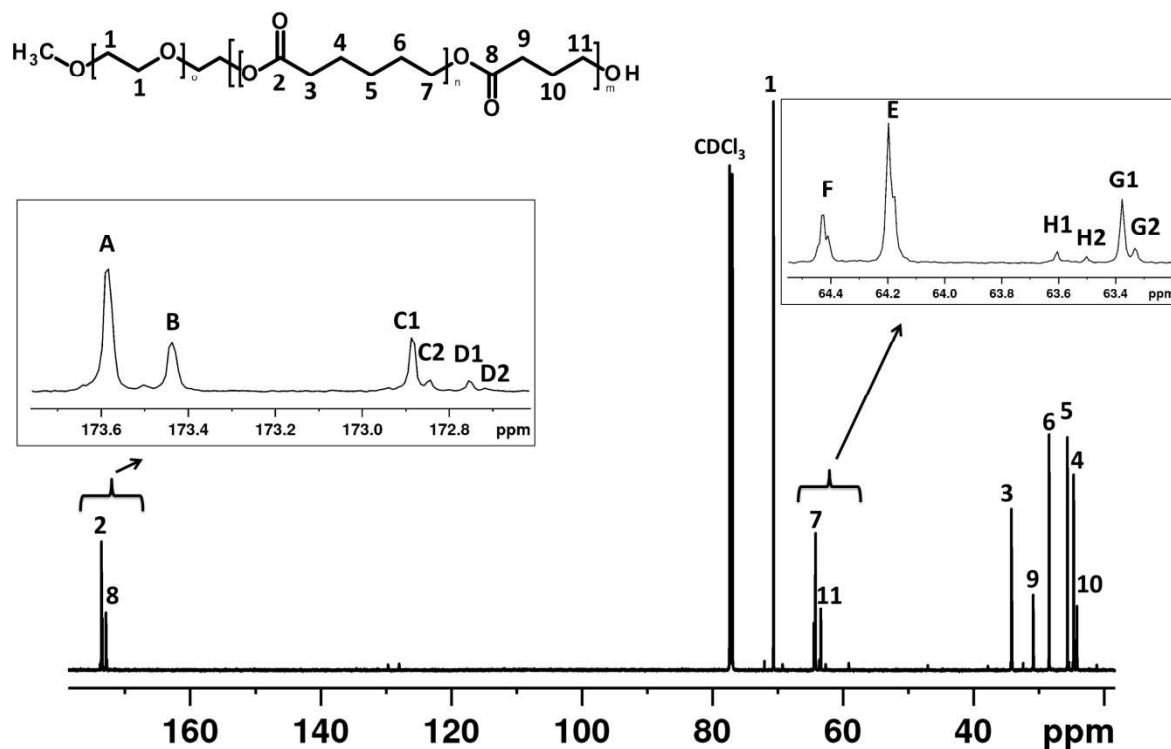
Figure S14 ^{13}C spectrum of mPEO-*b*-(PCL-*co*-P4HB) measured in CDCl₃ at 25°C. Enlarged areas shows carbonyl carbon region (A= CL<u>CL</u>CL + CL<u>CL</u>BL; B= BL<u>CL</u>CL + BL<u>CL</u>BL; C1= CL<u>BL</u>CL; C2= CL<u>BL</u>BL; D1= BL<u>BL</u>CL; D2= BL<u>BL</u>BL) and the methylene carbon region (E= CL<u>CL</u>CL + BL<u>CL</u>CL; F= CL<u>CL</u>BL + BL<u>CL</u>BL; G1= CL<u>BL</u>CL; G2= BL<u>BL</u>CL; H1= CL<u>BL</u>BL; H2= BL<u>BL</u>BL) triads.

To characterize macromolecular structure of copolymer polyester block we calculated from peak areas of the respective NMR signals of methylene carbon region. To simplify calculations integral intensity of signals of the diad diffractions $f_{CL,CL}$ (E), $f_{BL,BL}$ (H1 + H2), $f_{CL,BL}$ (F), and $f_{BL,CL}$ (G1 + G2) equals: 0.5106; 0.0692; 0.2054 and 0.2147 respectively, were used. The molar composition was obtained also from integral intensity of relative signals:

$$P_{CL} = \frac{f_{CL,BL} + f_{BL,CL}}{2} + f_{CL,CL} \qquad P_{BL} = \frac{f_{CL,BL} + f_{BL,CL}}{2} + f_{BL,BL}$$

The calculated molar fractions were: P_{CL}=0.721 and P_{BL}=0.279. The probabilities $P_{BL,CL}$ = 0.75 (or $P_{CL,BL}$ = 0.29) of appearance CL (or BL) unit after BL (or CL) unit is given by equations:

$$P_{CL,BL} = \frac{f_{CL,BL} + f_{BL,CL}}{2P_{CL}} \qquad P_{BL,CL} = \frac{f_{CL,BL} + f_{BL,CL}}{2P_{BL}}$$

The number average sequence length (block length) L_{ni} of the CL and BL units (3.45 and 1.33 respectively) was calculated from:

$$L_{nCL} = \frac{1}{P_{CL,BL}} \qquad L_{nBL} = \frac{1}{P_{BL,CL}}$$

The degree of randomness (B = 1.04) is defined as the sum of the probabilities $P_{BL,CL}$ and $P_{CL,BL}$:

$$B = P_{BL,CL} + P_{CL,BL}$$

The number average sequence length (L_{ni}) represents the change in sequence distribution; L_{ni}=1 (alternating copolymer), while $L_{ni} = \infty$ (homopolymer). The degree of randomness (B) describes a copolymer composition (B=1 $-$ random distribution of copolymer chain, B=0 $-$ homopolymer chain).
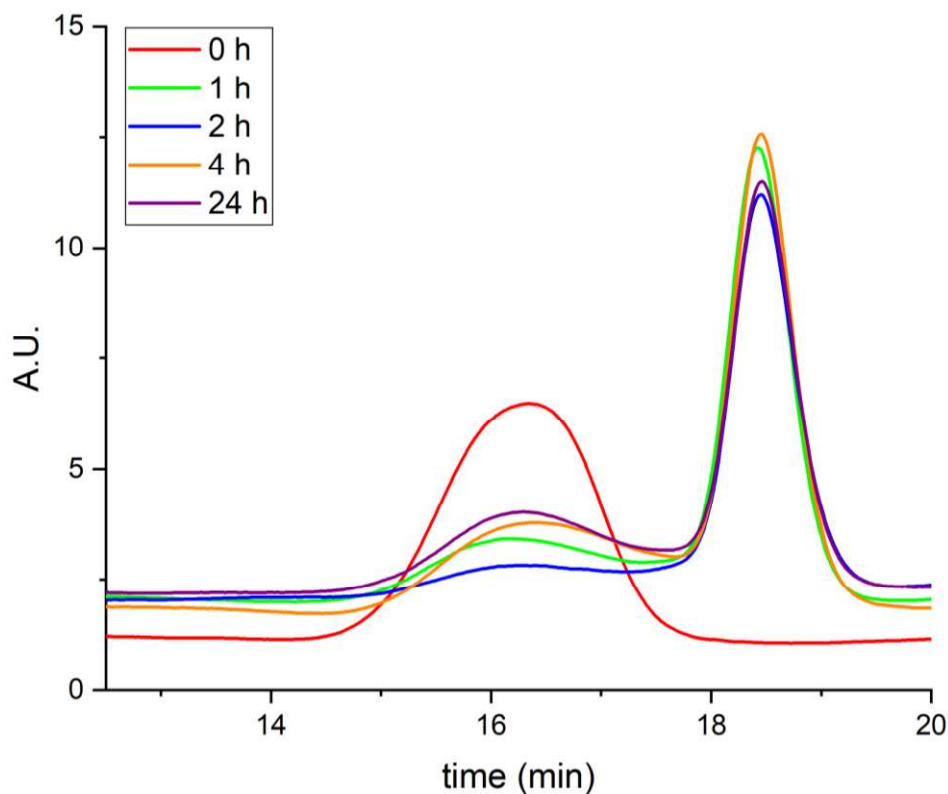
Figure S15 SEC chromatograms of sample **B2** captured in different times of the degradation process.

Appendix 3

Trousil, J.; Matějková, J.; Dai, YS.; Urbánek, T.; Šlouf, M.; Škorič, M.; Nejedlý, T.; Hrubý, M.; Fang, JY. Nanocrystalline chloroxine possesses broad-spectrum antimicrobial activities and excellent skin tolerability in mice. *Nanomedicine (Lond)* **2022**, 17 (3), 137. IF = 5.307

Nanocrystalline chloroxine possesses broad-spectrum antimicrobial activities and excellent skin tolerability in mice

Jiří Trousil*,‡,1 [ID], Jana Matějková‡,2,3 [ID], You-Shan Dai4, Tomáš Urbánek1 [ID], Miroslav Šlouf1 [ID], Miša Škorič5, Tomáš Nejedlý1, Martin Hrubý1 & Jia-You Fang4

1Institute of Macromolecular Chemistry, Czech Academy of Sciences, Heyrovského nám. 2, 162 00 Prague 6, Czechia
2Department of Medical Microbiology, Second Faculty of Medicine, Charles University and Motol University Hospital, V Úvalu 84, 150 06 Prague 5, Czechia
3Military Health Institute, Military Medical Agency, Tychonova 1, 160 00 Prague 6, Czechia
4Pharmaceutics Laboratory, Graduate Institute of Natural Products, Chang Gung University, Taoyuan 333, Taiwan
5Department of Pathological Morphology and Parasitology, Faculty of Veterinary Medicine, University of Veterinary Sciences Brno, Palackého tř. 1946/1, 612 42 Brno, Czechia
*Author for correspondence: trousil@imc.cas.cz
‡Authors contributed equally

Background: Antimicrobial submicrometer particles are being studied as promising interventions against a wide range of skin conditions, such as fungal or bacterial infections. **Aims:** To submicronize chloroxine, the crystalline compound 5,7-dichloro-8-hydroxyquinoline, by nanoprecipitation and characterize the resulting assemblies. **Methods:** The chloroxine particles were stabilized by a nonionic surfactant and were studied by a broth microdilution assay against 20 medically important bacteria and fungi. The intervention was studied using a murine model of skin irritation. **Results & conclusions:** Chloroxine nanoparticles with a diameter of 600–800 nm exhibit good tolerability in terms of skin irritation *in vivo* and good antimicrobial activity. Thus, the fabricated formulation shows great promise for interventions for both cutaneous infection control and prophylaxis.

Graphical abstract:
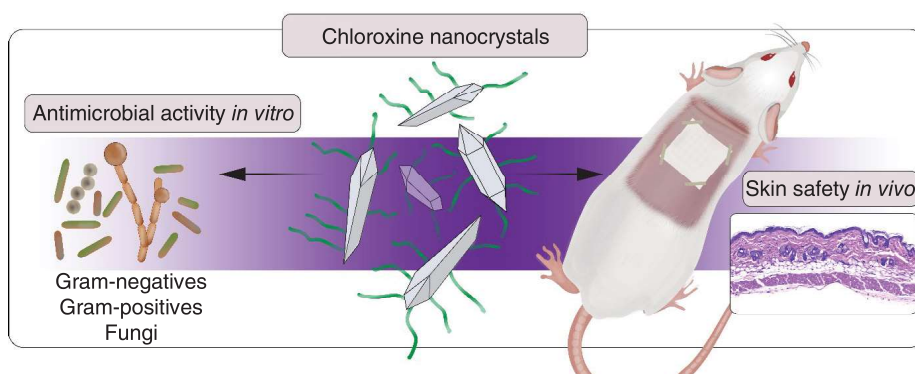
Chloroxine nanocrystals
Antimicrobial activity *in vitro*
Gram-negatives
Gram-positives
Fungi
Skin safety *in vivo*

The skin is the largest organ of the body. It possesses many functions, including immunologic and sensorial. Also, it acts as a critical barrier for protection and moisture control [1,2]. Due to the increasing incidence of injuries, surgery, burns and chronic diseases (e.g., diabetes), the prevalence of wounds and skin infections continues to be a major health problem on a global scale [3]. Due to skin damage, the skin mechanisms are lost and microorganisms can easily infect the wounded site and may cause an infection or septicemia if the pathogens infiltrate the body.

Future Medicine

Indeed, considerable achievement has been made by using antibiotic and chemotherapeutic agents that have been very successful against bacteria and fungi. It is, however, important to stress that the rates of multichemotherapeutic resistance among these microorganisms keep increasing [4–6]. Accordingly, innovative technologies and interventions are desperately needed for the control of such infections.

Nanotechnology offers attractive opportunities to avoid the pharmaceutical shortcomings of most active pharmaceutical ingredients (APIs) [7]. In the context of skin infections, the study of antibacterial, nanobead-based interventions is an emerging field, as beads with a mean size in the nanometer range possess antibacterial activities that allow for dosage reductions, minimize undesirable side effects and enhance their antimicrobial activities [8]. Several recent works studied metal nanoparticles, for instance. Permana and co-workers explored silver nanoparticles as antibiofilm agents against *Staphylococcus aureus* and *Pseudomonas aeruginosa* biofilms [9]. The particles were incorporated into bacteria-responsive microparticles based on poly (ε-caprolactone) decorated with chitosan. In rat skin, this approach led to bacterial bioburden eradication *ex vivo*. Addressing therapy of chronic wounds, Ahmadi and Adibhesami explored *P. aeruginosa*-treating silver nanoparticles in combination with tetracycline *in vivo* [4]. Among silver nanoparticles, gold nanoparticles are particularly attractive, as well. The Xia group synthesized antibacterial photodynamic gold nanoparticles, which were self-assembled nanocomposites of an antibacterial photodynamic peptide and poly(ethylene glycol)-stabilized nanoparticles [10]. The studied interventions exhibited stability, a satisfactory generation of reactive oxygen species and an antibacterial effect toward both *S. aureus* and *Escherichia coli*. Considerable attention has been given to soft nanomaterials. For example, lipid nanoparticles against *S. aureus* were studied by Walduck and co-workers [11]. *In vivo*, rifampicin-loaded lipid nanoparticles could successfully treat methicillin-resistant *S. aureus* (MRSA) infection at a reduced antibiotic dosage compared with the free rifampicin in a skin wound model. Similarly, nanomedicines have been suggested for use against cutaneous infections caused by fungi [12–14]. Recently, Mumtaz and coworkers studied polymeric nanoparticles loaded with voriconazole, a second-generation triazole antifungal drug, to enhance the topical delivery in the form of film-forming spray [15]. The nanoparticles were prepared through ionic gelation and were found to be active against *Candida albicans* and *Aspergillus flavus*. Importantly, the interventions exhibited good tolerability in terms of skin irritation *in vivo*. Overall, it has been suggested that antimicrobial drug delivery might overcome the limitations of conventional drugs.

Through the formulation of APIs as submicron crystals, in recent decades, nanomedicine-focused research has been approaching this issue. These interventions, defined as carrier-free submicron colloidal drug-delivery systems (with sizes typically ranging from 10 to 800 nm), include pure drugs and a minimum of surface-active compounds required for the stabilization of such formulations, for instance [16]. In this work, the authors studied chloroxine (CAS Reg. no. 773–76–2, chemically 5,7-dichloro-8-hydroxyquinoline). It is an important 8-hydroxyquinoline derivative; it is known to possess antiprotozoal, fungistatic and bacteriostatic activities [17]. Recently, its antimicrobial activities against MRSA [18], *Geomyces destructans* [19], pathogenic *Burkholderia* [20] and emerging molds [20] have been investigated. In these studies, its low water solubility, however, complicated the preclinical study and limited the formulation in dimethyl sulfoxide solutions. Also, this solubility issue limits its clinical use in orally administered interventions against intestinal amebiasis and topical shampoos against dandruff and seborrheic dermatitis of the scalp [21]. No information on possible chloroxine submicronization that could lead to stable nanoparticle-based formulations is, however, available.

The authors' research collective has a particular interest in a comprehensive study of antimicrobial nanoparticles. Given this motivation and the background outlined above, the authors propose the use of the approved drug chloroxine for the fabrication of submicron particles stabilized by a biocompatible surfactant to obtain a stable colloidal formulation as a potential antimicrobial intervention. These chloroxine nanoparticles (CXNPs) were formed through self-assembly in aqueous media. Next, their physicochemical properties were explored by dynamic light scattering (DLS), as well as their antimicrobial activities against several medically important microorganisms. The skin safety of the fabricated CXNPs was evaluated in mice *in vivo*. To the authors' knowledge, this is the first report on chloroxine submicronization and first study of its biological properties.

Materials & methods
Ethics statement
The animal study was conducted with approval from the Institutional Animal Care and Use Committee of Chang Gung University.
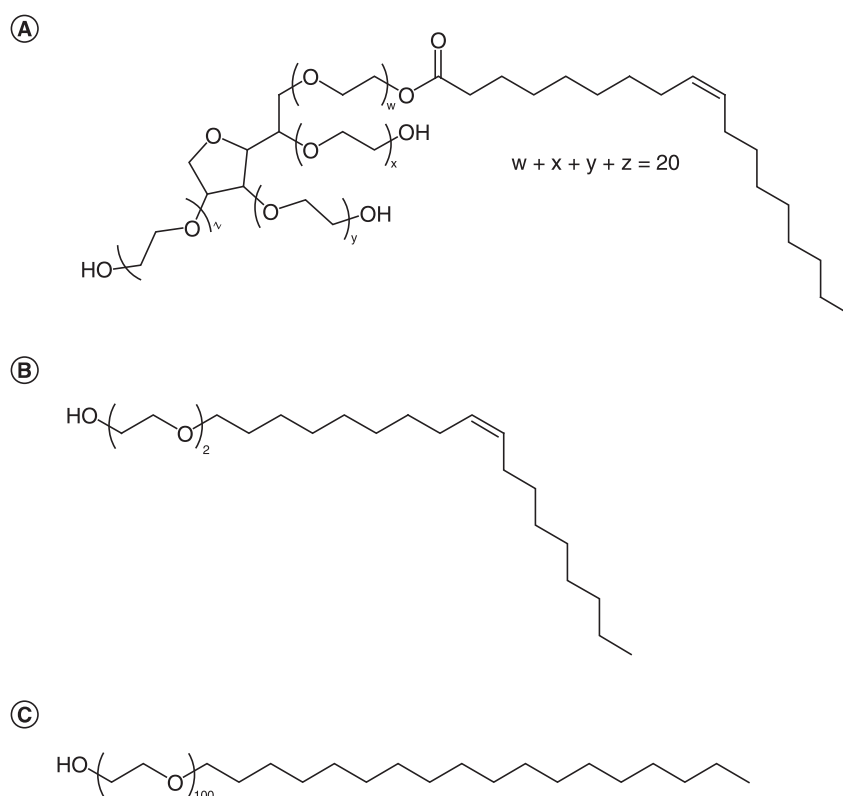
Figure 1.   Chemical structures of the nonionic surfactants used. (A) Tween 80, **(B)** Brij 92 and **(C)** Brij 700.

Materials

5,7-Dichloro-8-chinolinol (chloroxine, 99%), Brij 700, Brij 92, glycerol, oleic acid, ox-bile, Roswell Park Memorial Institute (RPMI) medium 1640, Tween 40 and Tween 80 were purchased from Sigma-Aldrich Ltd (Prague, Czechia). Ethanol (99.8%) was purchased from Lach-Ner Ltd (Neratovice, Czechia). Malt extract and peptone ex soya (papain digested) were purchased from Carl Roth Gmbh & Co. (Karlsruhe, Germany). Chocolate blood agar and Sabouraud dextrose agar plates were purchased from LabMediaServis Ltd (Jaroměř, Czechia). Mueller–Hinton broth base was purchased from Becton Dickinson Czechia Ltd (Prague, Czechia). Dulbecco's modified Eagle's medium (DMEM, Gibco™, Invitrogen, MA, USA) , purchased as both powder and liquid media; heat-inactivated fetal bovine serum (FBS, Gibco); penicillin-streptomycin solution (Gibco); PrestoBlue™ Cell Viability Reagent; and TrypLE™ Express Enzyme (Gibco) were supplied by Life Technologies Ltd (Prague, Czechia).

CXNP preparation

CXNPs were prepared by the nanoprecipitation method. For this purpose, a chloroxine solution in ethanol (500 μl, 2 mg/ml) was rapidly added to 10 ml aqueous media (i.e., water or surfactant solution) with continuous stirring (600 r.p.m.). The excess ethanol was evaporated *in vacuo* (40°C) after 1 min of stirring. The final concentration of CXNPs was 100 μg/ml. If surfactants (see the structures in Figure 1) were added to the aqueous medium, their content was set as 20, 40, 60 and 80% of the critical micellar concentration (CMC). For this, Tween 80 (CMC 13 μg/ml), Brij 92 (CMC 27 μg/ml) and Brij 700 (CMC 93 μg/ml) were used, and the resulting samples were referred to according to the surfactant used (namely, TW80, BR92 and BR700) and the surfactant percentage in the aqueous media used (e.g., BR700/80).

Nanoparticle characterization

The prepared samples were studied by DLS using a ZetaSizerNano-ZS ZEN3600 (Malvern Instruments Ltd, Malvern, UK) at an angle of 173°. A He-Ne 4.0 mW laser, operating at 633 nm, was used. The data were processed using Zetasizer Software, 7.10 (Malvern Instruments Ltd). The mean positions of the peaks within the intensity-hydrodynamic diameter (D_h) distributions were used to represent the data. The D_h of the particles was

calculated from the diffusion coefficient D using the Stokes–Einstein equation, $D = k_B T/3\mu\eta D_h$, where T is the absolute temperature, η is the viscosity of the solvent and k_B is the Boltzmann constant. The measurement of the zeta potential (electrophoretic light scattering) was performed using the same instrument. The electrophoretic mobility was mathematically transformed to zeta potential by the Smoluchowski approximation.

The morphology of the nanoparticles was visualized by transmission electron microscopy (TEM) using a Tecnai G2 Spirit Twin (Thermo Fisher Scientific Brno Ltd, Brno, Czech Republic). A drop of the sample formulation (2 μl) was deposited on a standard copper TEM grid coated with a carbon nanolayer and left to equilibrate for 1 min. Then, the excess solvent was removed by touching the bottom of the TEM grid with a piece of filter paper. This procedure (which the authors call the fast drying method) was found to be very useful for nanoparticle suspension systems, because it prevents oversaturation and minimizes drying artifacts [22,23]. The TEM grids were allowed to dry properly at room temperature for 1 h before measurement. The nanoparticles were observed at an accelerating voltage of 120 kV using standard bright field imaging mode.

Bacteria & fungi

Acinetobacter baumannii (CCM 2355), *Bordetella bronchiseptica* (CCM 6082), *Corynebacterium pseudodiphtheriticum* (CCM 2821), *Cronobacter sakazakii* (CCM 1902), *Enterobacter cloacae* (CCM 8574), *Escherichia coli* (CCM 3954), *Klebsiella oxytoca* (CCM 1901), *Klebsiella pneumoniae* subsp. *pneumoniae* (CCM 7798), *Moraxella catarrhalis* (CCM 2828), *Pseudomonas aeruginosa* (CCM 1960), *Shigella flexneri* (CCM 4422), *Staphylococcus aureus* subsp. *aureus* (ATCC 33591 and CCM 4223), *Staphylococcus epidermidis* (CCM 2124) and *Streptococcus pyogenes* (CCM 7418) were grown on chocolate blood agar at 37°C for 18–24 h. *Serratia marcescens* (CCM 303) was grown on chocolate-blood agar at 30°C for 18–24 h. *Candida albicans* (CCM 8261 and CCM 8215) was grown on Sabouraud dextrose agar at 30°C for 18–24 h. *Malassezia furfur* (DSM 6170) and *M. pachydermatis* (DSM 6172) were grown on modified Dixon agar (malt extract 36 g, peptone 6 g, ox bile 20 g, Tween 40 10 ml, glycerol 2 ml, oleic acid 2 ml and agar 12 g per liter [24]) at 32°C for 4–5 days.

Microdilution assay

Both the MIC and the minimum bactericidal concentration (MBC) values were estimated by broth microdilution assays. With a 96-well plate, the CXNPs were serially diluted twofold with deionized water supplemented with Brij700 (74 μg/ml, 80% CMC) at concentrations ranging from 100 to 0.10 μg/ml. Double-concentrated Mueller–Hinton broth, RPMI 1640 medium (*Can. albicans*) or modified RPMI 1640 medium (*Malassezia* spp.) was added to each well after inoculation, resulting in a final concentration ranging from 50 to 0.05 μg/ml and a final inoculum concentration of 1×10^5 colony-forming units (CFUs)/ml. The MIC values were determined as the lowest concentration of the compound that inhibited bacterial growth. After MIC determination, aliquots of 10 μl from wells that showed no growth were incubated on chocolate blood agar, Sabouraud dextrose agar or modified Dixon agar as appropriate. The MBC end point was defined as the lowest concentration of CXNPs that killed 100% of the initial bacterial population. The RPMI 1640 medium used for *Can. albicans* was supplemented with glucose at a final concentration of 2%. *Malassezia* spp. was cultured using RPMI 1640 medium that was supplemented as follows: 2% glucose, 1% peptone, 0.5% ox bile, 0.5% malt extract, 1% glycerol, 0.5% Tween 40 and 0.05% Tween 80 [25].

Cell culture

The HaCaT cell line, an immortalized keratinocyte cell line established from adult human skin, and human epidermoid carcinoma A431, both supplied by Cell Lines Service GmbH (Eppelheim, Germany), were grown in complete DMEM containing 10% FBS, 100 U/ml penicillin and 100 μg/ml streptomycin in a humidified atmosphere containing 5% CO_2 at 37°C. TrypLE™ Express Enzyme was used as the detaching reagent.

Cytotoxicity assay

The cells were seeded in 96-well plates at a density of 8,000 cells/well for both A431 and HaCaT cells. After overnight incubation at 37°C in 5% CO_2, the medium was replaced with 100 μl of DMEM containing the formulations to be tested. For this purpose, the CXNPs were serially diluted twofold with deionized water supplemented with Brij 700 (74 μg/ml). Double-concentrated DMEM (prepared and filter-sterilized from DMEM powder, 20% FBS) was added to each sample, resulting in a final concentration range of 50 to 0.4 μg/ml. After 24, 48 or 72 h of incubation, the medium was aspirated, and the cells were incubated with 110 μl of DMEM containing 10%
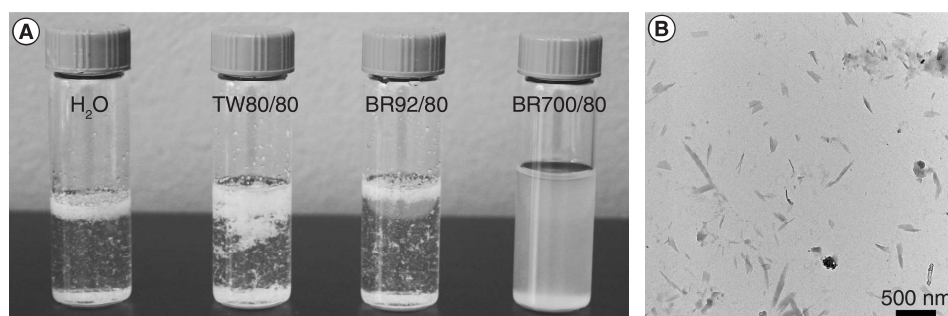
Figure 2.   Chloroxine nanocrystals. (A) Formulations based on different aqueous media: water, Tween 80, Brij 92 and Brij 700. **(B)** Ultrastructural analysis of the BR700/80-based nanoformulation; transmission electron micrograph is shown.

PrestoBlue™ Cell Viability Reagent. After 4 h, a Synergy H1 Hybrid Reader instrument (Biotek, VT, USA) was used to assess cell viability through fluorescence measurement according to the manufacturer's instructions. The results were expressed as a percentage of the control value (obtained from cells in the control medium), which was considered to be 100%. According to ISO 10993–5, a reduction in cell viability by more than 30% is considered a cytotoxic effect.

In vivo skin irritation

To assess the chloroxine formulation effect on mouse skin, the authors examined whether the CXNPs induced skin irritation. For this, BALB/c mice were randomly divided into four groups (n = 5) and prepared by shaving the dorsal fur; 100 µl of each formulation to be tested was spread over a nonwoven polyethylene cloth (1 × 1 cm) that was fixed on the mouse's back using a Tegaderm™ (3M, MN, USA) and Fixomull® stretch adhesive tape (BSN Medical Ltd, Willerby, UK). Sham control (Brij 700, 74 µg/ml) and CXNPs at two different concentrations (namely, 25 and 50 µg/ml, herein referred to as CXNPs 25 and CXNPs 50, respectively) were assessed. The formulations were administered once per day for 7 consecutive days. The skin condition was inspected daily via transepidermal water loss (TEWL) measurement (TM300, Courage & Khazaka, Köln, Germany), pH (Skin-pH-Meter® PH 905, Courage & Khazaka) and erythema (a*) using a CD100 colorimeter (Yokogawa Meters & Instruments Corp., Tokyo, Japan). On day 8, the mice were sacrificed and the dorsal skin was excised for histopathological examination (hematoxylin and eosin, H&E, staining). Nontreated mice served as the control group [26–28].

Results
Nanoparticle preparation optimization & further characterization

The authors studied chloroxine nanoprecipitation using different aqueous media. The use of water, Tween 80 and Brij 92 did not lead to satisfactory formulations, and a gross precipitate was formed (Figure 2A). Despite this fact, the supernatants of these formulations contained colloidal particles of chloroxine, as found by DLS measurements after centrifugation (1500 r.p.m., 5 min). The data obtained are listed in Table 1. This preliminary testing revealed D_h values ranging from 550 to 1040 nm when stabilized with Tween 80 and 320 to 1150 nm when stabilized with Brij 92. The surfactant Brij 700 revealed the best stabilizing properties among the tested surfactants with no need for centrifugation. There were no signs of gross precipitation in the case of CXNPs stabilized by Brij 700 (Figure 2A). This was also proven by TEM microscopy (Figure 2B).

The D_h of these particles ranged from 600 to 800 nm, and the distribution of the particle size was relatively broad (Figure 3). The zeta potential values were zero except for sample BR700/20, suggesting steric stabilization and a decrease in the surface charge. The BR700/80 CXNP sample possessing the smallest particle size was used for further TEM imaging and biological testing (see below). TEM (Figure 2B) of this formulation revealed elongated nanoparticles with sizes in the submicrometer range. This result was in very good agreement with the DLS measurements. The nanoparticles exhibited sharp, faceted edges, which confirmed their nanocrystalline structure [29], but their size and concentration were too low, and their sensitivity to electron beams was too high to yield an intensive electron diffraction pattern at laboratory temperature.

Table 1. Physicochemical characteristics of the chloroxine nanoparticles.			
Sample	$D_h \pm$ SD (nm)	$\zeta \pm$ SD (mV)	Note
TW80/20	1035 ± 26	-23.0 ± 0.6	G.P.
TW80/40	1026 ± 70	-29.4 ± 1.1	G.P.
TW80/60	903 ± 34	-29.8 ± 0.8	G.P.
TW80/80	548 ± 55	-30.8 ± 1.0	G.P.
BR92/20	1153 ± 55	-34.6 ± 0.8	G.P.
BR92/40	496 ± 51	-35.3 ± 5.7	G.P.
BR92/60	517 ± 87	-35.1 ± 4.1	G.P.
BR92/80	324 ± 73	-35.0 ± 1.2	G.P.
BR700/20	831 ± 17	-18.9 ± 0.6	H.F.
BR700/40	654 ± 13	0.0 ± 0.1	H.F.
BR700/60	608 ± 5	0.0 ± 0.0	H.F.
BR700/80	580 ± 26	0.0 ± 0.1	H.F.

Samples TW80 and BR92 were analyzed after centrifugation (1500 r.p.m., 10 min).
D_h: Hydrodynamic diameter; G.P: Gross precipitation occurred, centrifugation necessary; H.F: Homogeneous formulation with no need for gross particle separation; SD: Standard deviation.
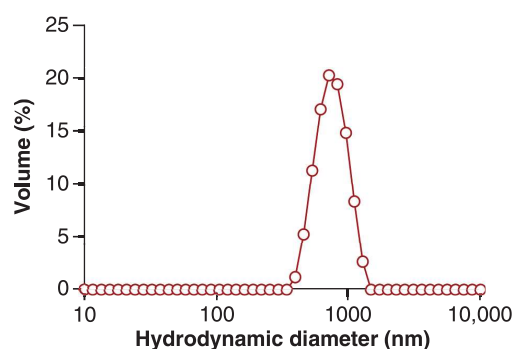
Figure 3.   Size distribution function of chloroxine nanoparticles (BR700/80) as found by dynamic light scattering.

Antimicrobial testing

The CXNP formulation (BR700/80) demonstrated antimicrobial activity against a wide range of medically important pathogenic microorganisms (Table 2) in a broth microdilution assay. Considering the Gram-positive bacterial strains studied, the resulting MIC across all of these strains was ca. 5 μg/ml, whereas the MBC values varied based on the species tested. Both *S. aureus* and *S. pyogenes* did not reveal bactericidal effects within the concentration range tested. In contrast, the CXNPs were found to be bactericidal for *C. pseudodiphtheriticum* (MBC 5–6 μg/ml) and *S. epidermidis* (MBC 12.5 μg/ml).

CXNPs were also found to be antibacterial against clinical respiratory, enteric and opportunistic Gram-negative pathogens, but with higher heterogeneity for both the MIC and MBC values. For instance, *C. sakazakii*, *P. aeruginosa* and *S. marcescens* with MICs of ca. 12 μg/ml were the most resistant strains found. An MIC of ca. 4 μg/ml was found against *B. bronchiseptica* and *S. flexneri*. In contrast, a bactericidal effect was not observed (MBC >50 μg/ml) against most Gram-negative species tested. This is probably in line with the fact that chloroxine is a microbiostatic compound [18]. The best activity was against *M. catarrhalis*; both the MIC and MBC were found to be ≤0.05 μg/ml (Table 2).

The formulation revealed antifungal potency, with MIC values of 0.2, 12.5 and 1.6 μg/ml for *Can. albicans*, *M. furfur* and *M. pachydermatis*, respectively. Furthermore, CXNPs were found to be fungicidal at clinically achievable concentrations; the MBC values ranged from 0.2 to 12.5 μg/ml (Table 2, fungi).

Cytotoxicity assessment

The authors studied the effect of CXNP on cell viability by a resazurin assay. Human skin epithelium A431 and human skin keratinocyte HaCaT cell lines were used as models for dermal cytocompatibility assessment *in vitro*.

The cytotoxic effects were observed in an incubation-dependent manner, as depicted in Figure 4. In more detail, considering the A431 cell line (Figure 4A), the obtained IC_{50} values were 31.6 ± 6.9 μg/ml and 5.9 ± 1.3 μg/ml after 48 and 72 h, respectively. The IC_{50} was not reached and thus was not estimated after 24 h. The resazurin

Table 2. Antimicrobial testing of the fabricated chloroxine formulation.

Group	Strain	Designation	Note	MIC (μg/ml)	MBC (μg/ml)
G+ bacteria	*Corynebacterium pseudodiphtheriticum*	CCM 2821	T	5	5–6
	Staphylococcus aureus subsp. *aureus*	CCM 4223		5	>50
	Staphylococcus aureus subsp. *aureus*	ATCC 33591	Methicillin-resistant	5	>50
	Staphylococcus epidermidis	CCM 2124	T	5	12.5
	Streptococcus pyogenes	CCM 7418		5–6	>50
G– bacteria	*Acinetobacter baumannii*	CCM 2355	T	5–6	25
	Bordetella bronchiseptica	CCM 6082	T	4	>50
	Cronobacter sakazakii	CCM 1902		11–12.5	>50
	Enterobacter cloacae	CCM 8574	T	8–9	>50
	Escherichia coli	CCM 3954		5–6	>50
	Klebsiella oxytoca	CCM 1901		5–6	6.25–12.5
	Klebsiella pneumoniae subsp. *pneumoniae*	CCM 7798	T	6–7	>50
	Moraxella catarrhalis	CCM 2828		≤0.05	≤0.05
	Pseudomonas aeruginosa	CCM 1960	T	12.5	>50
	Serratia marcescens	CCM 303	T	12	>50
	Shigella flexneri	CCM 4422		3–4	>50
Fungi	*Candida albicans*	CCM 8261		0.2	0.2–0.4
	Candida albicans	CCM 8215		0.2	0.4
	Malassezia furfur	DSM 6170		12.5	12.5
	Malassezia pachydermatis	DSM 6172		1.6	1.6–3

These strains were used for study of the MIC and MBC; the maximum concentration tested was 50 μg/ml.
T: Type strain; MBC: Minimum bactericidal concentration; MIC: Minimum inhibitory concentration.
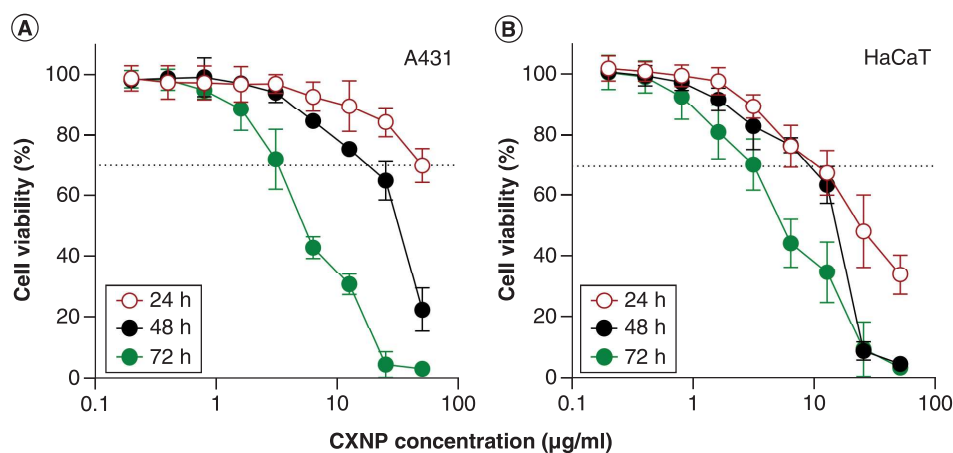

Figure 4.   Cytotoxicity of chloroxine nanoparticles. (A) Human skin epithelial A431 cells and **(B)** HaCaT human skin keratinocytes were treated with different concentrations of CXNPs (sample BR700/80) for 24, 48 and 78 h, and cytotoxicity was determined by resazurin assay. The horizontal lines indicate cell viability levels where the data above are considered noncytotoxic and below cytotoxic. The results indicate mean values ± standard deviation.
CXNP: Chloroxine nanoparticle.

assay with HaCaT cells (Figure 4B) revealed IC_{50} values of 26.0 ± 10, 12.0 ± 2.1 and 6.1 ± 2.3 μg/ml after 24, 48, and 72 h, respectively.

In vivo skin irritation

For the skin irritation study, measurements such as TEWL, colorimetry and pH were conducted for 7 consecutive days of CXNP treatment. Notably, there was no change in TEWL values during the treatment by both CXNPs and the Brij 700 solution dispersant (Figure 5A). Evaluating pH, it was found that the topical application of CXNPs did
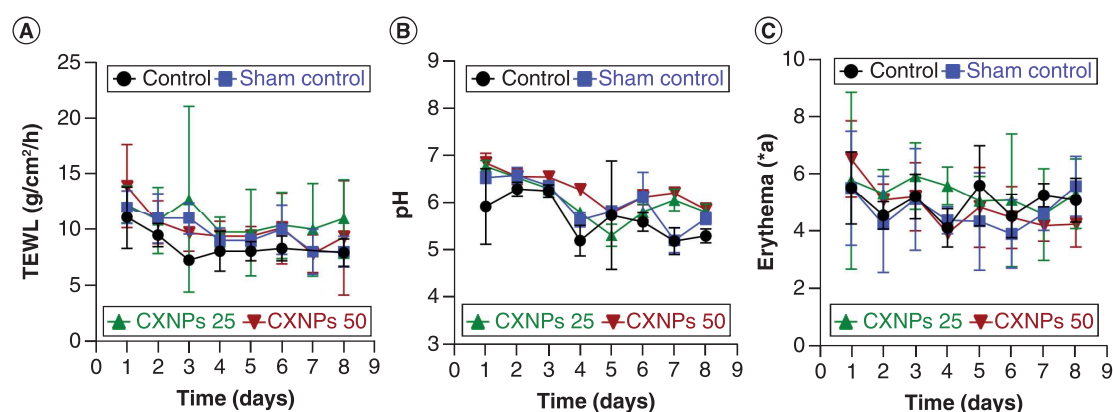
Figure 5.   *In vivo* skin tolerance of chloroxine nanoparticles. During the 7-day treatment of mouse skin, **(A)** transepidermal water loss (TEWL), **(B)** skin pH and **(C)** skin erythema (redness, a*) were assessed. Note that there was no effect of the CXNPs on the parameters discussed. The results represent mean values ± standard deviation. CXNP: Chloroxine nanoparticle.

not cause skin irritation during the 7-day treatment (Figure 5B). Finally, the colorimetry measurements of redness (a*) did not change significantly during the CXNP treatment (Figure 5C).

Additionally, the authors assessed the possible skin damage by H&E staining, as shown in Figure 6. There were no pathomorphological changes detected in skin sections from any of the experimental groups of mice: healthy control (Figures 6A & 6B), treatment with Brij 700 at a corresponding concentration (Figures 6C & 6D), CXNPs at 25 μg/ml (Figures 6E & 6F) or CXNPs at 50 μg/ml (Figures 6G & 6H). A detailed description of a representative section is depicted in Supplementary Figure 1. These observations are in line with the above-discussed skin parameters and suggest the good tolerability and nontoxicity of the prepared CXNPs.

Discussion

The framework of this study was based on chloroxine's low solubility in water as well as the urgent need for the study of novel antimicrobial interventions. This work was motivated by the goals of studying chloroxine self-association in the presence of nonionic surfactants and analyzing its relevant bioactive properties.

As presented, the authors explored the possibility of chloroxine nanoprecipitation using three different nonionic surfactants, namely, Tween 80, Brij 92 and Brij 700. The CXNP preparation was based on the presumption that the presence of a nonionic surfactant in the aqueous medium prevents the formation of gross aggregates of hydrophobic chloroxine and submicrometer particles are formed instead. The concentrations of the surfactants in the formulations were below their CMCs – 20, 40, 60 and 80% of their values – enabling the use of the minimal content of such excipients for nanoprecipitation. Although both Tween 80 and Brij 92 did not provide satisfactory formulations, it is evident that the higher the amount of surfactant used, the smaller the particles obtained in the supernatant (Table 1). Most plausibly, this was due to more efficient steric stabilization and kinetic reactions during nanoprecipitation. Simultaneously, the formulations with more surfactant exhibited more negative zeta potential values, although the charge of the Tween 80- and Brij 92-stabilized systems was obviously not sufficient for complete electrostatic stabilization.

The best stabilizing properties among the surfactants tested were revealed by Brij 700 that provided a homogeneous CXNP dispersion. This can be explained by the fact that stearyl groups possessing Brij 700 tend to interact effectively with chloroxine surfaces. This might explain why homogeneous dispersions did not form when Tween 80 and Brij 92, both possessing oleoyl/oleyl groups, were used, and steric stabilization was not sufficient. In other words, the crystalline stearyl group possesses an elevated affinity for crystalline chloroxine compared with oleoyl/oleyl (*cf.*, Figure 1). Additionally, the long poly(ethylene glycol) (PEG) chain within the Brij 700 structure presumably supports steric stabilization compared with the relatively short hydrophilic chains present within both Tween 80 and Brij 92. Overall, the authors observed efficient and favorable submicronization, which is of key importance for nanomedicines [30].

Chloroxine is a compound whose primary indication is the treatment of dandruff, seborrheic dermatitis and infectious diarrhea. Additionally, acute, subacute and/or secondary skin infections such as impetigo, folliculitis,
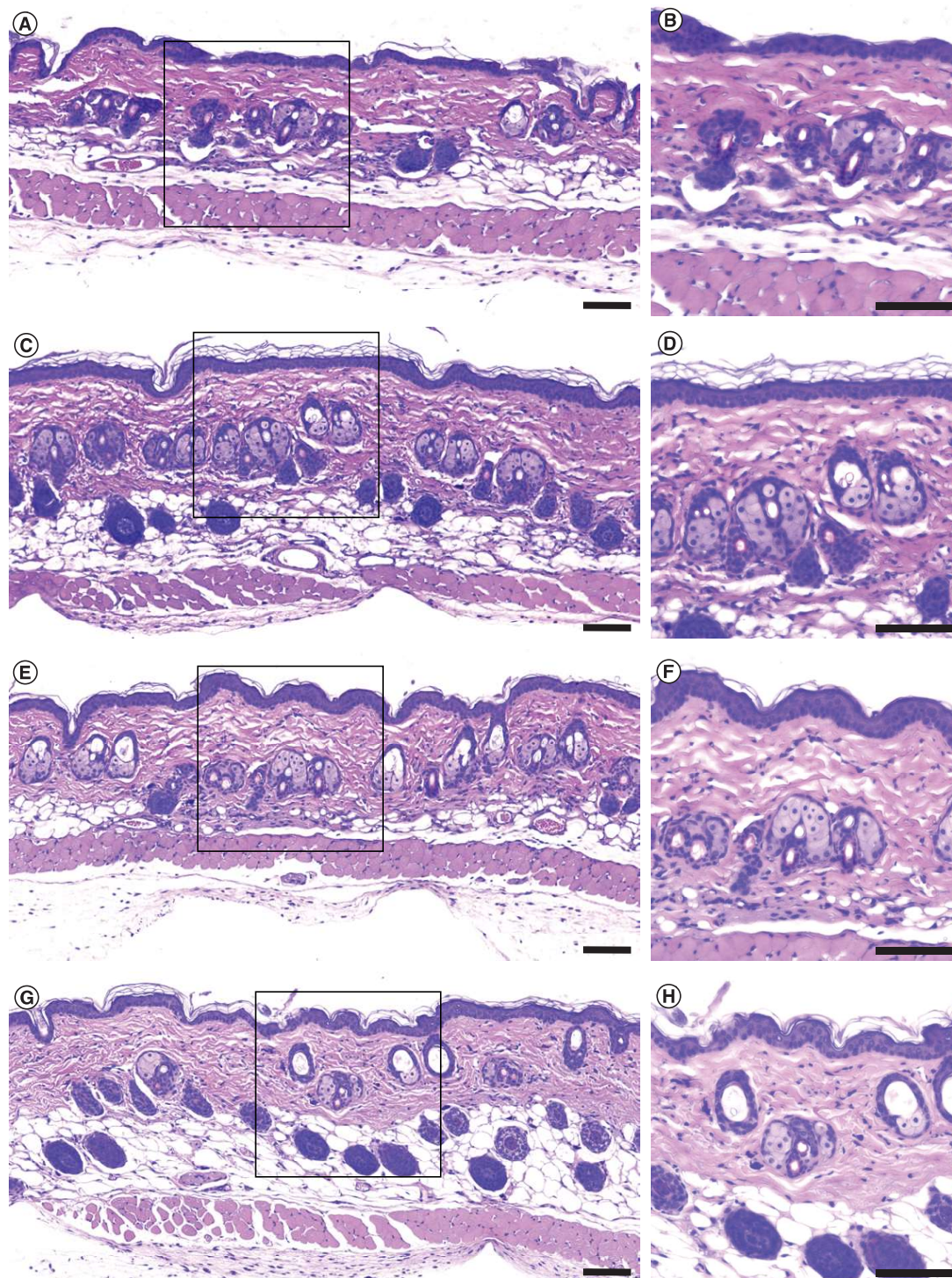
Figure 6.   *In vivo* skin tolerance of chloroxine nanoparticles assessed via histopathological examination (hematoxylin & eosin) of mouse dorsal skin 7 days after the treatment. (A & B) Skin sections from mice without any exposure, **(C & D)** mice exposed to Brij 700 solution and **(E & F)** mice exposed to chloroxine nanoparticles at 25 μg/ml and **(G & H)** 50 μg/ml are shown. Scale bars: 100 μm. For a detailed morphological description, see Supplementary Data.

intertrigo, *C. balanitis* and *C. vulvitis* represent other skin conditions for which the use of chloroxine might be indicated in extemporaneous prescription. In this work, the authors estimated the MICs and MBCs for five Gram-positive bacterial strains consisting of staphylococci, streptococci and corynebacteria, which are organisms that typically colonize human skin and are known to contribute to the majority of skin infections in general [31]. Next, the authors explored the antimicrobial activity against Gram-negative bacterial strains. Notably, the best activity was against *M. catarrhalis*, a nonmotile and aerobic diplococcus causing infections of the respiratory system, middle ear, eye, central nervous system and joints [32,33]. Finally, the authors assessed the activity against fungal pathogens. Currently, they are emerging because both cutaneous and subcutaneous mycoses are a source of significant morbidity in (but not limited to) immunocompromised patients [34]. The most common etiological agents of clinically relevant conditions include *Candida* spp., *Aspergillus* spp., *Cryptococcus* spp. and *Malassezia* spp. [35,36]. Despite the relatively large number of antifungal agents available, the therapeutic outcome can be suboptimal due to their toxic profile and physicochemical properties. Nanocarrier systems, however, have been suggested to tackle these issues [37–39]. Hence, using three medically important fungal pathogens – *Can. albicans*, *M. furfur* and *M. pachydermatis* – the authors studied the effect of CXNPs. It is worth emphasizing that the fabricated formulation was found to be fungicidal at concentration values ranging from 0.2 to 12.5 µg/ml.

Overall, one may hypothesize that, based on the broad antimicrobial activity of the intervention described, CXNPs can be effective and promising, for example, as a topical formulation, avoiding coinfections of undamaged skin (*cf.* the cytotoxicity assessment) and other dermal conditions related to, for instance, staphylococci, streptococci and emerging fungal pathogens.

Note that the use of particles in the submicrometer size range has a possible risk due to interactions with epidermal and dermal cells, which can lead to cytotoxicity and undesired immune responses [40]. Hence, the authors studied the dermal cytocompatibility *in vitro*. Although there can be concern about the observed CXNP effects on 2D skin cell cultures (Figure 4), several aspects explaining the presumable safety of such an intervention should be stressed. As indicated above, antimicrobial susceptibility testing revealed clinically achievable MIC and MBC values for most of the relevant species causing skin infections and conditions, such as *S. aureus*, *S. pyogenes*, *S. epidermidis*, *Can. albicans* and *M. pachydermatis*. Most of these MIC and/or MBC values were below or around the cytotoxicity level, minimizing the negative effects observed in Figure 4. Additionally, it is worth stressing that 2D skin cell cultures only partially reflect the real skin features. In other words, one may hypothesize that in the case of topical use, the outer stratum corneum layers limit CXNP bead penetration and form an effective barrier [41]. Finally, chloroxine is a well-known molecule that is used all over the world both orally and topically, indicating that there is no doubt about CXNP feasibility in the context of topical use. To address this issue, the authors carried out a skin irritation study *in vivo*. It was evaluated *in vivo* at two different concentrations of CXNPs, 25 and 50 µg/ml, both of which were above the MIC/MBC values of the susceptible microorganisms tested. As presented, there was no change in TEWL and pH values. Also, CXNP intervention did not lead to erythema that could be triggered by skin irritation [42]. Notably, histopathological examination of the skin revealed normal morphology without any pathological process observed in the epidermis, dermis, skin adnexa, subcutaneous tissue or muscular layer under the subcutis, suggesting that neither CXNPs nor Brij 700 (sham control) affected the stratum corneum barrier function.

Conclusion

In the current study, we addressed the low solubility of chloroxine in water, which limits its clinical use despite its antimicrobial activities. For the first time, nanocrystalline chloroxine particles stabilized by the nonionic surfactant Brij 700 were prepared and their antimicrobial activities and dermal cytotoxicity were studied. The CXNP formulation demonstrated microbiostatic activity against a range of Gram-positive and Gram-negative bacteria, as well as three fungal species (*M. furfur*, *M. pachydermatis* and *Can. albicans*) associated with skin conditions such as seborrheic dermatitis and dandruff. The intervention was found to be tolerated *in vitro* by both HaCaT and A431 human skin cells at clinically achievable levels related to both MIC and MBC. Importantly, preliminary safety examination of the skin showed acceptable skin tolerance of the CXNPs by mice. These results suggest a new means to solve problems such as the poor water solubility of chloroxine and its gross precipitation in water. Overall, the CXNPs have potential applications in the field of antimicrobial interventions and might be considered an innovative approach to the topical clinical use of chloroxine.

Summary points

- Bacterial and fungal infections represent a major health problem on a global scale.
- Currently, nanoparticles with antimicrobial activities are being studied as promising interventions against a wide range of cutaneous infections.
- The studied chloroxine (5,7-dichloro-8-hydroxyquinoline), a water-insoluble compound. It was submicronized by nanoprecipitation and stabilized by a nonionic surfactant.
- The resulting chloroxine nanoparticles were characterized and studied by a broth microdilution assay against several medically important bacteria and fungi.
- The prepared nanoparticles exhibited good tolerability in terms of skin irritation *in vivo*.
- The prepared nanoformulation shows great promise for interventions for both cutaneous infection control and prophylaxis.

Supplementary data

To view the supplementary data that accompany this paper please visit the journal website at: www.futuremedicine.com/doi/suppl/10.2217/nnm-2021-0323

Author contributions

J Trousil designed and formulated the chloroxine particles and all of the experimental testing. Particle physicochemical characterization was carried out by both J Trousil and T Nejedlý. T Urbánek helped with physicochemical characterization and reviewed the manuscript. Biological testing was carried out by both J Trousil and J Matějková. M Šlouf was responsible for the TEM analysis. Y-S Dai and J-Y Fang were responsible for the *in vivo* experiments. M Škorič helped with the histopathology result description. J Trousil and T Urbánek wrote the manuscript. M Hrubý proposed the concept of chloroxine submicronization/stabilization and reviewed the manuscript.

Ethical conduct of research

The authors state that they have obtained appropriate institutional review board approval or have followed the principles outlined in the Declaration of Helsinki for all human or animal experimental investigations.

References

Papers of special note have been highlighted as: ● of considerable interest

1. Blair MJ, Jones JD, Woessner AE, Quinn KP. Skin structure-function relationships and the wound healing response to intrinsic aging. *Adv. Wound Care.* 9(3), 127–143 (2020).

2. Pormohammad A, Monych NK, Ghosh S, Turner DL, Turner RJ. Nanomaterials in wound healing and infection control. *Antibiotics* 10(5), 2176 (2021).

● **Provides an overview on the current state of nanomedicines for the control of skin infections and wound healing.**

3. Wang W, Lu K-J, Yu C-H, Huang Q-l, Du Y-Z. Nano-drug delivery systems in wound treatment and skin regeneration. *J. Nanobiotechnol.* 17(1), 82 (2019).

4. Ahmadi M, Adibhesami M. The effect of silver nanoparticles on wounds contaminated with *Pseudomonas aeruginosa* in mice: an experimental study. *Iran. J. Pharm. Res.* 16(2), 661–669 (2017).

5. Westendorf AM. Applications of nanoparticles for treating cutaneous infection. *J. Investig. Dermatol.* 133(5), 1133–1135 (2013).

6. Alalaiwe A, Wang P-W, Lu P-L, Chen Y-P, Fang J-Y, Yang S-C. Synergistic anti-MRSA activity of cationic nanostructured lipid carriers in combination with oxacillin for cutaneous application. *Front. Microbiol.* 9, 1493 (2018).

7.   Sverdlov Arzi R, Sosnik A. Electrohydrodynamic atomization and spray-drying for the production of pure drug nanocrystals and co-crystals. *Adv. Drug Deliv. Rev.* 131, 79–100 (2018).

8.   Wang L, Hu C, Shao L. The antimicrobial activity of nanoparticles: present situation and prospects for the future. *Int. J. Nanomedicine* 12, 1227–1249 (2017).

9.   Permana AD, Anjani QK, Sartini *et al.* Selective delivery of silver nanoparticles for improved treatment of biofilm skin infection using bacteria-responsive microparticles loaded into dissolving microneedles. *Mater. Sci. Eng. C.* 120, 111786 (2021).

•   **A recent publication in the antibacterial research field. The authors explored bacteria-responsive microparticles for the treatment of skin infections.**

10.   Qiu L, Wang C, Lan M *et al.* Antibacterial photodynamic gold nanoparticles for skin infection. *ACS Appl. Bio Mater.* 4(4), 3124–3132 (2021).

11.   Walduck A, Sangwan P, Vo QA *et al.* Treatment of *Staphylococcus aureus* skin infection *in vivo* using rifampicin loaded lipid nanoparticles. *RSC Adv.* 10(55), 33608–33619 (2020).

12.   Garg A, Sharma GS, Goyal AK, Ghosh G, Si SC, Rath G. Recent advances in topical carriers of anti-fungal agents. *Heliyon* 6(8), e04663 (2020).

13.   Sousa F, Ferreira D, Reis S, Costa P. Current insights on antifungal therapy: novel nanotechnology approaches for drug delivery systems and new drugs from natural sources. *Pharmaceuticals* 13(9), 248 (2020).

•   **Elucidates emerging strategies for the treatment of fungal infections using nanomedicines.**

14.   Mallmann EJJ, Cunha FA, Castro BNMF, Maciel AM, Menezes EA, Fechine PBA. Antifungal activity of silver nanoparticles obtained by green synthesis. *Rev. Inst. Med. Trop. Sao Paulo* 57(2), 165–167 (2015).

15.   Mumtaz T, Ahmed N, Hassan Nu, Badshah M, Khan S, Rehman A. Voriconazole nanoparticles-based film forming spray: an efficient approach for potential treatment of topical fungal infections. *J. Drug Deliv. Sci. Technol.* 102973 (2021). doi.org/10.1016/j.jddst.2021.102973

16.   Gigliobianco RM, Casadidio C, Censi R, Di Martino P. Nanocrystals of poorly soluble drugs: drug bioavailability and physicochemical stability. *Pharmaceutics* 10(3), 134 (2018).

17.   Shi H, Xie Y, Xu J, Zhang X, Wang H. Cosolvency and mathematical modeling analysis of chloroxine in some binary solvent system. *J. Chem. Eng. Data.* 63(9), 3353–3359 (2018).

18.   Niu H, Yee R, Cui P *et al.* Identification of agents active against methicillin-resistant *Staphylococcus aureus* USA300 from a clinical compound library. *Pathogens* 6(3), 44 (2017).

19.   Chaturvedi S, Rajkumar SS, Li X, Hurteau GJ, Shtutman M, Chaturvedi V. Antifungal testing and high-throughput screening of compound library against *Geomyces destructans*, the etiologic agent of geomycosis (WNS) in bats. *PLoS ONE* 6(3), e17032 (2011).

20.   Barker S, Harding SV, Gray D, Richards MI, Atkins HS, Harmer N. Drug screening to identify compounds to act as co-therapies for the treatment of pathogenic *Burkholderia*. *PLoS ONE* 16(3), e0248119 (2019).

21.   Hans Schwarzkopf and Henkel GmbH. US3886277A (1973).

22.   Jäger E, Höcherl A, Janoušková O *et al.* Fluorescent boronate-based polymer nanoparticles with reactive oxygen species (ROS)-triggered cargo release for drug-delivery applications. *Nanoscale* 8(13), 6958–6963 (2016).

23.   Paiuk O, Mitina N, Slouf M *et al.* Fluorine-containing block/branched polyamphiphiles forming bioinspired complexes with biopolymers. *Colloids Surf. B.* 174, 393–400 (2019).

24.   Zeinali E, Sadeghi G, Yazdinia F, Shams-Ghahfarokhi M, Razzaghi-Abyaneh M. Clinical and epidemiological features of the genus *Malassezia* in Iran. *Iran. J. Microbiol.* 6(5), 354–360 (2014).

25.   Rojas FD, Sosa Mde L, Fernández MS, Cattana ME, Córdoba SB, Giusiano GE. Antifungal susceptibility of *Malassezia furfur*, *Malassezia sympodialis*, and *Malassezia globosa* to azole drugs and amphotericin B evaluated using a broth microdilution method. *Med. Mycol.* 52(6), 641–646 (2014).

26.   Zhang L-W, Al-Suwayeh SA, Hsieh P-W, Fang J-Y. A comparison of skin delivery of ferulic acid and its derivatives: evaluation of their efficacy and safety. *Int. J. Pharm.* 399(1), 44–51 (2010).

27.   Hsieh P-W, Hung C-F, Lin C-H, Huang C-W, Fang J-Y. Anti-melasma codrug of retinoic acid assists cutaneous absorption with attenuated skin irritation. *Eur. J. Pharm. Biopharm.* 114, 154–163 (2017).

28.   Fang J-Y, Tang K-W, Yang S-H *et al.* Synthetic naphthofuranquinone derivatives are effective in eliminating drug-resistant *Candida albicans* in hyphal, biofilm, and intracellular forms: an application for skin-infection treatment. *Front. Microbiol.* 11, 2053 (2020).

29.   Ng SW. 5,7-Dichloroquinolin-8-ol. *Acta Crystallogr. Sect. E Struct. Rep. Online* 65(5), o1131 (2009).

30.   Fenaroli F, Robertson JD, Scarpa E *et al.* Polymersomes eradicating intracellular bacteria. *ACS Nano.* 14(7), 8287–8298 (2020).

•   **An interesting publication in the antibacterial research field. The authors explored polymerosomes as tools for the treatment of intracellular bacterial infections.**

31.   Ki V, Rotstein C. Bacterial skin and soft tissue infections in adults: a review of their epidemiology, pathogenesis, diagnosis, treatment and site of care. *Can. J. Infect. Dis. Med. Microbiol.* 19(2), 173–184 (2008).

32. Maleki A, Mirnaseri Z, Kouhsari E *et al.* Asymptomatic carriers of *Neisseria meningitidis* and *Moraxella catarrhalis* in healthy children. *New Microbes New Infect.* 36, 100691 (2020).

33. Milner DA, Pecora N, Solomon I, Soong TR. *Neisseria* and *Moraxella* species infections. In: *Diagnostic Pathology: Infectious Diseases.* Elsevier, PA, USA (2015).

34. Guégan S, Lanternier F, Rouzaud C, Dupin N, Lortholary O. Fungal skin and soft tissue infections. *Curr. Opin. Infect. Dis.* 29(2), 124–130 (2016).

35. Bartram L, Aaron JG. Fungal necrotizing skin and soft tissue infections. *Curr. Fungal Infect. Rep.* 13(4), 146–156 (2019).

36. Iatta R, Cafarchia C, Cuna T *et al.* Bloodstream infections by *Malassezia* and *Candida* species in critical care patients. *Med. Mycol.* 52(3), 264–269 (2014).

37. Verma S, Utreja P. Vesicular nanocarrier based treatment of skin fungal infections: potential and emerging trends in nanoscale pharmacotherapy. *Asian J. Pharm. Sci.* 14(2), 117–129 (2019).

38. Mussin JE, Roldán MV, Rojas F, Sosa MdlÁ, Pellegri N, Giusiano G. Antifungal activity of silver nanoparticles in combination with ketoconazole against *Malassezia furfur. AMB Express.* 9(1), 131 (2019).

39. Kumari M, Giri VP, Pandey S *et al.* An insight into the mechanism of antifungal activity of biogenic nanoparticles than their chemical counterparts. *Pestic. Biochem. Phys.* 157, 45–52 (2019).

40. Smijs TG, Bouwstra JA. Focus on skin as a possible port of entry for solid nanoparticles and the toxicological impact. *J. Biomed. Nanotechnol.* 6(5), 469–484 (2010).

41. Filipe P, Silva JN, Silva R *et al.* Stratum corneum is an effective barrier to TiO_2 and ZnO nanoparticle percutaneous absorption. *Skin Pharmacol. Physiol.* 22(5), 266–275 (2009).

42. Siddique MI, Katas H, Jamil A *et al.* Potential treatment of atopic dermatitis: tolerability and safety of cream containing nanoparticles loaded with hydrocortisone and hydroxytyrosol in human subjects. *Drug Deliv. Transl. Res.* 9(2), 469–481 (2019).

Nanocrystalline chloroxine possesses broad-spectrum antimicrobial activities and excellent skin tolerability in mice

Jiří Trousil[1, †, *], Jana Matějková[2, 3, †], You-Shan Dai[4], Tomáš Urbánek[1], Miroslav Šlouf[1], Miša Škorič[5], Tomáš Nejedlý[1], Martin Hrubý[1], Jia-You Fang[4]

[1] Institute of Macromolecular Chemistry, Czech Academy of Sciences, Heyrovského nám. 2, 162 00 Prague 6, Czechia

[2] Department of Medical Microbiology, Second Faculty of Medicine, Charles University and Motol University Hospital, V Úvalu 84, 150 06 Prague 5, Czechia

[3] Military Health Institute, Military Medical Agency, Tychonova 1, 160 00 Prague 6, Czechia

[4] Pharmaceutics Laboratory, Graduate Institute of Natural Products, Chang Gung University, Taoyuan 333, Taiwan

[5] Department of Pathological Morphology and Parasitology, Faculty of Veterinary Medicine, University of Veterinary Sciences Brno, Palackého tř. 1946/1, 612 42 Brno, Czechia

[†] These authors contributed equally to this work.

[*] Corresponding author. E-mail address: trousil@imc.cas.cz, jiri.trousil@centrum.cz
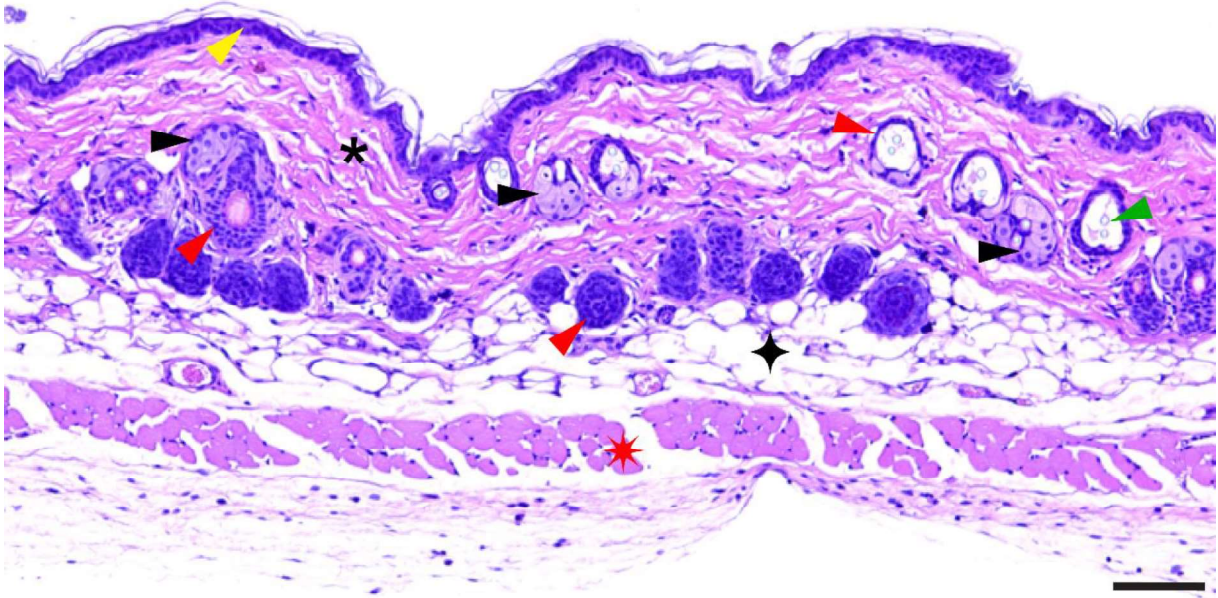
Figure S1 Representative H&E-stained section of mouse skin and a description of the morphological structures. A Brij 700-treated mouse skin (sham control) section is shown. Yellow arrowhead – normal epidermis with superficial keratinization; black arrowheads – normal sebaceous glands; green arrowhead – hairs on a transversal section inside a hair follicle; black asterisk – normal dermis formed by fibrous collagenous tissue; red arrowhead – normal hair follicles and the wall of a hair follicle on a transversal section; black four-pointed star – normal subcutaneous adipose and loose connective tissue; red eight-pointed star – muscular layer with underlying loose connective tissue. Scale bar: 100 μm.

Appendix 4

Urbánek, T.; Ivanko, I.; Svoboda, J.; Tomšík, E.; Hrubý, M., Selective potentiometric detection of reactive oxygen species (ROS) in biologically relevant concentrations by a modified metalized polyporphyrine sensing layer coated with nonbiofouling poly(2-alkyl-2oxazoline)s. *Sensors and Actuators B: Chemical* **2022**, 363, 131827. IF = 9.221

Contents lists available at ScienceDirect

Sensors and Actuators: B. Chemical

Selective potentiometric detection of reactive oxygen species (ROS) in biologically relevant concentrations by a modified metalized polyporphyrine sensing layer coated with nonbiofouling poly (2-alkyl-2oxazoline)s

Tomáš Urbánek, Iryna Ivanko, Jan Svoboda, Elena Tomšík [*], Martin Hrubý [*]

Institute of Macromolecular Chemistry, Czech Academy of Sciences, Heyrovského náměstí 2, 16200 Prague 6, Czech Republic

A B S T R A C T

We built a robust selective potentiometric sensor of reactive oxygen species (ROS) as a thin layer applied on the surface of smart implants, which enables the detection and localization of inflammation at an early stage. The sensor consists of a conductive polymer layer based on polythiophene with an incorporated porphyrin-metal complex that potentiometrically detects the presence of ROS. This sensor is covalently coated with a non-biofouling layer of poly(2-methyl-2-oxazoline), which works as a biocompatibilizer but mainly prevents the sorption of proteins and other biomacromolecules naturally occurring in organisms, which could interfere with the ROS signal. We have shown that our potentiometric sensor shows a rapid response to hydrogen peroxide, does not experience interference with bovine serum albumin as a model serum protein when sensing ROS, is able to fully reversibly detect ROS with a linear response within a very wide range of biologically relevant concentrations and, most importantly, is able to distinguish between hydrogen peroxide and hypochlorite. We also performed a head-to-head comparison of two positional isomers of thienylated porphyrine for sensor applications (2TTP and 3TTP, with 3TTP shown to be more appropriate) and four different coordinated metals (Cu, Fe, Co and Mn, with Cu and especially Fe shown to be the most appropriate).

1. Introduction

It has been shown that many types of materials can be coated with conductive polymers such as polyaniline, polypyrrole, polythiophene, poly(3,4-ethylenedioxythiophene) (PEDOT) or their derivatives [1,2]. Due to the polymer coating, the surface physical, chemical, and/or electrical properties could be tuned by choosing the chemical structure of the polymer that forms the thin layer. In addition, the morphology and thickness of the polymer film also play key roles [3]. The electrochemical potential of such a layer may change if an external stimulus appears, and the signal can subsequently be detected. The advantages of PEDOT-based sensors are relatively high conductivity ($\sigma = 300 - 600$ $S \cdot cm^{-1}$) combined with significant chemical and thermal stability [2,4]. Therefore, such materials have been investigated in many biomedical applications, especially as biosensors. PEDOT has been described for the selective detection of dopamine [5] and glucose sensing [6] or in general as a stable and long-lasting neural recording device [7]. Another promising polymer is based on the porphyrin structure and its derivatives. The redox properties of porphyrin-based self-assembled sensing layers are determined by the chemical substituents and by the coordinated metal in the material [8,9].

The nonbiofouling property of surfaces is crucial for use in biological environments. Unfortunately, most of the surfaces attract proteins, other biomolecules, whole cells and microorganisms. This spontaneous and unwanted adsorption prevents further communication between the material surface and electrolyte [10]. There are several reasons for considering surface treatment. For example, a particle covered by a nonbiofouling layer cannot be recognized properly by the immune system because of the missing protein corona. There is also a need to prepare nonbiofouling surfaces when communication between the surface and electrolyte is required, e.g., in sensor applications. The protecting layer can be composed of hydrophobic fluorinated alkanes, zwitterions with high hydration capability or water-soluble poly(ethylene oxide), which is the most commonly used [11]. The last mentioned approach is

often called PEGylation. Poly(ethylene oxide) is currently being replaced with other hydrophilic polymers, such as poly(alkyloxazolines) because there are concerns about the presence of antibodies produced by the immune system, which is connected with the massive overuse of poly(ethylene oxide)-containing products in medications and in households.

Bacteria rank among the main pathogens threatening human health. Once the germ is recognized as a threat, a series of biological processes occur depending on the body part and the circumstances resulting in a complex defense reaction, inflammation. Specialized cells that are involved in the host defense response [12], predominantly macrophages, neutrophils, and endothelial cells, create a specific microclimate there [13]. The pathologically higher concentrations of reactive oxygen species (ROS) in the inflamed area and in its vicinity are one of the key features [14].

In general, ROS are defined as a group of oxygen compounds with strong oxidizing capabilities. The most biologically relevant ROS are the superoxide anion $O2^{\bullet-}$, hydroxyl radical $OH^\bullet$, hydrogen peroxide H_2O_2, and hypochlorite ClO^- [15,16]. Physiological concentrations of ROS are relatively low but are essential for complex signaling functions related to cell growth, the adhesion of cells towards other cells, differentiation, senescence, or apoptosis [15,17]. In the current work, two major ROS compounds (particularly H_2O_2 and ClO^-) will be investigated. There are few major ROS sources in human organisms. ROS are steadily released through the electron transport chain or cytochrome P450 as by-products. In addition, cells involved in the inflammatory response, phagocytes or endothelial cells, are able to increase the concentrations of ROS via NADPH oxidases [18]. Studies have shown that ROS cause the oxidation of proteins and lipids within the cell membrane and damage to DNA. Thus, inflammatory disease can progress rapidly [19].

One of the dangerous problems during joint replacement is complications connected with the post-surgery infections. Infection is caused by bacteria that form biofilms on surfaces and is referred to as biofilm-related infections (BRIs). Biofilms are thin layers of microorganisms attached to a surface protected by extracellular matrix and are composed mainly of functional amyloids, proteoglycans, glycosaminoglycans, lipids, and extracellular DNA [20]. According to the US National Institutes of Health, this form of infection accounts for over 80% of microbial infections in the body [21]. Common examples of BRI include implant-related infections, such as those that may follow joint replacement, osteosynthesis, mechanical heart valves, breast implants, indwelling catheters, ventriculo-peritoneal shunts, etc [20,22]. It is also worth noting that due to the bioresponse, strong pathophysiological changes in the microclimate of an affected surface occur (decrease in pH, formation of different ROS, depletion of Fe ions and increase in the concentration of Ca ions) [14]. These divergences could be used for the indirect detection of inflammation if corresponding in vivo sensors were available. Thus, treatment would be possible before any serious infectious complications are manifested.

It is worth noting that hydrogen peroxide and superoxide are generated to an increased extent not only in inflamed but also in tumour and ischaemic tissue. It was found that the function of hypoxia-inducible factor 1α (HIF1α) is regulated by ROS. In general, the mitochondrial electron transport chain generates more ROS due to a lower supply of oxygen and, thus, HIF1α activation [16,23,24]. On the other hand, hypochlorite is produced when so-called neutrophil extracellular traps are being formed. This process is often called netosis and is an important part of the innate immune system [25]. Therefore, if one would distinguish hydrogen peroxide (as a hallmark of inflammation in general) from hypochlorite (typical for bacterial infections) by in situ sensing, it would be of great interest in diagnostics, e.g., orthopedic implants (as blood plasma C-reactive protein is only a general and not site-specific marker of bacterial infection).

Semiconducting polymers have been utilized for the construction of sensing layers. Amperometric sensors for ROS (e.g., for superoxide [26, 27] and NO [28] based on iron porphyrines with imidazole axial

ligands) have been constructed; however, they show a very limited lifetime in the presence of blood proteins even if coated with Nafion® [28] or heparin [27], which is somewhat longer with carboxymethylated dextran [26]. From a practical point of view, however, the efficient diffusion range of superoxide in biological environments is limited due to its extreme reactivity, and thus, it is questionable how it would reach the sensor. Nitrogen monoxide, although also overproduced in inflamed regions, is not a straightforward inflammation marker. These sensors do not detect hydrogen peroxide and hypochlorite, and their concentration-response linearity window is narrow.

Over the last few years, potentiometric sensors have demonstrated huge potential for analysis [29]. Beyond the excellent analytical performances for the detection of important targets, the challenge now lies in bringing those sensors to an in situ format and obtaining valuable information directly. Technically speaking, the instrumentation for potentiometric assessment is simple, low cost and requires minimal space and energy supply. In addition, the potentiometric sensor seems ideal for the fabrication of miniaturized sensors with sufficient analytical performance [29].

Therefore, in the current work, we decided to use a potentiometric method to selectively detect H_2O_2 and ClO^- ions. The concept of the work is the preparation of a robust selective potentiometric sensor of ROS as a thin layer applied on the surface of smart implants, which enables the detection and localization of inflammation at an early stage. The sensor consists of a conductive polymer layer based on polythiophene with an incorporated porphyrin-metal complex that potentiometrically detects the presence of ROS. The macroinitiators 2TTP and 3TTP differ in the number of functional groups used. There were four cases of 2TTP and eight cases of 3TTP. This sensor is covalently coated with a nonbiofouling layer of poly(2-methyl-2-oxazoline), which works as a biocompatibilizer but mainly prevents the sorption of proteins and other biomacromolecules naturally occurring in organisms, which could interfere with the ROS signal. It also prolongs the device life in vivo. We have shown that our potentiometric sensor shows a rapid response to hydrogen peroxide, does not experience interference with bovine serum albumin as a model serum protein when sensing ROS, is able to fully reversibly detect ROS with a linear response within a very wide range (covering 4 orders of magnitude in concentration) of biologically relevant concentrations (with extremely low detection limit 50 nM, which is better than even for enzymatic electrodes) and, most importantly, is able to distinguish between hydrogen peroxide and hypochlorite. Therefore, we developed for the first time a simple sensor fulfilling all of the properties needed for biomedical sensing of in situ inflammation. Last but not least, we, for the first time, compared two positional isomers of thienylated porphyrine for sensor applications (2TTP and 3TTP, with 3TTP shown to be more appropriate) and four different coordinated metals (Cu, Fe, Co and Mn, with Cu and especially Fe shown to be the most appropriate).

2. Materials and methods

2.1. Experimental section/methods

Ammonium iron(II) sulfate hexahydrate (98%, Sigma-Aldrich Ltd., Prague, Czech Republic), 3-(bromomethyl)thiophene (BrT, 95%, abcr GmbH, Karlsruhe, Germany), formic acid (98%, Sigma-Aldrich Ltd. Prague, Czech Republic), chloroform stabilized with amylene (pure, Sigma-Aldrich Ltd., Prague, Czech Republic), cobalt(II) chloride hexahydrate (98%, Sigma-Aldrich Ltd., Prague, Czech Republic), copper(II) chloride (Sigma-Aldrich Ltd., Prague, Czech Republic), hydrochloric acid (36.5–38%, Sigma-Aldrich Ltd., Prague, Czech Republic), manganese(II) chloride monohydrate (> 97%, Sigma-Aldrich Ltd., Prague, Czech Republic) 1-methylimidazole (97%, Sigma-Aldrich Ltd., Prague, Czech Republic), propionic acid (Sigma-Aldrich Ltd., Prague, Czech Republic), pyrrol (98%, Sigma-Aldrich Ltd., Prague, Czech Republic), 2-thiophenecarboxaldehyde (98%, Sigma-Aldrich Ltd., Prague, Czech

Republic), 3-thiophenecarboxaldehyde (98%. Sigma-Aldrich Ltd., Prague, Czech Republic) and phosphate-buffered saline (PBS, from tablets, Merck KGaA, Darmstadt, Germany) were used as received. Acetonitrile (Lachner Ltd., Neratovice, Czech Republic) was dried over CaH_2 and distilled prior to use and 2-methyl-2-oxazoline (MeOx, 98%, Sigma-Aldrich Ltd., Prague, Czech Republic) was dried over BaO and distilled prior to use.

^1H and ^{13}C NMR spectra were recorded using a Bruker Avance Neo spectrometer operating at 400.13 and 100.61 MHz. The acquisition parameters for 1 H and 13 C NMR were respectively as follows: 90° pulse width 16.5 and 10 µs, relaxation delay 10 s, acquisition time 2.73 and 1.72 s, 32 and 3000 scans at temperature 300 K. The chemical shifts are relative to tetramethylsilane (TMS) using hexamethyldisiloxane (HMDSO, δ = 0.05 and 2 ppm from TMS) as the internal standard.

Number average molecular weight M_n and dispersity $Đ$ of the samples P1-P3 were determined by size exclusion chromatography (SEC) equipped with PLgel 5 µm 100 Å and DeltaGel Mixed-B columns. The mixture of chloroform, isopropyl alcohol and triethylamine in volume ratio 94:4:2 was used as a mobile phase at a flow rate 1 mL·min^{-1}. The detection was done by differential refractometer Shodex RI 71. Poly (methyl metacrylate) standards (PSS GmbH, Germany) were used for calibration.

Molar masses of synthesized products 2TTP and 3TTP were measured by matrix-assisted laser desorption/ionization with time-of-flight mass spectroscopy (MALDI-TOF MS). Spectra were obtained with an UltrafleXtreme (Bruker Daltonics, Bremen, Germany) in the positive ion reflection mode. The spectra were the sum of 25000 shots with a DPSS, Nd: YAG laser (355 nm, 2000 Hz). Delayed extraction and external calibration were used. The samples were prepared by a dried droplet method: solutions of sample (10 mg·mL^{-1}) and of DCTB (trans-2-[3-(4-t-butyl-phenyl)− 2-methyl-2-propenylidene] malonitrile, Sigma–Aldrich, 10 mg·mL^{-1}) as a matrix in THF (tetrahydrofuran, Sigma–Aldrich, ≥ 99.9%) were mixed in the volume ratio 4:20. 1 mL of the mixture was deposited on the ground-steel target plate. Drop was dried in the ambient atmosphere.

Content of C, H, N and S was determined by FlashSmart™ Elemental Analyzer (Thermo Fisher Scientific Ltd., Czech Republic). Approximately 1.5 mg of the sample was weighed to a tin capsule using the precision weighing balance Sartorius SE 2-OCE. Then, about 10 mg of vanadium pentoxide was added. The capsule was sealed and inserted into the autosampler of the Analyzer and the standard operational procedures were employed.

Absorption spectra of 2TTP and 3TTP were measured by Evolution 220 UV-Visible Spectrophotometer (Thermo Fisher Scientific Ltd., Czech Republic). The samples were dissolved in tetrahydrofuran and placed in quartz cuvette. The measured spectra with typical Soret bands are shown in Fig. S4) and the maxima of absorption occur at 426 (2TTP) and 421 nm (3TTP), respectively.

Monomers 2TTP and 3TTP were electrochemically polymerized on fluorine-doped tin oxide (FTO) and glassy carbon (GC) supports during cyclic voltammetry. The spectral measurement was performed using an AvaSpec-ULS2048L spectrophotometer (Avantes). Polymerization and electrochemical characterization of polymers were performed using an AUTOLAB PGSTAT302N potentiostat with FRA32M Module and Nova software 2.2. Electrochemical characterization was performed using a three-electrode set up where a Pt electrode with an area of 1.2 cm^2 was used as a counter electrode and Ag/AgCl (3 M KCl) was utilized as a reference electrode. Whereas, the electrochemical polymerization took place in the presence of Ag/Ag$^+$ as a reference electrode. Electrochemical impedance spectroscopy (EIS) measurements were performed in the frequency range from 10 kHz to 0.1 Hz with 10 mV amplitude. The Kronig–Kramers test was applied to verify the obtained EIS data.

Potential stability of poly-2TTP and poly-3TTP based electrodes were measured by using 6-channel high input impedance voltmeter with the input impedance of 10^{10} Ω, (Lawson Laboratories, Malvern, PA, USA).

Scanning Electron Microscopy was done with a JEOL 6400 microscope (Japan).

X-ray photoelectron spectroscopy (XPS) measurements were performed using a K-Alpha+ XPS spectrometer (ThermoFisher Scientific, UK) operating at a base pressure of 1.0×10^{-7} Pa. The data acquisition and processing were performed using the Thermo Avantage software. All samples were analyzed using a microfocused, monochromated Al Kα X-ray radiation (400 µm spot size) with pass energy of 200 eV for survey and 50 eV for high-energy resolution core level spectra. The X-ray angle of incidence was 30° and the emission angle was along the surface normal. The binding energy scale of the XPS spectrometer was calibrated by the well-known positions of the C 1 s C–C and C–H, C–O and C (=O)–O peaks of polyethylene terephthalate and Cu 2p, Ag 3d, and Au 4 f peaks of Cu, Ag and Au metals, respectively. The obtained high-resolution spectra were fitted with Voigt profiles to review the individual contributions of present chemical species.

Raman spectra of poly-2TTP and poly-3TTP films were obtained using Renishaw in Via Reflex Raman microscope (Renishaw, UK) with high efficiency 250 mm focal length spectrograph equipped with research grade Leica DM LM microscope 514 nm lasers. The scattered light was analyzed by the spectrograph with holographic gratings 1200 lines mm^{-1}.

3. Synthetic procedures

3.1. Synthesis and characterization of α-thiophene poly(2-methyl-2-oxazoline)

Microwave-assisted cationic ring opening polymerization was carried out in a Biotage Initiator+ equipped with a Robot sixty autosampler (Biotage, Sweden) in a crimped glass vial. A dry vial equipped with a magnetic stir bar was charged with acetonitrile, 3-(bromomethyl)thiophene, and 2-methyl-2-oxazoline under argon flow so that the initial monomer concentration equalled 2 mol·dm^{-3}. The polymerization was carried out in a capped vial at 110 °C under microwave irradiation (Fig. 1). The polymerization conditions and properties of the resulting polymers are listed in Table 2. The optimal polymerization times t_p were determined by a kinetic study, which is described in the supplemental information. The loss of MeOx and increasing molar mass over time are shown in Fig. S1.

Upon reaction completion, it was quenched by 25% wt. tetramethylammonium hydroxide (TMAH) in methanol and that was left stirring overnight at room temperature. The mixture was filtered and the polymer was precipitated into cold diethyl ether and filtered out. The final polymer was dried under reduced pressure.

^1H NMR of P1-P3 (400 MHz, D$_2$O, HMDSO), δ (ppm): 2.10, 3.40, 4.63 (2 H), 7.10 (1 H), 7.35 (1 H), 7.52 (1 H) – spectrum shown in Fig. S2.

3.2. Synthesis and characterization of 5,10,15,20-tetra(thien-2-yl) porphyrin (2TTP) and 5,10,15,20-tetra(thien-3-yl)porphyrin (3TTP)

The reaction was carried out by a modified procedure according to Refs [30,31]. To the refluxing propionic acid (160 mL), 2-thiophenecarboxaldehyde (45 mmol, 4.2 mL, for the synthesis of 2TTP) or 3-thiophenecarboxaldehyde (45 mmol, 4.2 mL, for the synthesis of 3TTP) and pyrrole (45 mmol, 3.1 mL) were added, and then, the mixture was refluxed for 30 min. After cooling to room temperature, the dark brown crystals were filtered out. The crystals were washed with methanol, recrystallized twice from a chloroform/methanol mixture and dried under vacuum. The yield of 2TTP (Fig. 2 **up**) was 0.95 g (13%), and the yield for 3TTP (Fig. 2 **down**) was 1.66 g (23%) [32].

TLC was used to confirm the purities of the samples. Toluene and hexane (1:1) were used as the mobile phase. There was only one spot in both cases with a similar retention factor RF (for 2TTP – RF = 0.41 and for 3TTP – RF = 0.45).

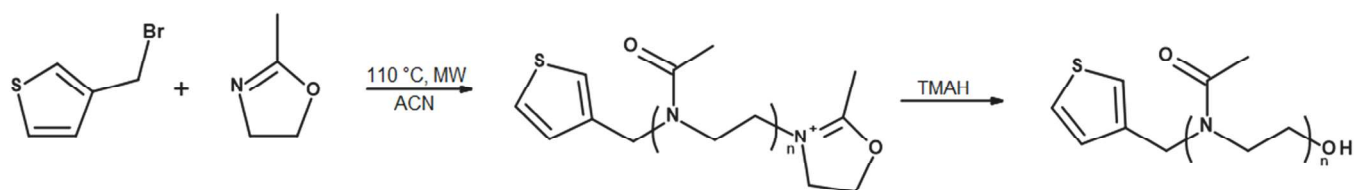2TTP: ^1H NMR (400 MHz, THF-d8, HMDSO), δ (ppm): − 2.60 (s,

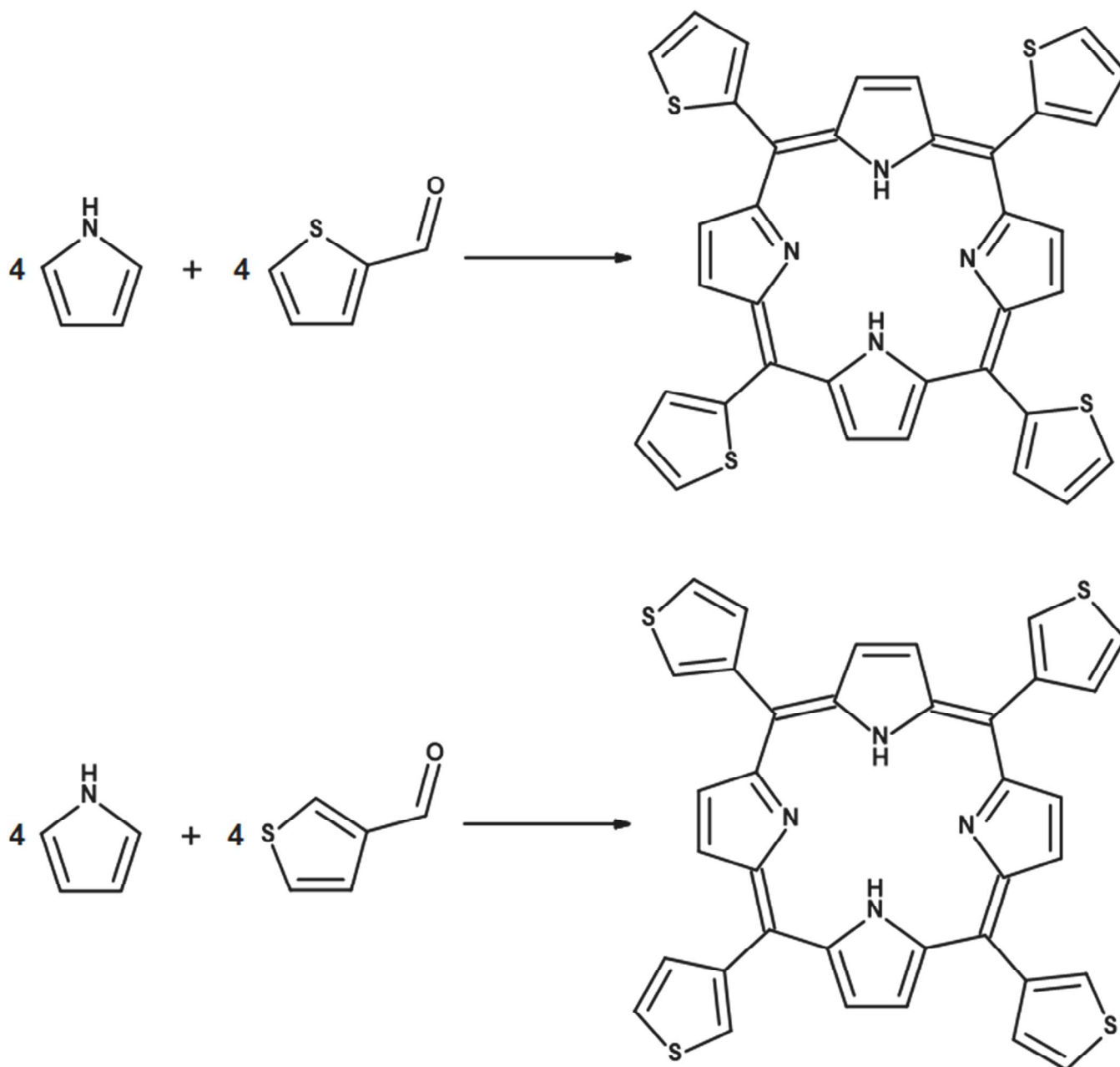**Fig. 1.** Synthetic scheme of poly(2-methyl-oxazoline).

Fig. 2. Synthetic schemes of the prepared porphyrin derivatives 2TTP (up) and 3TTP (down).

2 H), 7.51 (dd, 4 H), 7.93 (dd, 4 H), 7.98 (dd, 4 H), 9.01 (s, 8 H) – spectrum shown in Fig. S5. Elemental analysis (theoretical/found): C 67.71/67.14 ± 0.01%; H 3.45/3.54 ± 0.04%, N 8.78/7.67 ± 0.16%, S 20.06/19.85 ± 0.03%. MALDI-TOF: $m/z = 638.07$ (M). ^{13}C NMR (400 MHz, DCOOD+THF-d8 1:1), δ (ppm): 147.29, 143.70, 139.91, 137.81, 130.71, 129.09, 116.66 - spectrum shown in Fig. S7 **up**.

3TTP: ^{1}H NMR (400 MHz, THF-d8, HMDSO), δ (ppm): − 2.66 (s, 2 H), 7.86 (dd, 4 H), 7.99 (dd, 4 H), 8.13 (s, 4 H), 8.94 (s, 8 H) – spectrum shown in Fig. S6. Elemental analysis (theoretical/found): C: 67.71/66.62 ± 0.12%, H: 3.45/3.58 ± 0.00%, N: 8.78/8.26 ± 0.11%, S: 20.06/20.17 ± 0.16%. MALDI-TOF $m/z = 638.13$ (M). ^{13}C NMR (400 MHz, DCOOD+THF-d8 1:1), δ (ppm): 146.54, 141.95, 137.24,

136.29, 129.64, 128.20, 117.80 - spectrum shown in Fig. S7 down.

3.3. Electropolymerization and characterization of 5,10,15,20-tetra (thien-2-yl) porphyrin (2TTP) and 5,10,15,20-tetra(thien-3-yl) porphyrin (3TTP)

First, 1.3 mM (12 mg) of 5,10,15,20-tetra(thien-2yl) porphyrin (2TTP) or 5,10,15,20-tetra(thien-3yl) porphyrin (3TTP) was dissolved in 4 mL of concentrated formic acid, with the formation of green and brown solutions, respectively. After the ultrasonication of a solution of 2TTP or 3TTP for 10 min, 0. 25 mM 1-methylimidazole in CH_2Cl_2 (10 mL) was added. The electropolymerization of 2TTP or 3TTP solutions was performed in a three-electrode cell (15 mL) with an AUTOLAB PGSTAT302N potentiostat. All measurements were performed at ambient temperature by cycling the potential 50 times between –1 and 1.85 V with a scan rate of 50 mV s^{-1}. The polymerization solution was purged with N_2 gas for 15 min prior to each electropolymerization. The solution was blanketed with N_2 during electropolymerization to protect it from atmospheric oxygen. The FTO or GC electrodes were tested as the working electrode (WE), while a Pt sheet and Ag wire served as the counter (CE) and reference electrodes (RE), respectively. After electropolymerization, the electrodes were washed with chloroform and stored in a desiccator. The conductive polymeric layers were named poly-2TTP and poly-3TTP.

3.4. Preparation of metal-complexed poly-3TTP

Four different metal cations were incorporated into the porphyrin core, which is found in the thin layer of poly-3TTP. Fe^{2+}, Co^{2+}, Cu^{2+} and Mn^{2+} were selected; thus, 1 M aqueous solutions of $FeCl_2$, $CoCl_2$, $CuCl_2$ and $MnCl_2$ were prepared, and the individual poly-3TTP electrodes were dipped into the solution of the corresponding metal for 24 h to chelate the particular metal cation into the porphyrin core.

3.5. Preparation of poly-3TTP-Fe/PMeOx

Poly(2-methyl-2-oxazoline) with a thiophene end group was covalently bound to the polymeric film of poly-3TTP-Fe. A drop of a solution of PMeOx was applied on the surface of poly-3TTP-Fe and dried in an oven. Three types of PMeOx differing in molar masses were tested. The covalent link between PMeOx and the poly-3TTP-Fe film was provided by a few cyclic voltammetry cycles. Such film is referred to as poly-3TTP-Fe/PMeOx.

3.6. Potentiometric testing of different sensing layers in the presence of H_2O_2

The testing electrode was immersed into solution of PBS and left to reach a stable potential. After that the solution of hydrogen peroxide was added starting from the smallest concentration, which is 50 nM. Fresh solution of hydrogen peroxide was prepared before each measurement. The maximum concentration of hydrogen peroxide was 10 μM. The change in the potential was recorded after complete reaching the equilibrium, which was obtained during 15 min. The potentiometric study was performed by using 6-chanel high input impedance (10^{10} Ω, Lawson Laboratories, Malvern, PA, USA).

3.7. Testing of poly-3TTP-Fe/PMeOx in the presence of catalase

Catalase from bovine liver (Sigma-Aldrich, Czech Republic) in the concentration of 110×10^{-6} units/L was dissolved in PBS solution and used for the detection of H_2O_2 by poly-3TTP-Fe/PMeOx sensing layer.

4. Results and discussion

4.1. Synthesis of porphyrin derivatives

Two derivatives of porphyrin with incorporated thiophene structures have been successfully synthesized. Namely, 5,10,15,20-tetra(thien-2-yl)porphyrin (2TTP) and 5,10,15,20-tetra(thien-3-yl)porphyrin (3TTP) were synthesized according to the abovementioned procedure. The yields of 2TTP and 3TTP were 13% and 23%, respectively. Their structures were confirmed by ^{1}H NMR, elemental analysis and MALDI-TOF. The structures were designed so that 2TTP offers 4 and 3TTP offers 8 positions for electropolymerization to form a thin homogeneous conductive layer.

4.2. Synthesis of α-(3-methyl)thiophene poly(2-methyl-2-oxazoline)

Poly(2-methyl-oxazoline) with a thiophene end group was successfully prepared with 3 different molar masses by microwave-assisted cationic ring opening polymerization. The chemical structure was proven by ^{1}H NMR and molar masses, and their distributions were determined by SEC. The values are listed in Table 2. The thiophene end group serves as a linker to the porphyrin-based layer. Such an arrangement creates a nonbiofouling barrier of the conductive porphyrin-based layer, and thus, it is prevented from plasma protein interactions.

4.3. Electrochemical deposition of the sensing layer

The electropolymerization of two monomers (2TTP and 3TTP) on two different supports was performed by applying cyclic voltammetry. Our first task was to determine the appropriate support for sensing layer deposition. For that purpose, FTO and GC were chosen. It is interesting to note that the nature of the support plays a crucial role in determining if the monomer could be deposited or not. The 3TTP monomer could not deposit on the FTO electrode; however, it was easily deposited on GC (Fig. 3b). The 2TTP monomer could be deposited on both supports (FTO or GC), and the cyclic voltammetry curves of the film deposition on the FTO support (for the 2TTP monomer) are presented in Fig. 3a. The cyclic voltammetry curves of 2TTP have two oxidation and two reduction peaks. The mechanism of the dimer formation proceeds via formation of dimer in the second position of C_α. The cyclic voltammetry curves of the 3TTP monomer have only one oxidation peak and one reduction peak. Moreover, the 3TTP monomer has a higher oxidation potential ($E_{ox} = 0.52$ V vs. Ag/AgCl) compared to the oxidation potential of 2TTP ($E_{ox} = 0.4$ V vs. Ag/AgCl). The higher oxidation potential of the 3TTP monomer is probably the reason why this monomer could not be deposited on the FTO support because the applied voltage was not enough to activate the FTO surface for monomer oxidation. We also observed that the difference between the oxidation and reduction potentials was similar for both monomers; however, with increasing deposition layers, the oxidation current increased almost 4 times for the 3TTP monomer and only 1.5 times for the 2TTP monomer. Such behaviour is connected with the fact that the 3TTP monomer has 8 positions for electropolymerization compared to the 2TTP monomer, which only has 4 positions. The appearance of the second oxidation/reduction peak for the 2TTP monomer is connected with the oxidation/reduction of the porphyrin ring, as was previously published in the literature [33,34].

Based on these results, it is concluded that the 3TTP monomer is more redox stable than the 2TTP monomer.

To further characterize the two polymer films (poly-2TTP and poly-3TTP), scanning electron microscopy (SEM) was applied. The SEM images (Fig. 3c and d) show that the surface of the deposited films is different. The poly-3TTP film has a rough surface compared to the poly-2TTP film. The SEM images of the bare FTO and GC electrodes are presented in SI Fig. S8 for comparison. It is obvious that GC as a supporting electrode is more suitable for our purpose than FTO because on
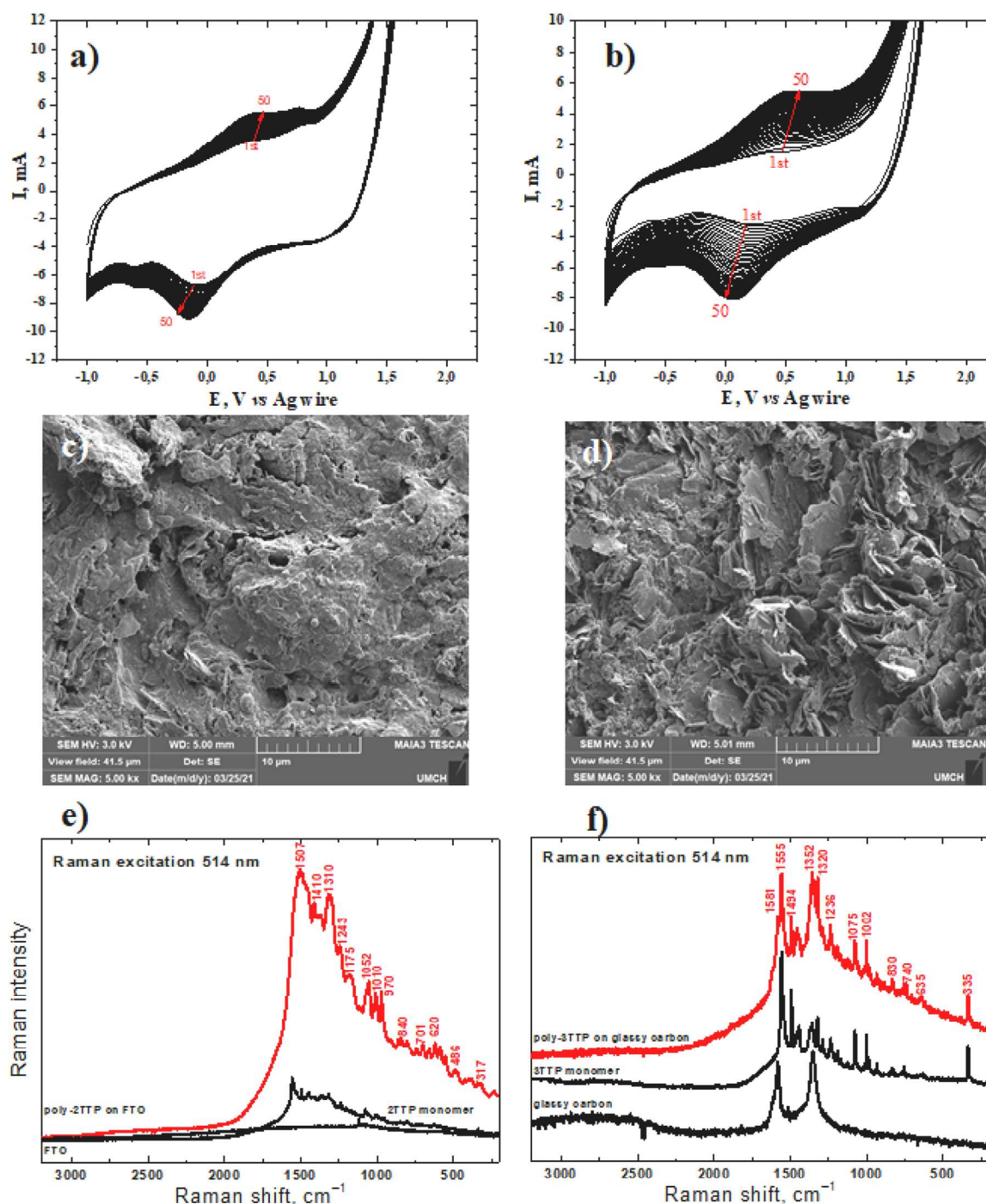
Fig. 3. Electropolymerization curves (**a** and **b**) of 5,10,15,20-tetra(thien-2yl) porphyrin (2TTP) and 5,10,15,20-tetra(thien-3yl) porphyrin (3TTP) on FTO and GC, respectively, in CH_2Cl_2 containing 5 M formic acid. SEM images of the obtained polymers (c and d) with a magnification 10 000x. Raman spectra (excitation laser of 514 nm) of poly-2TTP (e) electrochemically prepared on FTO and poly-3TTP (f) on GC. The spectra of 2TTP and 3TTP monomers are added for comparison.

such electrodes, the total surface area of the deposited poly-3TTP film is much higher.

The main purpose of this study is deposition of a thin sensing layer for the detection of ROS. The rough surface of poly-3TTP is favourable for the detection of ROS because it has a higher interface area than poly-2TTP (see SEM images, Fig. 3; and EIS Fig. 4). The nature of the in-terfaces (boundary region between two phases) predetermines the sensing ability of the constructed film (confirmed by EIS data). This is the second favourable point for the poly-3TTP film compared to the poly-2TTP film.

To confirm the formation of the polymer film, the Raman spectra were measured for monomers (2TTP and 3TTP) and compared with the final polymer films, as shown in Fig. 3e and f, respectively. The forma-tion of the polymer film was proven by the broadening and increasing Raman signals corresponding to monomers.

The stretching vibration of the pyrrole ring on the porphyrin mac-rocycle is observed at 1320 cm^{-1} for poly-3TTP and 1310 cm^{-1} for poly-2TTP, and its intensity is increased for the polymer film [35]. The characteristic Raman signals for the thiophene ring are located at wavelengths similar to those for porphyrin, which is why it is difficult to identify them. The orientation of porphyrin rings in the deposited polymer films was analysed by X-ray diffraction measurements and is
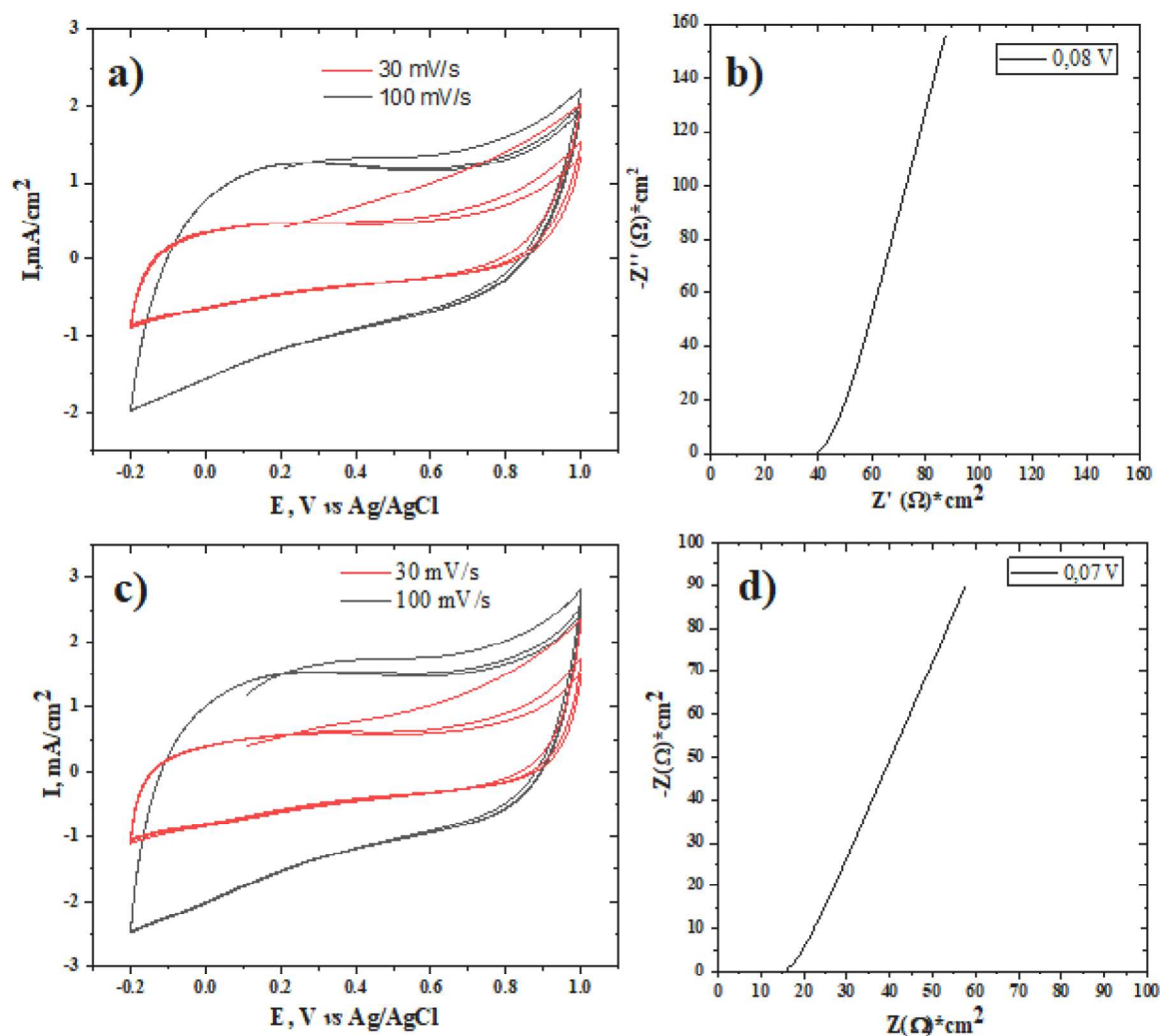
Fig. 4. Electrochemical cyclic voltammetry of poly-3TTP measured in PBS buffer (a) and (b) EIS of poly-3TTP measured in PBS at 0.08 V vs. Ag/AgCl (corresponding to V_{oc}); electrochemical cyclic voltammetry of poly-2TTP measured in PBS buffer (c) and (d) EIS of poly-2TTP measured in PBS at 0.07 V vs. Ag/AgCl (correspond to V_{oc}).

presented in SI Fig. S9 (black arrow). The peak located at $2\Theta = 16°$ corresponds to the distance between porphyrin rings. The intensity of the peak is higher for poly-2TTP than for poly-3TTP. This indicates that the porphyrin rings in poly-2TTP are organized better than those in poly-3TTP, probably because 2TTP offers only 4 while 3TTP offers 8 positions for electropolymerization. This result also confirms the observation by SEM, where a compact and smooth layer is observed for poly-2TTP and a rough surface is detected for poly-3TTP.

To choose the appropriate polymer (poly-3TTP or poly-2TTP) for sensing applications, electrochemical characterization in PBS solution was performed, particularly cyclic voltammetry (in the potential window from −0.2 to 1.0 V vs. Ag/AgCl reference electrode) and electrochemical impedance spectroscopy (EIS) measured at open circuit potential. Both polymeric films have similar cyclic voltammetry curves, as shown in Fig. 4a and c. However, the EIS measurements are different (Fig. 4b and d). Poly-3TTP has capacitive character of impedance data (an almost vertical behaviour at low frequencies) compared to the diffusion character of impedance for poly-2TTP. Such a difference could be explained by the porphyrin orientation in the deposited film, proven by XRD and SEM measurements. Moreover, neither film has a semicircle at high frequencies, meaning that the charge-transfer resistance at the interface is low, which reflects that poly-3TTP and poly-2TTP are reversible and return rapidly to the equilibrium value after a small perturbation. Based on electrochemical measurement results, poly-3TTP

is chosen for further investigation as a sensing layer (the interface has a capacitive nature).

Electrochemical sensors have attracted much attention from researchers in recent years due to their outstanding advantages, such as simplicity in instrumentation, real-time analyte detection in complex systems, high sensitivity and selectivity, rapid response, miniaturization, convenient operation procedures, and in vivo detection capability [36]. In recent years, a significant amount of electrochemical studies focused on detection or quantifying H_2O_2 in body fluids and presented in Table 1.

The electrochemical systems described for the determination of H_2O_2 are mostly amperometric [38,40–58], although differential pulse voltammograms [37] and potentiometric sensors [39] are also described for enzyme-based approaches. The electrochemical systems for the determination of H_2O_2 may be roughly divided into two categories depending on sensing species on the electrode: enzyme-based (with horseradish peroxidase, HRP) and enzyme-free (based on various transition metal-containing (nano)materials). The enzymatic electrodes are specific for hydrogen peroxide due to high substrate specificity of HRP, however have more limited lifetime due to denaturation/inhibition of the enzyme. Enzymatic electrodes can detect as low concentration as 100 nM [41], however the upper limit of response linearity is rarely above 1 mM [38]. Contrary to that, nonenzymatic electrodes are more robust, but have higher detection limit and linearity range shifted to

Table 1
Comparison of the electrochemical detection of H_2O_2 by different electrodes.

Sensor type	Chemistry	Linearity range	Reference
Enzymatic sensors			
Differential pulse voltammograms	Horseredish peroxidase (HRP)	200 nM – 0.281 mM	[37]
Amperometry	HRP-MIL-100(Cr)-B/GCE	0.5–3000 μM	[38]
Potentiometry	Os-PVP with HRP	1–150 μM	[39]
Amperometry	HRP on ultrathin titania layer-modified self-assembled gold electrode	1 μM – 0.76 mM	[40]
Amperometry	HRP on functionalized carbon buckypaper	100 nM – 0.5 mM	[41]
Enzyme free sensor			
Potentiometry	**Poly-3TTP-Fe/PMeOx**	**50 nM – 10 μM**	**This work**
Amperometry	AuPt/ZIF-8-rGO	100 nM – 18 mM	[42]
Amperometry	Mn@FeNi-S/GO	25 μM – 0.125 mM	[43]
Amperometry	3D N-Co-CNT@NG	2 μM – 7.449 mM	[44]
Amperometry	CoS	5 μM – 14.82 mM	[45]
Amperometry	Co$_3$N NW/TM	2 μM – 28 mM	[46]
Amperometry	Fe$_3$N-Co$_2$/CC	150 nM – 8 mM	[47]
Amperometry	RGO-Pt/GCE	500 μM – 3.47 mM	[48]
Amperometry	CoP NWs	1 μM – 12 mM	[49]
Amperometry	PPy-Co NCs	20 μM – 1 mM	[50]
Amperometry	CoTPP/RGO	100 nM – 2.4 mM	[51]
Amperometry	hemin-modified gold electrod	5 mM	[52]
Amperometry	Au-Pd bimetallic nanocubes	5 nM – 3.5 mM	[53]
Amperometry	Pt@PAA(DS)/aSPCEs	0.1–10 μM	[54]
Amperometry	CeO$_2$-modified Pt/C catalyst inks	0.01–30 mM	[55]
Amperometry	MnO$_2$ ultrathin nanosheets	5 μM – 3.5 mM	[56]
Amperometry	CoHCF Nanoparticles	8 μM –7.5 mM	[57]
Amperometry	MWCNTs-POMAF	1.0 – 6.0 μM	[58]

higher concentrations of hydrogen peroxide. Generally, concentration-response linearity range is mostly around 3 orders of magnitude wide.

The detection limit and position of linearity range greatly depends on the electrode material. With the advancement of nanotechnologies, various nanomaterials have been designed to detect and monitor reactive oxygen species. Most systems utilize cobalt as sensing metal [44–47, 49–51,57], where the detection limit is in micromolar range and the response is linear up to several to tens of millimolar concentrations. Similar behavior was described for platinum-based materials [42,48,54, 55]. Few studies utilize other metals such as iron, nickel, manganese, molybdenum, gold, cerium or palladium [42,43,47,55,56,58].

Currently, the detection of ROS by nonenzymatic sensors has gained attention in practical applications compared with enzymatic sensors [36,59]. In this regard, a series of transition metal porphyrins have been prepared. For that purpose, electrochemically deposited poly-3TTP films on GC were immersed in the corresponding solutions of metals for 24 h. Porphyrins are excellent metal chelators, and poly-3TTP-Cu, poly-3-TTP-Fe, poly-3TTP-Co, and poly-3TTP-Mn were obtained after the interaction of the corresponding metal ions with the porphyrin film. The presence of metal ions in the porphyrin was confirmed by high-resolution core-level XPS measurements. The deconvoluted XPS spectrum of poly-3TTP of high-resolution core-level N 1 s has two peaks corresponding to oxidized (=N-, 400 eV) and reduced (-NH-, 401 eV) pyrrole units in porphyrin. The deconvoluted XPS spectrum of poly-3TTP with the metal changes with the appearance of a new peak

and depletion of the peaks corresponding to the original pyrrole units in porphyrin. This new peak corresponds to nitrogen complexed with the corresponding metals. The presence of the corresponding metal was also confirmed by XPS spectra and is presented in SI Fig. S11.

Hydrogen peroxide (H_2O_2) is an eminent biomarker in pathogenesis. In biological systems, an adequate amount of H_2O_2, from 1 to 700 nM, is essential for intracellular signal transduction, cell proliferation, protein synthesis, and controlling living activities [38]. The concentration of H_2O_2 exceeding the permissible limit > 700 nM is associated with cell damage, and in inflamed tissues, orders of magnitude higher concentrations are present. Based on this knowledge, the assembled poly-3TTP-Me sensing layers were tested in the H_2O_2 concentration range from 50 nM to 100 μM.

A commonly employed analytical method for ROS detection is amperometry. However, to measure ROS concentrations in vivo (orthopedic implants), a less energy-consuming method is required. Therefore, potentiometric detection was chosen as an appropriate method for ROS detection.

To study the dependence of the potential vs·H_2O_2 concentration on poly-3TTP-metal films, the bare poly-3TTP electrodes were measured in phosphate buffered saline (PBS) solution (the result is presented in SI Fig. S12). It is obvious that the poly-3TTP film does not interact with H_2O_2. However, when Cu or Fe ions were incorporated into poly-3TTP layers, we observed the potentiometric sensitivity of these films (the results of the measurements are presented in Fig. 5a and b). The potentiometric measurement was performed on a high input impedance potentiostat. Phosphate buffer solution (PBS) at a pH of 7 was used as an electrolyte, and hydrogen peroxide was added at each concentration after 15 min

The potentiometric detection of H_2O_2 vs. concentration is presented in Fig. 5a and Fig. 5b for poly-3TTP-Cu (n = 3) and poly-3TTP-Fe (n = 3), respectively. The concentration of H_2O_2 is in the range from 50 nM to 100 μM. The sensitivity of the poly-3TTP-Cu and poly-3TTP-Fe is changing linearly in the low concentration range, as shown in Fig. 5a and Fig. 5b. It obvious that at low hydrogen peroxide concentrations the sensitivity of the developed films is better, with a linear range from 50 nM to 1 μM and a slope of 13.54 ± 0.5 mV/decade (R^2 = 0.9939) for poly-3TTP-Cu, and with a linear range from 50 nM to 10 μM and a slope of 31.75 ± 0.5 mV/decade (R^2 = 0.9995) for poly-3TTP-Fe are calculated. From the slope value and linear concentration range it is concluded that poly-3TTP-Fe has superior performance compared to poly-3TTP-Cu sensing film. We explain the decrease of the sensitivity for higher concentration of hydrogen peroxide by the fact that molecules of hydrogen peroxide, which reacts with Fe or Cu ions in poly-3TTP (by the reaction presented below), must diffuse into inner layers of poly-3TTP-Fe or poly-3TTP-Cu. Superior performance of poly-3TTP-Fe is due to the structure of the film (roughness of the surface), which is confirmed by SEM and XRD measurements. Therefore, it is concluded that poly-3TTP-Fe is more sensitive to hydrogen peroxide than poly-3TTP-Cu.

Similar behaviour was reported in the literature for amperometric detection of hydrogen peroxide by Mn@FeNi-S/GO nanocomposites (see Table 1) [43]. The advantage of our potentiometric method for hydrogen peroxide detection is simplicity of sensing layer preparation, and high sensitivity of the poly-3TTP-Fe film at low, and most importantly, relevant concentration of hydrogen peroxide for bio-medical application.

We proposed the interaction mechanism of the poly-3TTP-Fe sensing layer with H_2O_2 as follows:

poly-3TTP-Fe$^{(2+)}$ + H_2O_2 → poly-3TTP-Fe$^{(3+)}$ + H_2O + 1/2 O_2
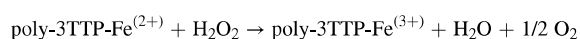
The reversibility of sensor's response was checked three times giving the same potential vs hydrogen peroxide concentration response.

On the other hand, the poly-3TTP-Co and poly-3TTP-Mn sensing layers were not sensitive to H_2O_2, as presented in SI Fig. S13. We explained such behaviour (of these two sensing layers) by the method of
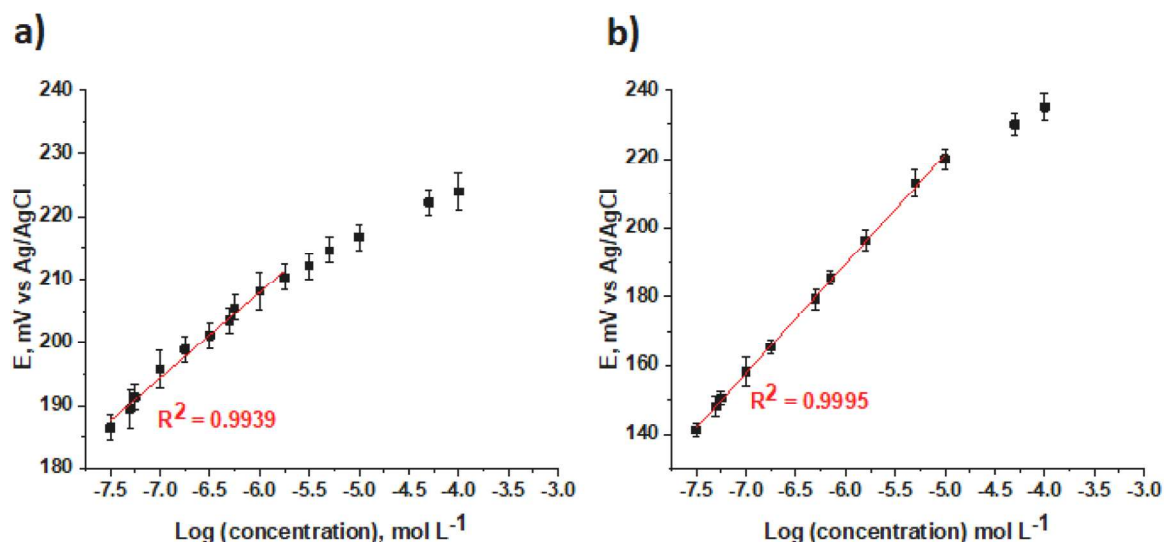
Fig. 5. (a) Potentiometric response of the (potential vs. concentration) poly-3TTP-Cu sensing layer and (b) poly-3TTP-Fe sensing layer in PBS (pH = 7).

detection (potentiometric) that was applied. In the literature, the most applied method for H_2O_2 detection is amperometric when Co and/or Mn ions are used, see Table 1 [36,43,60].

It is concluded that poly-3TTP-Cu and/or poly-3TTP-Fe sensing layers are suitable for the detection of H_2O_2. However, based on the slope value, it was decided to continue to work only with the poly-3TTP-Fe sensing layer and to coat it with a nonbiofouling layer.

4.4. Covalent deposition of poly(2-methyl-oxazoline) as nonbiofouling layer and measurement in biologically relevant environment

The nonbiofouling property of a surface is crucial to prevent interactions between bulky proteins and an engineered surface. In this work, a poly(2-methyl-oxazoline) (PMeOx) thin film is used as a non-biofouling layer. Three polymers with different molar masses were synthesized (as presented above, see Table 2) to find the optimal chain length of PMeOx to prevent protein absorption while still able to be penetrable for ROS. The XPS method was used to study the deposition of PMeOx on top of the poly-3TTP-Fe sensing layer (see SI, Table S2). The XPS data clearly showed that low molecular weight PMeOx does not form a layer on top of poly-3TTP-Fe. However, the highest molecular weight PMeOx formed a thin layer, which was detected by XPS. This tendency is explained by the method of PMeOx deposition: a solution of PMeOx was drop cast deposited on top of poly-3TTP-Fe and dried in an oven. After that, we applied a few cyclic voltammetry cycles in PBS solution to fix the PMeOx layer. We assumed that PMeOx with lower molecular weight chains could be dissolved in PBS before the cyclic voltammetry method is applied and/or during it. We must emphasize

that direct electrochemical deposition of PMeOx by different methods was not successful.

The final electrode was named poly-3TTP-Fe/PMeOx and was tested in the presence of bovine serum albumin, or catalase and bovine serum albumin (n = 3) to understand whether the nonbiofouling property of the PMeOx layer works. The results of the potentiometric detection of H_2O_2 are presented in Fig. 6a (with albumin) and Fig. 6b (with albumin and catalase).

Similar to the potentiometric results for the poly-3TTP-Fe (Fig. 5b) the sensitivity of the poly-3TTP-Fe/PMeOx response to hydrogen peroxide linearly changed with the concentration, see Fig. 6a. The sensitivity of the poly-3TTP-Fe/PMeOx in the presence of albumin as the most bioenvironment-relevant condition is linearly changed with the broad range of hydrogen concentration (from 50 nM to 100 μM) and one linear regression is used (see Fig. 6a). Moreover, the presence of albumin in the solution did not block the surface of the sensing layer due to the presence of PMeOx (Fig. 6a). The slope is 12.84 ± 0.5 mV/decade (R^2 = 0.9920). The biologically relevant concentration of hydrogen peroxide in blood is from 1 μM to 5 μM. If the concentration of hydrogen peroxide is higher than 5 μM, it could be the signal of inflammation process. That is why the poly-3TTP-Fe/PMeOx was tested in the concentration range from 50 nM to 10 μM and in the presence of catalase.

In the literature it is published that the measurement of hydrogen peroxide in plasma and/or in the blood is highly complicated by a very short half-life of peroxide in the biological systems (due to the presence of catalase in blood and pathologically also in some cases due to bacterial catalase production in infects). The concentration of catalase in the blood is ca 110 megaunits per liter [61], therefore, it was suggested to investigate the sensing performance of poly-3TTP-Fe/PMeOx towards hydrogen peroxide in the presence of catalase of this activity, and the results are present in Fig. 6b. The sensitivity of poly-3TTP-Fe/PMeOx film towards hydrogen peroxide in the concentration range from 50 nM to 10 μM is even improved in the presence of catalase, the slope value is 44.4 ± 2.2 mV/decade (R^2 = 0.9938, n = 3) compared to the measurements without catalase (see Fig. 6a and Fig. 6b respectively). One of the possible explanation of the improvement of the sensitivity of the sensing layer poly-3TTP-Fe/PMeOx with addition of catalase to the testing solution is by the fact that there is a redox communication between catalase and the sending layer, direct or indirect via more reactive ultra-short half-life ROS intermediates such as ·OH radicals produced by catalase as side products from hydrogen peroxide to some extent (catalase possesses some minor peroxidase activity and vice versa). It is concluded (based on these measurements) that the
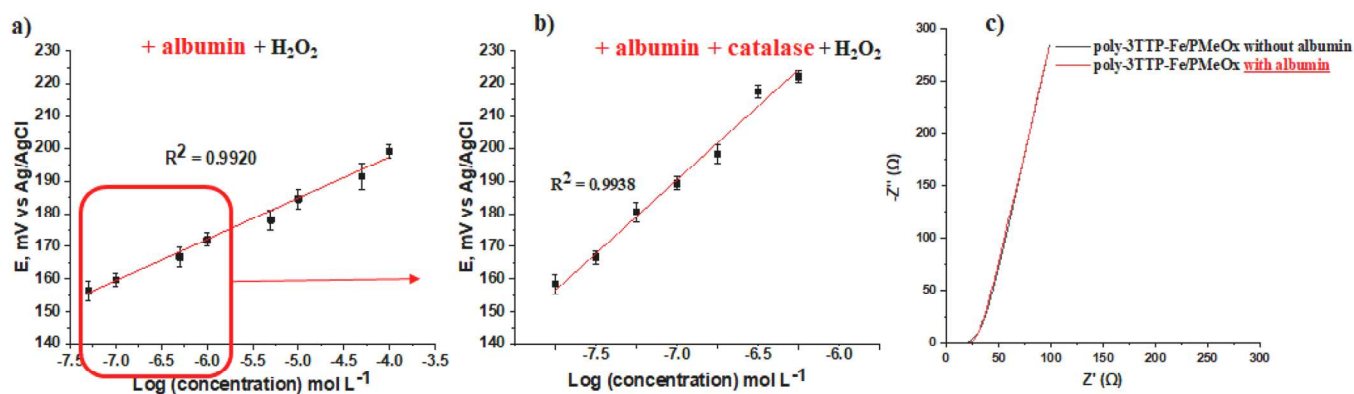
Table 2
The polymerization conditions for syntheses of PMeOx and their characteristics.

No.	M_{th}[a] (kDa)	t_P (min)	n_M/n_I	m_I (mg)	M_n[b] (kDa)	M_n[c] (kDa)	$Đ$[c]
P1	1	28	11.7	177	1.5	1.5	1.15
P2	2	56	23.5	89	3.0	2.4	1.24
P3	5	140	58.7	53	4.6	5.4	1.24

[a] Theoretical molecular weight calculated by $M_{th} = \frac{n_I}{m_M}$ where n_I stands for amount of substance of initiator and m_M for mass of monomer; [b] Number average of molar mass M_n determined by ^{1}H NMR [c] Number average of molar mass M_n and dispersity $Đ$ were determined by SEC, chromatograms shown in Fig. S3.

Fig. 6. Potentiometric detection of H_2O_2 in PBS (pH = 7) for the poly-3TTP-Fe/PMeOx sensing layer in the presence of albumin (a) and poly-3TTP-Fe/PMeOx in the presence of albumin with catalase (b). EIS of poly-3TTP-Fe/PMeOx before and after measurement in albumin.

poly-3TTP-Fe/PMeOx sensing film developed by us is promising for accurate and sensitive online in situ monitoring of hydrogen peroxide.

Additionally, the EIS data for poly-3TTP-Fe/PMeOx before and after measurements with albumin proved that albumin was not attached to the PMeOx surface (Fig. 6c), and the spectra were similar. The measurements in the presence of bovine serum albumin, catalase and hydrogen peroxide is accurately estimate the performance of the developed sensor in biologically relevant environment. As reported in the literature, the concentration measurements of hydrogen peroxide in plasma, or in cells is complicated by the short half-life of hydrogen peroxide in the biological systems (due to the presence of enzymes, which decompose hydrogen peroxide) [62,63].

The constructed poly-3TTP-Fe/PMeOx sensor is stable for at least one month. Moreover, when a fresh solution of PBS was applied and the poly-3TTP-Fe/PMeOx sensor was tested again for H_2O_2 detection, the sensor performance was reproduced. We explain the stability over time of the poly-3TTP-Fe/PMeOx sensor to detect H_2O_2 by the ability of polyporphyrin to reduce Fe^{3+} ions back to Fe^{2+}. Also, the nonbiofouling layer protect sensing layer of poly-3TTP-Fe. These results indicate that poly-3TTP-Fe/PMeOx could be a promising sensing film for accurate and sensitive online monitoring of hydrogen peroxide.

4.5. Selectivity of poly-3TTP-Fe/PMeOx sensor

To prove that poly-3TTP-Fe/PMeOx is selectively responsive towards
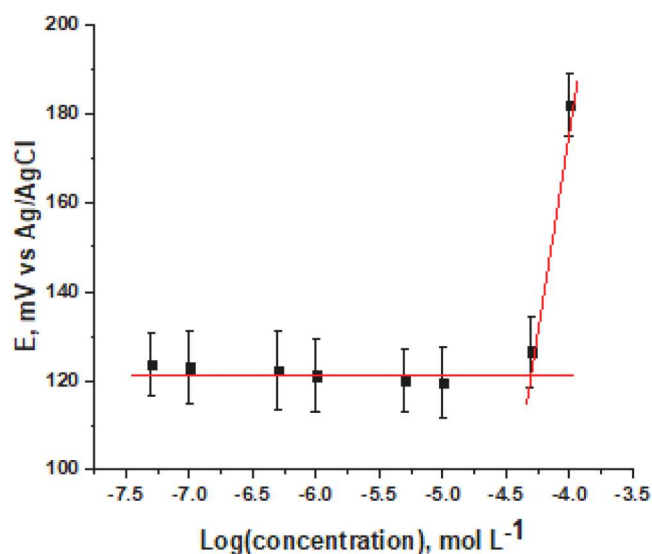
Fig. 7. Potentiometric detection of ClO⁻ ions by poly-3TTP-Fe/PMeOx.

H_2O_2, it was decided to measure potentiometric detection of ClO⁻ as a hallmark of bacterial infection at relevant concentrations, and the results are presented in Fig. 7.

We did not observe the response of poly-3TTP-Fe/PMeOx towards ClO⁻ in the concentration range from 50 nM to 10 μM, as presented in Fig. 7. Only for the last two concentrations was poly-3TTP-Fe/PMeOx sensitive; however, such a high concentration is not relevant for bio-applicable purposes because in living cells, the concentration of ClO⁻ is in the range from 50 nM to 5 μM [64,65].

Based on this result, it is concluded that the assembly of our poly-3TTP-Fe/PMeOx sensing layer is suitable for the detection of H_2O_2, and the presence of ClO⁻ will not deteriorate its performance.

5. Conclusion

In summary, the present work reports the method of assembling a sensing layer based on electrochemically deposited polyporphyrin (3TTP) incorporating different coordinated metals (Cu, Fe, Co and Mn) protected by a nonbiofouling thin film composed of poly(2-methyl-2-oxazoline). The assembled poly-3TTP-Fe/PMeOx film was characterized by Raman spectroscopy, XPS, cyclic voltammetry and EIS. It was demonstrated that the poly-3TTP-Fe/PMeOx film has the sensing ability to detect H_2O_2 by a potentiometric method in a biologically relevant concentration range (from 0.05 μM to 10 μM). Moreover, the poly-3TTP-Fe/PMeOx sensing layer is selective for H_2O_2 and does not work for another ROS, ClO⁻ ions. We also have shown that our potentiometric sensor shows a rapid response to hydrogen peroxide even in the presence of interfering bovine serum albumin as a model serum protein and the sensor has improved performance in the presence of catalase in biological relevant concentration. The designed potentiometric sensor is stable over time.

Supporting information

Supporting Information is available: Kinetic study of polymerization of 2-methyl-2-oxazoline initiated by 3-(bromomethyl)thiophene; Characterization of α-thiophene-ω-hydroxy poly(2-methyl-2-oxazoline) by ^{1}H NMR spectroscopy; SEC chromatograms of prepared polymers; Absorption spectra of 2TTP and 3TTP; ^{1}H NMR spectrum of 2TTP; ^{1}H NMR spectrum of 3TTP; ^{13}C NMR spectrum of 3TTP; SEM image of the surface of FTO glass(left) and GC (right). Magnification: 10 000 times; X-ray diffraction of poly(3TTP) and poly(2TTP) on GC support, the spectrum of GC is added for comparison; Atomic concentration of metals in poly-3TTP; XPS spectra of poly-3TTP and its composite with metals; XPS spectra of measured of metals in poly-3TTP; Open circuit potential of bare poly-3TTP electrode (n = 3) measured in PBS solution with H_2O_2; Potentiometric detection of H_2O_2 in PBS (pH 7) for poly-3TTP-Cu sensing layer, and poly-3TTP-Fe sensing layer; Potentiometric

detection of H_2O_2 in PBS (pH 7) for poly-3TTP-Mn sensing layer and poly-3TTP-Co sensing layer; Atomic concentration of N in different samples.

Funding sources

Author contributions

The manuscript was written through contributions of all authors. All authors have given approval to the final version of the manuscript.

Declaration of Competing Interest

The authors declare the following financial interests/personal relationships which may be considered as potential competing interests: Martin Hruby reports financial support was provided by Czech Science Foundation, 21–01090S. Elena Tomsik reports financial support was provided by Czech Health Research Council, NU20–06–00424.

Acknowledgment

Appendix A. Supporting information

Supplementary data associated with this article can be found in the online version at doi:10.1016/j.snb.2022.131827.

References

[1] C. Lei, P. Wilson, C. Lekakou, Effect of poly(3,4-ethylenedioxythiophene) (PEDOT) in carbon-based composite electrodes for electrochemical supercapacitors, J. Power Sources 196 (18) (2011) 7823–7827.

[2] C. Zuliani, V.F. Curto, G. Matzeu, K.J. Fraser, D. Diamond, Properties and Customization of Sensor Materials for Biomedical Applications, in: S. Hashmi, G. F. Batalha, C.J. Van Tyne, B. Yilbas (Eds.), Comprehensive Materials Processing, Elsevier, Oxford, 2014, pp. 221–243.

[3] S. Kirchmeyer, K. Reuter, Scientific importance, properties and growing applications of poly(3,4-ethylenedioxythiophene), J. Mat. Chem. 15 (21) (2005) 2077–2088.

[4] N. Rozlosnik, New directions in medical biosensors employing poly(3,4-ethylenedioxy thiophene) derivative-based electrodes, Anal. Bioanal. Chem. 395 (3) (2009) 637–645.

[5] V.S. Vasantha, S.-M. Chen, Electrocatalysis and simultaneous detection of dopamine and ascorbic acid using poly(3,4-ethylenedioxy)thiophene film modified electrodes, J. Electroanal. Chem. 592 (1) (2006) 77–87.

[6] J. Park, H.K. Kim, Y. Son, Glucose biosensor constructed from capped conducting microtubules of PEDOT, Sens. Actuator B-Chem. 133 (1) (2008) 244–250.

[7] Y.H. Xiao, C.M. Li, M.L. Toh, R. Xue, Adenosine 5′-triphosphate incorporated poly (3,4-ethylenedioxythiophene) modified electrode: a bioactive platform with electroactivity, stability and biocompatibility, J. Appl. Electrochem. 38 (12) (2008) 1735–1741.

[8] C.C. Negut, R.-I. Stefan - van Staden, J.F. van Staden, Porphyrins-as active materials in the design of sensors. An overview, ECS J. Solid State Sci. Technol. 9 (5) (2020), 051005.

[9] C.-Z. Li, S. Alwarappan, W. Zhang, N. Scafa, X. Zhang, Metallo protoporphyrin functionalized microelectrodes for electrocatalytic sensing of nitric oxide, Am. J. Biomed. Sci. 1 (3) (2009) 274–282.

[10] C. Sanchez-Cano, M. Carril, Recent developments in the design of non-biofouling coatings for nanoparticles and surfaces, Int. J. Mol. Sci. 21 (3) (2020) 1007.

[11] I. Banerjee, R.C. Pangule, R.S. Kane, Antifouling coatings: recent developments in the design of surfaces that prevent fouling by proteins, bacteria, and marine organisms, Adv. Mat. 23 (6) (2011) 690–718.

[12] M. Mittal, M.R. Siddiqui, K. Tran, S.P. Reddy, A.B. Malik, Reactive oxygen species in inflammation and tissue injury, Antioxid. Redox Signal. 20 (7) (2014) 1126–1167.

[13] O. Takeuchi, S. Akira, Pattern recognition receptors and inflammation, Cell 140 (6) (2010) 805–820.

[14] D. Lebeaux, J.-M. Ghigo, C. Beloin, Biofilm-related infections: bridging the gap between clinical management and fundamental aspects of recalcitrance toward antibiotics, Microbiol. Mol. Biol. Rev. 78 (3) (2014) 510–543.

[15] V.J. Thannickal, B.L. Fanburg, Reactive oxygen species in cell signaling, Am. J. Physiol. -Lung Cell. Mol. Physiol. 279 (6) (2000) L1005–L1028.

[16] G.R. Buettner, Superoxide dismutase in redox biology: the roles of superoxide and hydrogen peroxide, Anticancer Agents Med. Chem. 11 (4) (2011) 341–346.

[17] W. Dröge, Free radicals in the physiological control of cell function, Physiol. Rev. 82 (1) (2002) 47–95.

[18] S. Pendyala, V. Natarajan, Redox regulation of Nox proteins, Respir. Physiol. Neurobiol. 174 (3) (2010) 265–271.

[19] M. Saran, W. Bors, Oxygen radicals acting as chemical messengers: a hypothesis, Free Radic. Res. Commun. 7 (3–6) (1989) 213–220.

[20] C.R. Arciola, D. Campoccia, L. Montanaro, Implant infections: adhesion, biofilm formation and immune evasion, Nat. Rev. Microbiol. 16 (7) (2018) 397–409.

[21] R.J.C. McLean, J.S. Lam, L.L. Graham, Training the biofilm generation–a tribute to J. W. Costerton, J. Bacteriol. 194 (24) (2012) 6706–6711.

[22] A. Al-Ahmad, M. Wiedmann-Al-Ahmad, J. Faust, M. Bächle, M. Follo, M. Wolkewitz, et al., Biofilm formation and composition on different implant materials in vivo, J. Biomed. Mater. Res. Part B: Appl. Biomat. 95B (1) (2010) 101–109.

[23] S. Movafagh, S. Crook, K. Vo, Regulation of hypoxia-inducible factor-1a by reactive oxygen species: new developments in an old debate, J. Cell. Biochem. 116 (5) (2015) 696–703.

[24] N.V. Iyer, L.E. Kotch, F. Agani, S.W. Leung, E. Laughner, R.H. Wenger, et al., Cellular and developmental control of O_2 homeostasis by hypoxia-inducible factor 1 alpha, Genes Dev. 12 (2) (1998) 149–162.

[25] K. Akong-Moore, O.A. Chow, M. von Köckritz-Blickwede, V. Nizet, Influences of chloride and hypochlorite on neutrophil extracellular trap formation, PLoS One 7 (8) (2012) e42984-e.

[26] R. Matsuoka, M. Igarashi, T. Kondo, T. Aikawa, M. Yuasa, Biomimetic antithrombogenic electrochemical superoxide anion radical sensor, J. Electrochem. Soc. 161 (6) (2014) B163–B166.

[27] R. Matsuoka, T. Kondo, M. Yuasa, Superoxide anion radical sensor using gc electrode modified with heparin/PEDOT and polymerized iron porphyrin, ECS Trans. 50 (12) (2013) 369–376.

[28] R. Matsuoka, S. Kobayashi, A. Nakagawa, S. Aoyagi, T. Aikawa, T. Kondo, et al., A reactive oxygen/nitrogen species sensor fabricated from an electrode modified with a polymerized iron porphyrin and a polymer electrolyte membrane, Anal. Sci. 33 (8) (2017) 911–915.

[29] M. Cuartero, G.A. Crespo, All-solid-state potentiometric sensors: a new wave for in situ aquatic research, Curr. Opin. Electrochem. 10 (2018) 98–106.

[30] P. Bhyrappa, P. Bhavana, Meso-tetrathienylporphyrins: electrochemical and axial ligation properties, Chem. Phys. Lett. 349 (5) (2001) 399–404.

[31] Y. Guo, X. Hao, Y. Tao, C. Zhang, H. Cheng, Preparation, characterizations and electrochromic properties of copolymers containing 5, 10, 15, 20-tetra(thienyl) porphyrin and thiophene derivatives, Synth. Met. 258 (2019), 116202.

[32] P. Betoni Momo, C. Pavani, M.S. Baptista, T.J. Brocksom, Thiago, K. de Oliveira, Chemical transformations and photophysical properties of meso-tetrathienyl-substituted porphyrin derivatives, Eur. J. Org. Chem. 21 (2014) 4536–4547.

[33] A.R. Antonangelo, K.C.M. Westrup, L.A. Burt, C.G. Bezzu, T. Malewschik, G. S. Machado, et al., Synthesis, crystallographic characterization and homogeneous catalytic activity of novel unsymmetric porphyrins, RSC Adv. 7 (80) (2017) 50610–50618.

[34] T.T.H. Tran, M.-R. Gan, Y.-P. Tzeng, H. Shaw, T.K.A. Hoang, M.-Y. Kuo, et al., Experimental and computational study on the electrochemistry of meso-tetrasubstituted porphyrins: effects of resonance and inductive substituents, J. Electroanal. Chem. 815 (2018) 40–46.

[35] M. Aydin, DFT and Raman spectroscopy of porphyrin derivatives: tetraphenylporphine (TPP), Vib. Spectrosc. 68 (2013) 141–152.

[36] S. Zhao, G. Zang, Y. Zhang, H. Liu, N. Wang, S. Cai, et al., Recent advances of electrochemical sensors for detecting and monitoring ROS/RNS, Biosens. Bioelectron. 179 (2021), 113052.

[37] M. Feizabadi, A. Soleymanpour, H. Faridnouri, D. Ajloo, Improving stability of biosensor based on covalent immobilization of horseradish peroxidase by γ-aminobutyric acid and application in detection of H_2O_2, Int. J. Biol. Macromol. 136 (2019) 597–606.

[38] H. Dai, W. Lu, X. Zuo, Q. Zhu, C. Pan, X. Niu, J. Liu, H.L. Chen, X. Chen, A novel biosensor based on boronic acid functionalized metal-organic frameworks for the determination of hydrogen peroxide released from living cells, Biosens. Bioelectron. 95 (2017) 131–137.

[39] D.T.V. Anh, W. Olthuis, P. Bergveld, Hydrogen peroxide detection with improved selectivity and sensitivity using constant current potentiometry, Sens. Actuator B-Chem. 91 (1–3) (2003) 1–4.

[40] Q.Y. Cao, W.Y. Zhou, Immobilization of horseradish peroxidase on a biocompatible titania layer–modified gold electrode for the detection of hydrogen peroxide, Anal. Lett. 39 (14) (2006) 2725–2735.

[41] S. Chatterjee, A.C. Chen, Functionalization of carbon buckypaper for the sensitive determination of hydrogen peroxide in human urine, Biosens. Bioelectron. 35 (1) (2012) 302–307.

[42] T. Zhang, Y. Xing, Y. Song, Y. Gu, X. Yan, N. Lu, H. Liu, Z. Xu, H. Xu, Z. Zhang, M. Yang, AuPt/MOF–graphene: a synergistic catalyst with surprisingly high peroxidase-like activity and its application for H_2O_2 detection, Anal. Chem. 91 (2019) 10589–10595.

[43] S. Manavalan, J. Ganesamurthi, S.M. Chen, P. Veerakumar, K. Murugan, A robust Mn@FeNi-S/graphene oxide nanocomposite as a high-efficiency catalyst for the

non-enzymatic electrochemical detection of hydrogen peroxide, Nanoscale 12 (2020) 5961–5972.

[44] J. Balamurugan, T.D. Thanha, G. Karthikeyana, N.H. Kima, J.H. Lee, Sensitivity improvement of an electrical sensor achieved by control of biomolecules based on the negative dielectrophoretic force, Biosens. Bioelectron. 89 (2016) 970–977.

[45] W. Wu, B. Yu, H. Wu, S. Wang, Q. Xia, Y. Ding, Synthesis of tremella-like CoS and its application in sensing of hydrogen peroxide and glucose, Mater. Sci. Eng. C. Mater. Biol. Appl. 70 (2017) 430–437.

[46] F. Xie, X. Cao, F. Qu, A.M. Asiri, S. Sun, Cobalt nitride nanowire array as an efficient electrochemical sensor for glucose and H_2O_2 detection, Sens. Actuator B-Chem. 255 (2018) 1254–1261.

[47] D. Zhou, X. Cao, Z. Wang, S. Hao, X. Hou, F. Qu, G. Du, A.M. Asiri, C. Zheng, X. Sun, Fe_3N-Co_2N nanowires array: a non-noble-metal bifunctional catalyst electrode for high-performance glucose oxidation and H_2O_2 reduction toward non-enzymatic sensing applications, Chem. -Eur. J. 23 (2017) 5214–5218.

[48] J. Tian, Q. Liu, C. Ge, Z. Xing, A.M. Asiri, A.O. Al-Youbi, X. Sun, Ultrathin graphitic carbon nitride nanosheets: a low-cost, green, and highly efficient electrocatalyst toward the reduction of hydrogen peroxide and its glucose biosensing application, Nanoscale 5 (2013) 8921–8924.

[49] D. Liu, T. Chen, W. Zhu, L. Cui, A.M. Asiri, X. Sun, Cobalt phosphide nanowires: an efficient electrocatalyst for enzymeless hydrogen peroxide detection, Nanotechnology 27 (2016), 33LT01.

[50] T. Marimuthu, M.R. Mahmoudian, S. Mohamad, Y. Alias, Synthesis and characterization of non-enzymatic hydrogen peroxide sensor of polypyrrole coated cobalt nanocomposites, Sens. Actuator B-Chem. 202 (2014) 1037–1043.

[51] L. Zheng, D. Ye, L. Xiong, J. Xu, K. Tao, Z. Zou, D. Huang, X. Kang, S. Yang, J. Xia, Reduced graphene oxide nanocomposite and its application on hydrogen peroxide biosensor, Anal. Chim. Acta 768 (2013) 69–75.

[52] T. Lötzbeyer, W. Schuhmann, H.-L. Schmidt, Direct electrocatalytical H_2O_2 reduction with hemin covalently immobilized at a monolayer-modified gold electrode, J. Electroanal. Chem. 35 (1995) 341–344.

[53] W. Dong, Y. Ren, Z. Bai, Y. Yang, Q. Chen, Fabrication of hexahedral Au-Pd/graphene nanocomposites biosensor and its application in cancer cell H_2O_2 detection, Bioelectrochemistry 128 (2019) 274–282.

[54] R. Jimenez-Perez, L. Almangro, M.I. Gonzalez-Sanchez, M.A. Pedreno, E. Valero, Non-Enzymatic screen-printed sensor based on PtNPs@polyazure a for the real-time tracking of the H_2O_2 secreted from living plant cells, Bioelectrochemistry 134 (2020), 107526.

[55] A. Uzunoglu, H.H. Ipekci, The use of CeO_2-modified Pt/C catalyst inks for the construction of high-performance enzyme-free H_2O_2 sensors, J. Electroanal. Chem. 848 (2019), 113302.

[56] P. Zhang, D. Guo, Q.H. Li, Manganese oxide ultrathin nanosheets sensors for non-enzymatic detection of H_2O_2, Mater. Lett. 125 (2014) 202–205.

[57] R. Banavath, R. Srivastava, P. Bhargava, Improved non-enzymatic H_2O_2 sensors using highly electroactive cobalt hexacyanoferrate nanostructures prepared through EDTA chelation route, Mater. Chem. Phys. 267 (2021), 124593.

[58] M.L. Mujica, I. Sotomayor-Santander, P. Hermosilla-Ibánez, F. Oyarzun-Ampuero, M.C. Rodríguez, G.A. Rivas, D. Venegas-Yazigi, S. Bollo, MWCNT-organoimido polyoxomolybdate hybrid material: analytical applications for amperometric sensing of hydrogen peroxide, Electroanalysis 33 (2021) 2105–2114.

[59] J.S. Daniels, N. Pourmand, Label-free impedance biosensors: opportunities and challenges, Electroanalysis 19 (12) (2007) 1239–1257.

[60] P. Balasubramanian, P. Annalakshmi, S.-M. Chen, T. Sathesh, T.-K. Peng, T.S. T. Balamurugan, Facile solvothermal preparation of Mn2CuO4 microspheres: excellent electrocatalyst for real-time detection of H_2O_2 released from live cells, ACS Appl. Mater. Interfaces 10 (50) (2018) 43543–43551.

[61] M. Vitai, Góth. Reference ranges of normal blood catalase activity and levels in familial hypocatalasemia in Hungary, Clin. Chim. Acta 1 (6) (1997) 35–42.

[62] H.J. Forman, A. Bernardo, K.J.A. Davies, What is the concentration of hydrogen peroxide in blood and plasma? Arch. Biochem. Biophys. (2016) 48–53.

[63] R. Gaikwad, P.R. Thangaraj, A.K. Sen, Direct and rapid measurement of hydrogen peroxide in human blood using a microfluidic device, Sci. Rep. 11 (2021) 2960.

[64] P. Li, Y. Jia, N. Zhao, Y. Zhang, P. Zhou, Z. Lou, et al., Quantifying the fast dynamics of HClO in living cells by a fluorescence probe capable of responding to oxidation and reduction events within the time scale of milliseconds, Anal. Chem. 92 (19) (2020) 12987–12995.

[65] H. Tan, X. Wu, Y. Weng, Y. Lu, Z.-Z. Huang, Self-assembled FRET nanoprobe with metal–organic framework as a scaffold for ratiometric detection of hypochlorous acid, Anal. Chem. 92 (4) (2020) 3447–3454.

Tomáš Urbánek (Mgr., PhD student), is a student at Charles University Prague, Czech Republic, has published 3 articles, H-index 2.

Iryna Ivanko (Mgr., PhD student), is a student at Charles University Prague, Czech Republic, has published 8 articles, H-index 3.

Jan Svoboda (Dr., senior researcher), Researcher in XPS spectroscopy, has published 44 articles, H-index 13.

Elena Tomšík* (Dr., senior researcher, Deputy Head of the Department), has published 54 articles, H-index 21.

Martin Hrubý* (Dr., senior researcher, Head of the Department), has published 175 articles, H-index 26.

Supporting Information

Selective Potentiometric Detection of Reactive Oxygen Species (ROS) in Biologically Relevant Concentrations by a Modified Metalized Polyporphyrine Sensing Layer Coated with Nonbiofouling Poly(2-alkyl-2oxazoline)s

Tomáš Urbánek, Iryna Ivanko, Jan Svoboda, Elena Tomšík,* Martin Hrubý*

Institute of Macromolecular Chemistry, Czech Academy of Sciences, Heyrovského náměstí 2, 162 00 Prague 6, Czech Republic
E-mail: E.T. (tomsik@imc.cas.cz), M.H. (mhruby@centrum.cz)

Kinetic study of polymerization of 2-methyl-2-oxazoline initiated by 3-(bromomethyl)thiophene

The polymerization rate was determined with gas chromatography system Autosystem (Perkin Elmer) equipped with column BD-35MS (30 m; 0.25 mm; 0.25 µm; Restek). Quantification of the residual 2-methyl-2-oxazoline was done by the method of internal standard (mesitylene). The polymerization mixture was prepared (M_{th} = 5 kDa, n_M/n_I = 59, m_M = 70.6 mg) under argon flow and divided into 8 microwave vials. Each of the vial, with the same composition, was quenched in different times and the content of residual MeOx was detected and the values are plotted in the **Figure S1**. The theoretical values of molar masses (red) were calculated. The polymerization conditions are described in the main article.
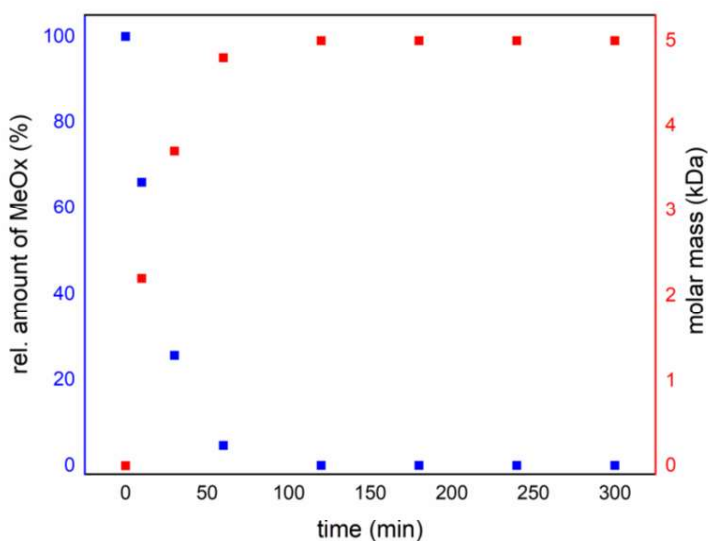
Figure S1. Decrease of MeOx depending on the polymerization time.

Characterization of α-thiophene-ω-hydroxy poly(2-methyl-2-oxazoline)

The synthetized polymers of PMeOx were characterized by ^{1}H NMR spectroscopy. Their typical spectra are shown in the **Figure S2**. There are two main peaks with the shifts at 2.09 and 3.40 ppm. The ratio of the integral areas of these peaks responds to the ratio of protons producing these signals – which is 3:4. There are also minute signals in the range of values of 6.80 and 7.60 ppm which are caused by the end group of thiophene.
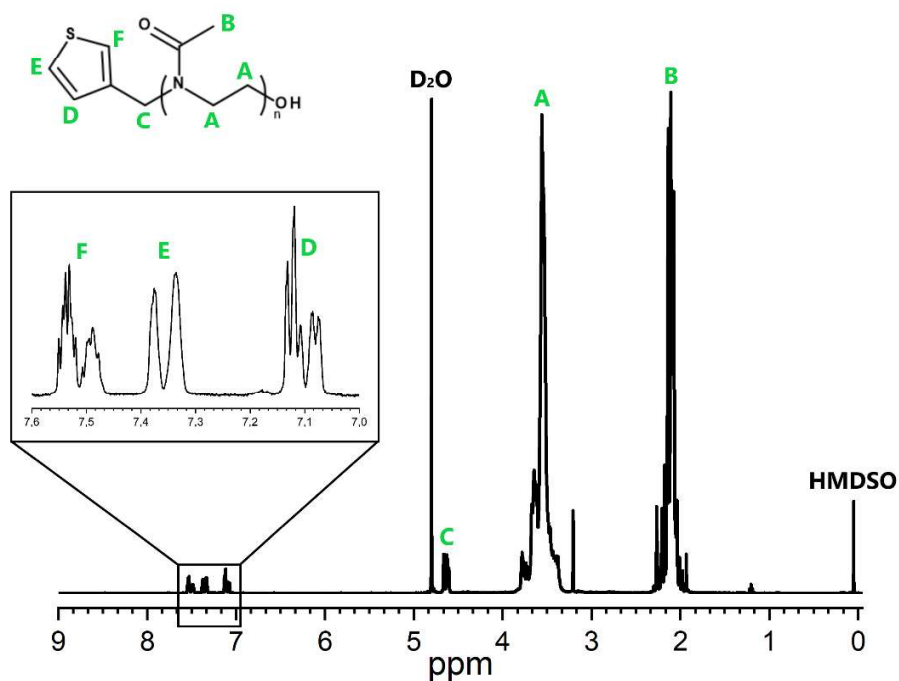
Figure S2. Typical ^{1}H NMR spectrum for synthetized poly(2-methyl-2-oxazoline)s.

The polymers of PMeOx were characterized by size exclusion chromatography and their chromatograms are shown in **Figure S3**.
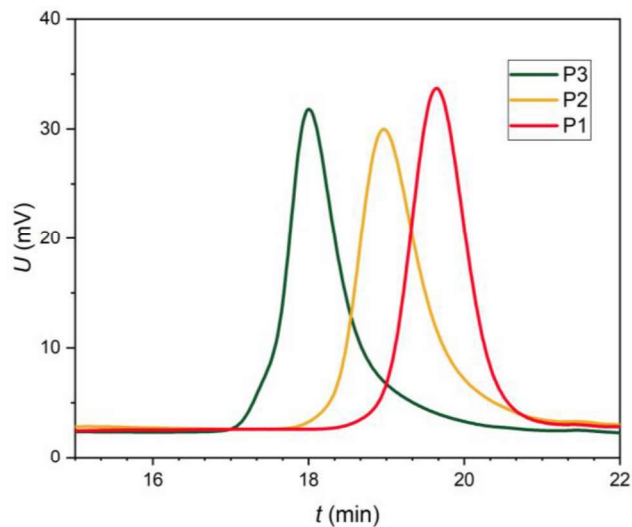
Figure S3. SEC chromatograms of prepared polymers.

Characterization of 5,10,15,20-tetra(thien-2-yl)porphyrin (2TTP) and 5,10,15,20-tetra(thien-3-yl)porphyrin (3TTP)
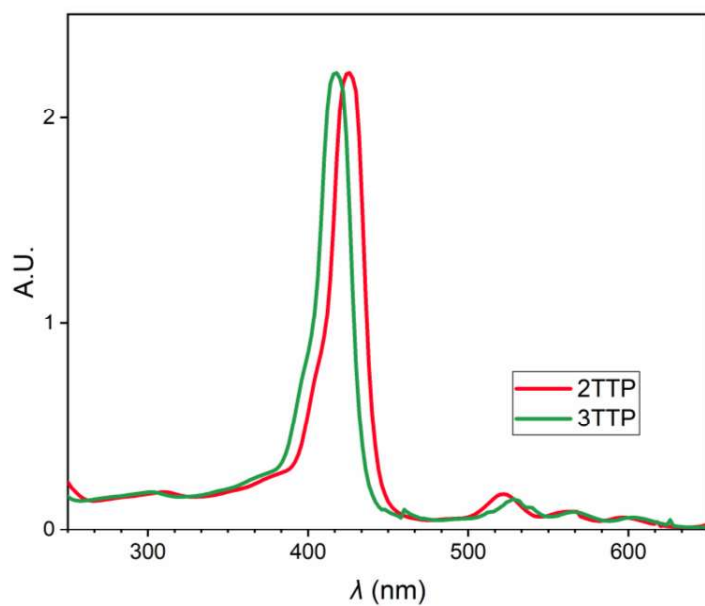
Figure S4. Absorption spectra of 2TTP and 3TTP.
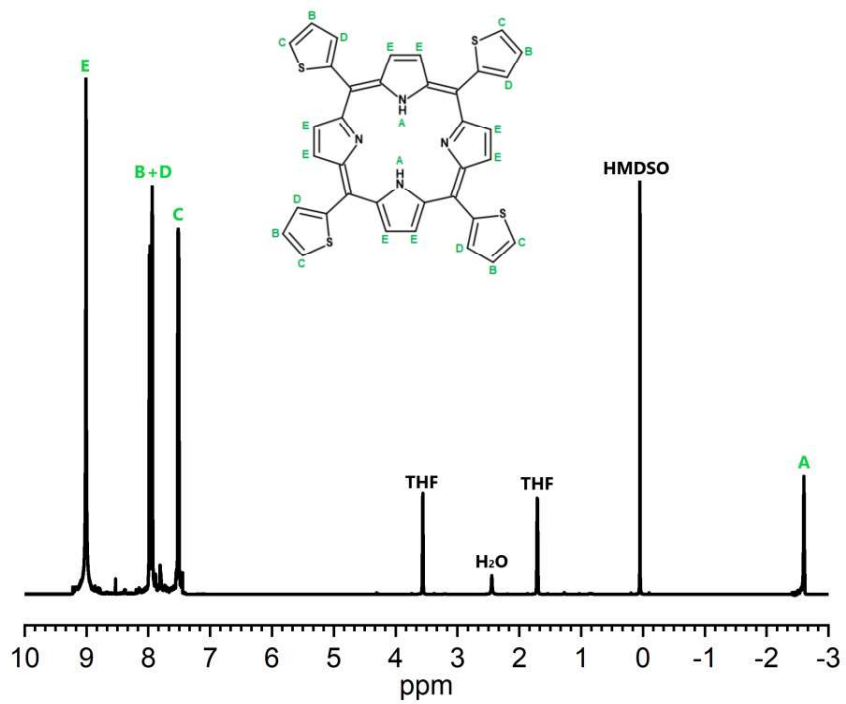
Figure S5. ^{1}H NMR spectrum of 2TTP.
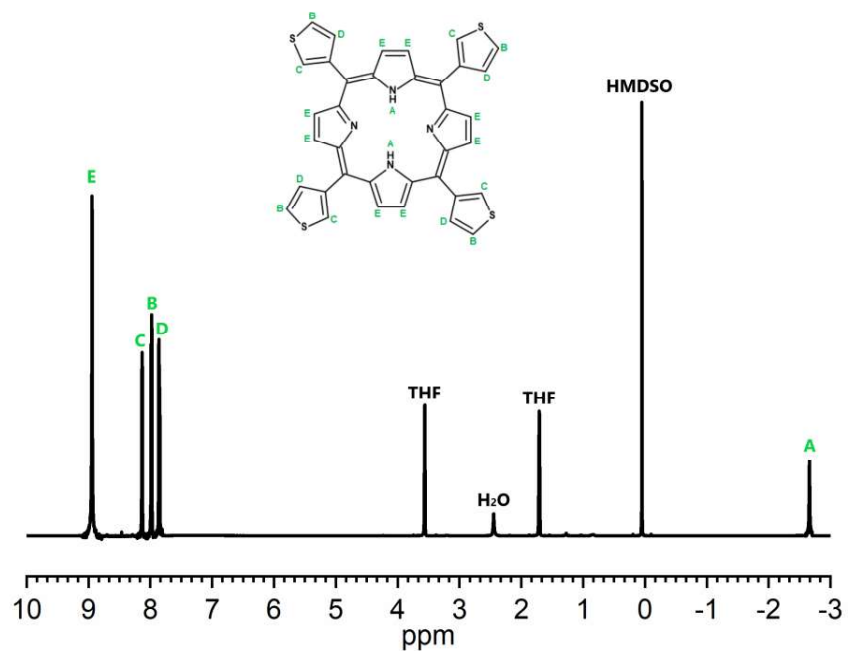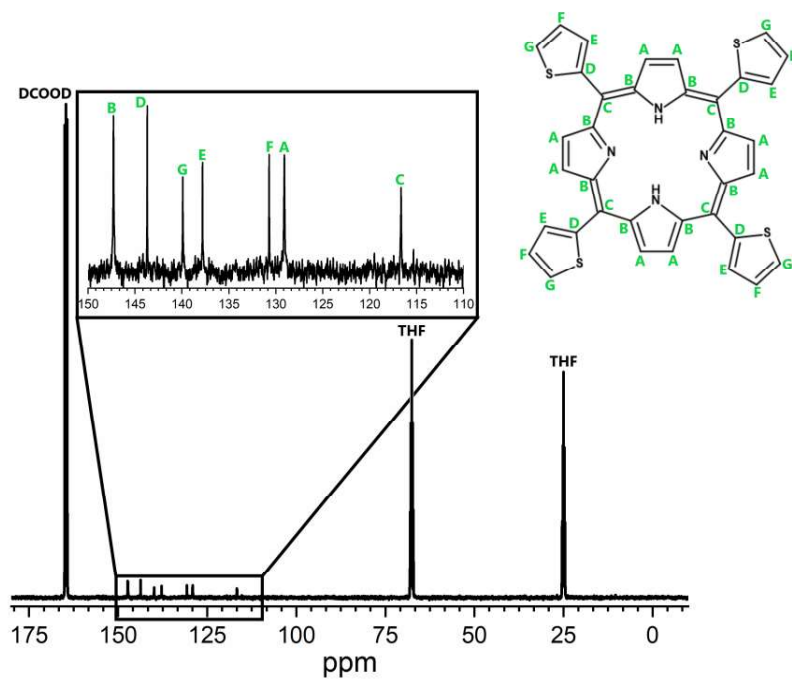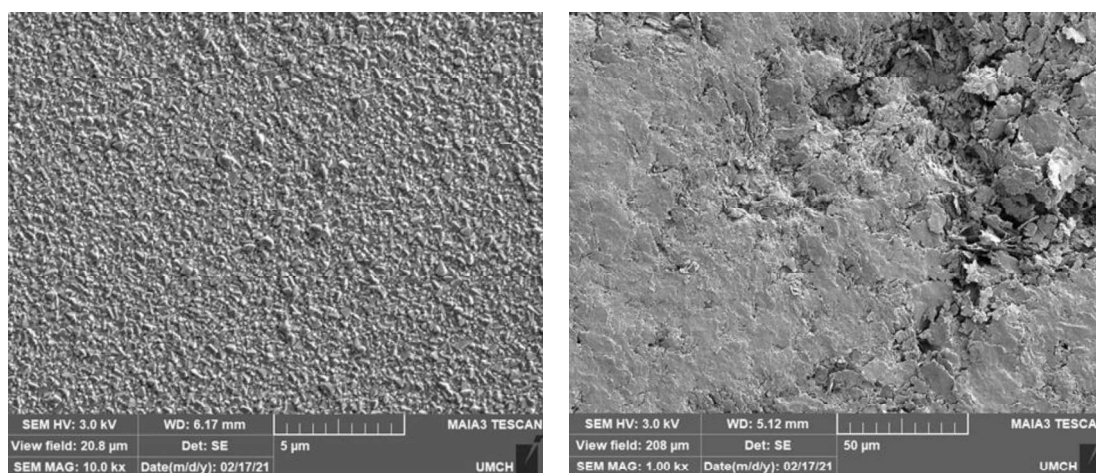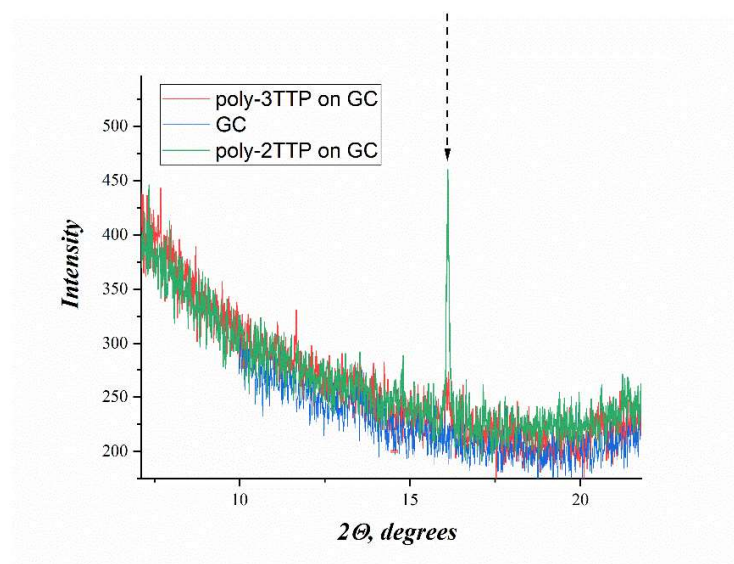
Figure S6. ^{1}H NMR spectrum of 3TTP.
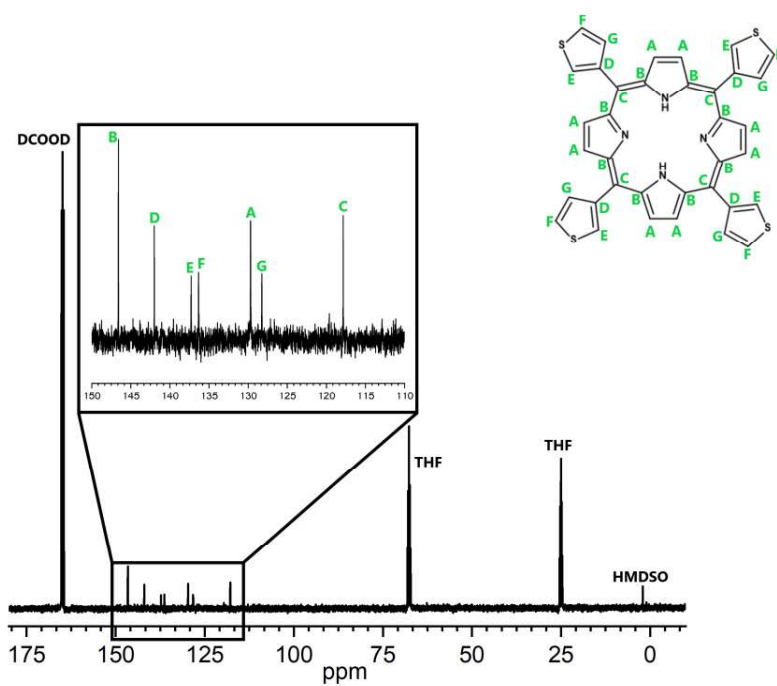
Figure S7. ^{13}C NMR spectrum of 3TTP.

1. Characterization of the substrates

The FTO and GC electrodes were used as electrode substrates for the polymerization of TTP and 2 TTP respectively.

Figure S8. SEM image of the surface of FTO glass(left) and GC (right). Magnification: 10 000 times.


Figure S9. X-ray diffraction of poly(3TTP) and poly(2TTP) on GC support, the spectrum of GC is added for comparison.

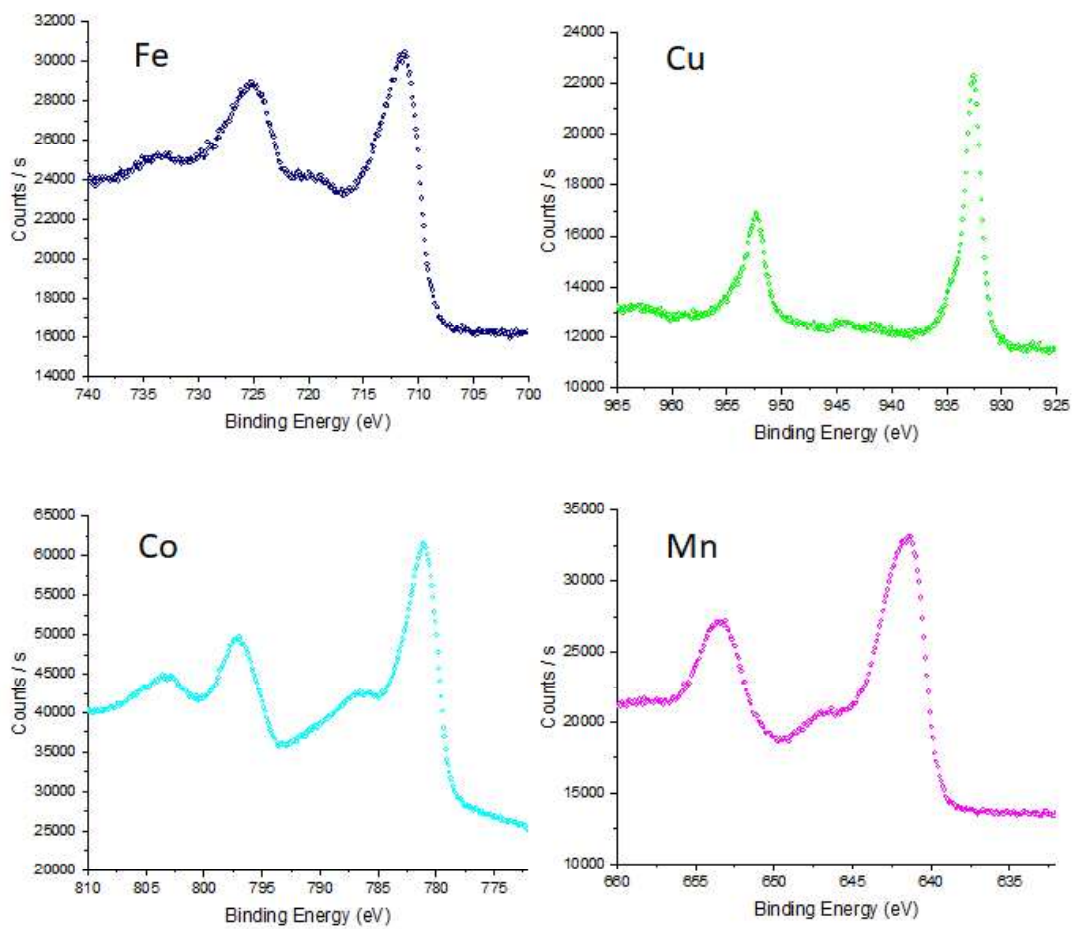**Table S1**: Atomic concentration of metals in poly-3TTP.

Polymer film	Atomic % of corresponding metal	Atomic % of N
poly-3TTP-Fe	1.75 ± 0.09	4.64 ± 0.25
poly-3TTP-Cu	0.07 ± 0.02	2.65 ± 0.63
poly-3TTP-Co	0.23 ± 0.06	1.37 ± 0.32
poly-3TTP-Mn	0.42 ± 0.01	3.56 ± 0.53

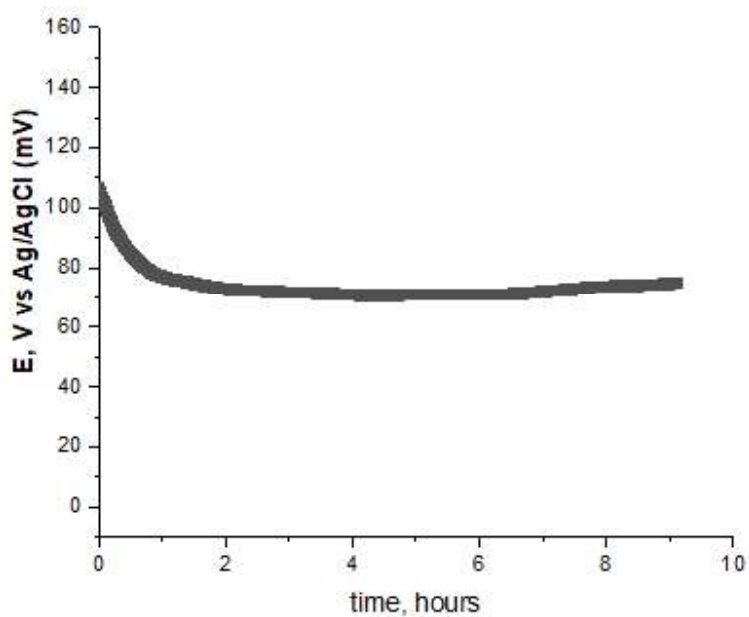The theoretical calculation of the atomic % of N in poly-3TTP is 8.7 %.
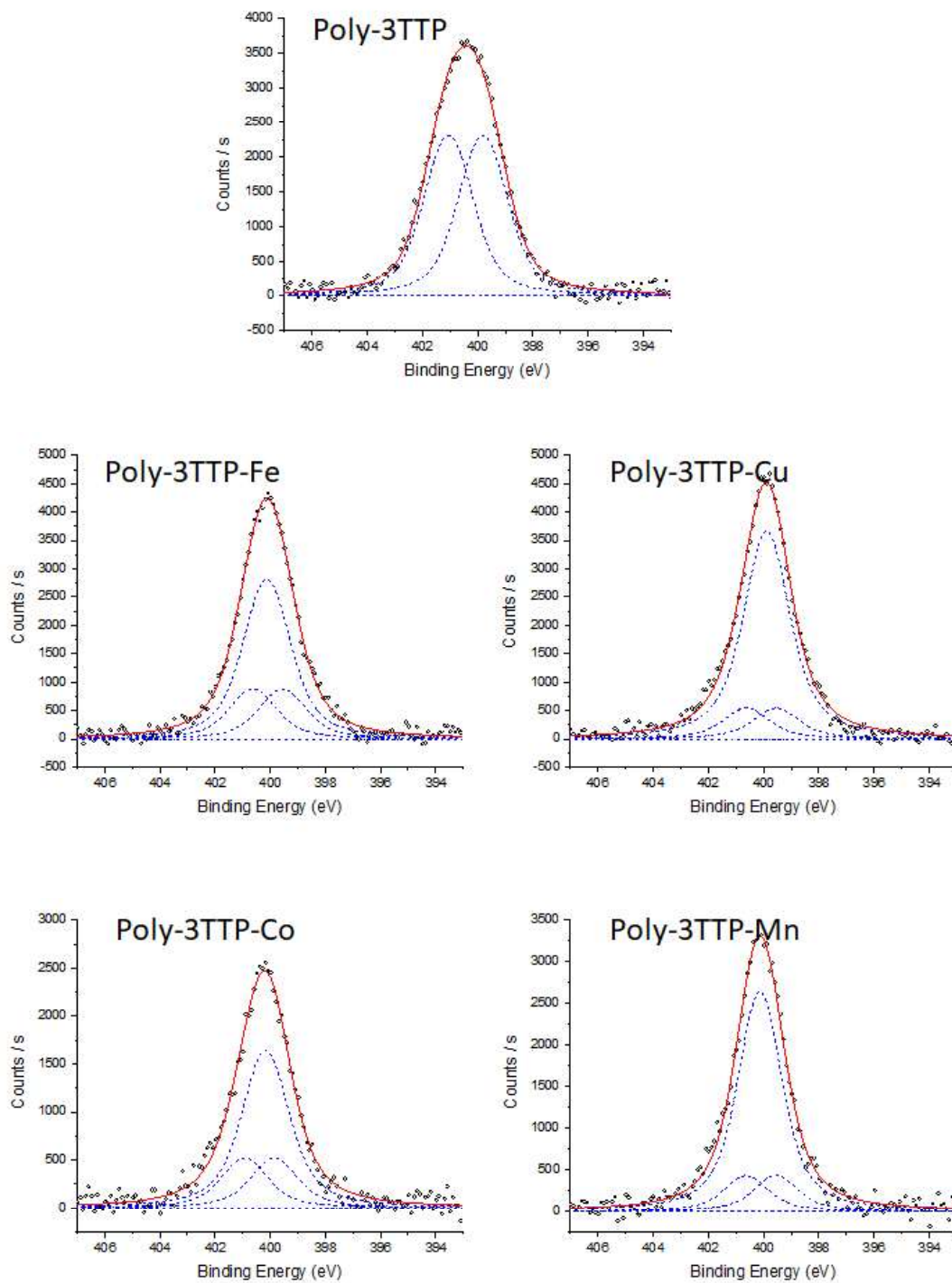
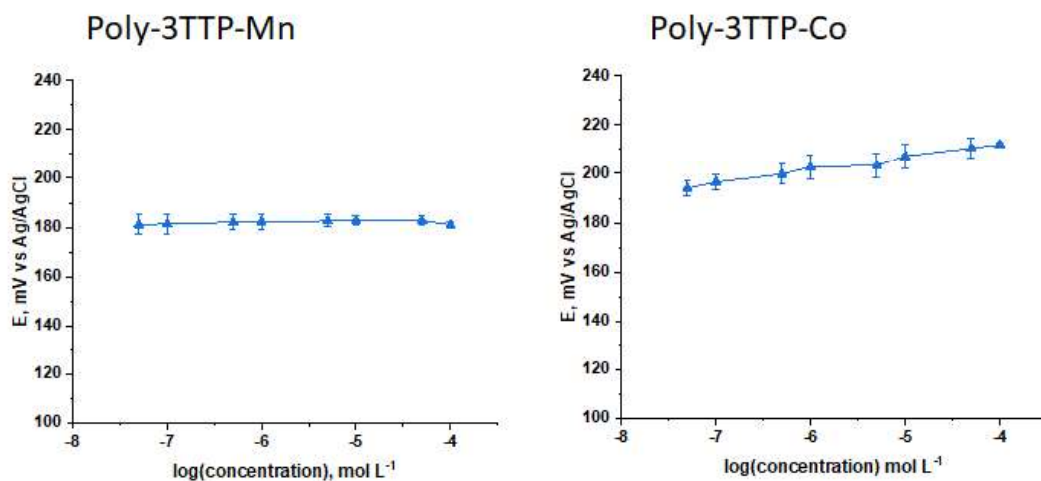**Figure S10**. XPS spectra of poly-3TTP and its composite with metals.

Figure S11. XPS spectra of measured of metals in poly-3TTP.

Figure S12. Open circuit potential of bare poly-3TTP electrode (n = 3) measured in PBS solution with H_2O_2.

Figure S13. Potentiometric detection of H_2O_2 in PBS (pH 7) for poly-3TTP-Mn sensing layer (left) and poly-3TTP-Co sensing layer (right).

Table S2: Atomic concentration of N in different samples.

Sample	Atomic concentration of N, %
PMeOx*	7.1
3TTP*	8.8
Poly-3TTP-Fe	4.64 ± 0.25
Poly-3TTP-Fe/PMeOx (1200)	3.96 ±0.38
Poly-3TTP-Fe/PMeOx (2000)	13.55 ± 0.69
Poly-3TTP-Fe/PMeOx (4700)	**14.06 ± 0.27**

* Theoretical value.